FIRST DETERMINATION OF THE ^{8}Li VALENCE NEUTRON ASYMPTOTIC NORMALIZATION COEFFICIENT USING THE ^{7}Li(^{8}Li,^{7}Li)^{8}Li REACTION

by

Derek Howell

B.Sc., Simon Fraser University, 2005

A Thesis submitted in partial fulfillment
of the requirements for the degree of

Doctor of Philosophy

in the
Department of Physics
Faculty of Science

SIMON FRASER UNIVERSITY
Spring 2013

APPROVAL

Name: Derek Howell

Degree: Doctor of Philosophy

Title of Thesis: First Determination of the ^{8}Li Valence Neutron Asymptotic Normalization Coefficient using the ^{7}Li(^{8}Li,^{7}Li)^{8}Li reaction

Examining Committee:

Dr. Sarah Johnson,
Senior Lecturer
Chair

Dr. Dugan O'Neil (Senior Supervisor),
Associate Professor

Dr. Barry Davids (Co-Supervisor),
Adjunct Professor

Dr. Levon Pogosian (Supervisor),
Associate Professor

Dr. Eldon Emberly (Internal Examiner),
Associate Professor

Dr. Alan Chen (External Examiner),
Associate Professor, Physics and Astronomy
McMaster University

Date Approved: March 19^{th}, 2013

Partial Copyright Licence

Abstract

Solar neutrino experiments have often been plagued with large uncertainties. With the recent results from the Borexino Collaboration, for the first time the total uncertainty in the ^{7}Be solar neutrino flux measurement is smaller than the uncertainty of standard solar model (SSM) predictions.

Improvement in neutrino experiments must be followed by refinements to the SSM; to do so requires reduced uncertainties on the parameters used in SSM calculations. One such value is the astrophysical S-factor describing the ^{7}Be(p,γ)^{8}B reaction, $S_{17}(0)$.

We report here a determination of the asymptotic normalization coefficient (ANC) of the valence neutron in ^{8}Li from a measurement of the angular distribution of the single neutron transfer between ^{8}Li and ^{7}Li via the ^{7}Li(^{8}Li,^{7}Li)^{8}Li reaction at 11 MeV. Using isospin symmetry the ^{8}B ANC has also been calculated and used to infer a value for $S_{17}(0)$ of 20.2 ± 4.4 eV b.

To my wife Lisa. Without her love and support, none of this would have been possible.

"Wonder implies the desire to learn"

— Aristotle

Acknowledgments

To begin I would like to thank Barry Davids for his guidance and advice that helped me along with every step. Thanks must also go to Ritu Kanungo and Pat Walden for their extensive help with the experiment. Thanks to Tom Davinson for sharing his expertise of the TUDA systems and help in solving system and detector mysteries I would never have been able to figure out on my own. Thanks to Ian Thompson for his help in understanding FRESCO and all the calculations that at first seemed overwhelming. Finally, thanks to countless others who helped. Your help, support and advice, however small, was invaluable.

Contents

List of Tables

List of Figures

Chapter 1

Introduction

Nuclear astrophysics focuses on the study of the thermonuclear reactions taking place in stars and the associated nucleosynthesis of the elements. From the development of standard solar models (SSMs) to measurements and theoretical estimations of nuclear reaction rates in a stellar environment, nuclear astrophysics aims to understand the origin of the elements and the energy generation in stars.

1.1 Nuclear Astrophysics

Shortly following the Big Bang the early universe consisted of little more than hydrogen and helium and trace amounts of heavier elements. Through the nuclear fusion that took place in the first stars and subsequent generations of stars the elemental composition that exists today was established. It is through the synthesis of heavier elements via nuclear fusion that stars generate the massive amounts of energy that allows them to shine for up to billions of years.

Direct study of most of the nuclear reactions taking place in a star is not possible for many reasons. Without being able to directly study the nuclear reactions as they take place in a star, recreating the reaction in a laboratory is the next best thing. One of the problems with directly observing a reaction as it occurs in a star as well as recreating the same reactions in a laboratory is that many of the nuclear reactions taking place in a stellar environment have vanishingly small cross sections at relevant energies. For example, the first reaction of the pp chains, the fusion of two protons to form deuterium expressed by

the reaction p + p $\rightarrow$ d + $e^+ + \nu$, has a theoretically calculated astrophysical S-factor[1] of $(4.01 \pm 0.04) \times 10^{-22}$ keVb [1], which results in a reaction rate per particle pair in a star such as the Sun of

$$\langle \sigma v \rangle_{pp} = 1 \times 10^{-43}\,\mathrm{cm^3 s^{-1}}, \tag{1.1}$$

It is only through the sheer number of protons present in the Sun that this reaction occurs with any regularity.

Experiments must then be designed to study these reactions at higher energies where the cross section is larger, then extrapolate the results down to astrophysically relevant energies. Alternatively, experiments can be designed to make indirect measurements of a stellar reaction. By studying a similar reaction and relating the results via theory to the desired reaction, the hindrance of a small cross section, or extrapolation error can be removed or lessened.

This thesis is a study of an indirect measurement of a stellar reaction. The ^{7}Be(p,γ)^{8}B reaction is a prominent neutrino producing reaction in the Sun that has been the object of much experimental and theoretical work. A recent high precision measurement indicating a larger value than previous lower precision measurements [2] has renewed interest in this reaction. This study aims to determine the asymptotic normalization coefficient (ANC)[2] of the valence neutron in ^{8}Li via the elastic transfer reaction ^{7}Li(^{8}Li,^{7}Li)^{8}Li. By taking advantage of charge symmetry in the mirror system with ^{7}Be and ^{8}B a new value for the astrophysical S-factor for the ^{7}Be(p,γ)^{8}B reaction, $S_{17}(0)$, will be inferred from the ^{8}Li valence neutron ANC.

1.2 Thermonuclear Reactions in a Stellar Environment

Regardless of the size or temperature of a star, the nuclear energy generated in a stellar environment originates from the fusion of lighter elements into heavier elements. The synthesis of heavier elements releases energy in accordance with Einstein's famous mass-energy relation in relativity,

$$E_0 = mc^2. \tag{1.2}$$

[1] See section 2.1.3 for more information on astrophysical S-factors

[2] See section 2.3.2 for more information on ANCs

As lighter elements combine and form heavier elements whose mass is less than the combined mass of their constituents, energy is released in the form of kinetic energy via Einstein's equation. This energy is better expressed in terms of the mass difference between initial and final states.

$$E = \Delta mc^2 = (m_f - m_i)c^2. \tag{1.3}$$

This process is exothermic up to approximately A=60, where the binding energy per nucleon reaches a maximum as seen in Figure 1.1. Nearly all elements below this peak are produced as the result of thermonuclear fusion reactions that take place in stars. The observed abundances in the Universe of elements above the binding energy peak at A $\sim$ 60 are thought to arise principally from two different neutron capture processes, the slow (s) and rapid (r) neutron capture processes.

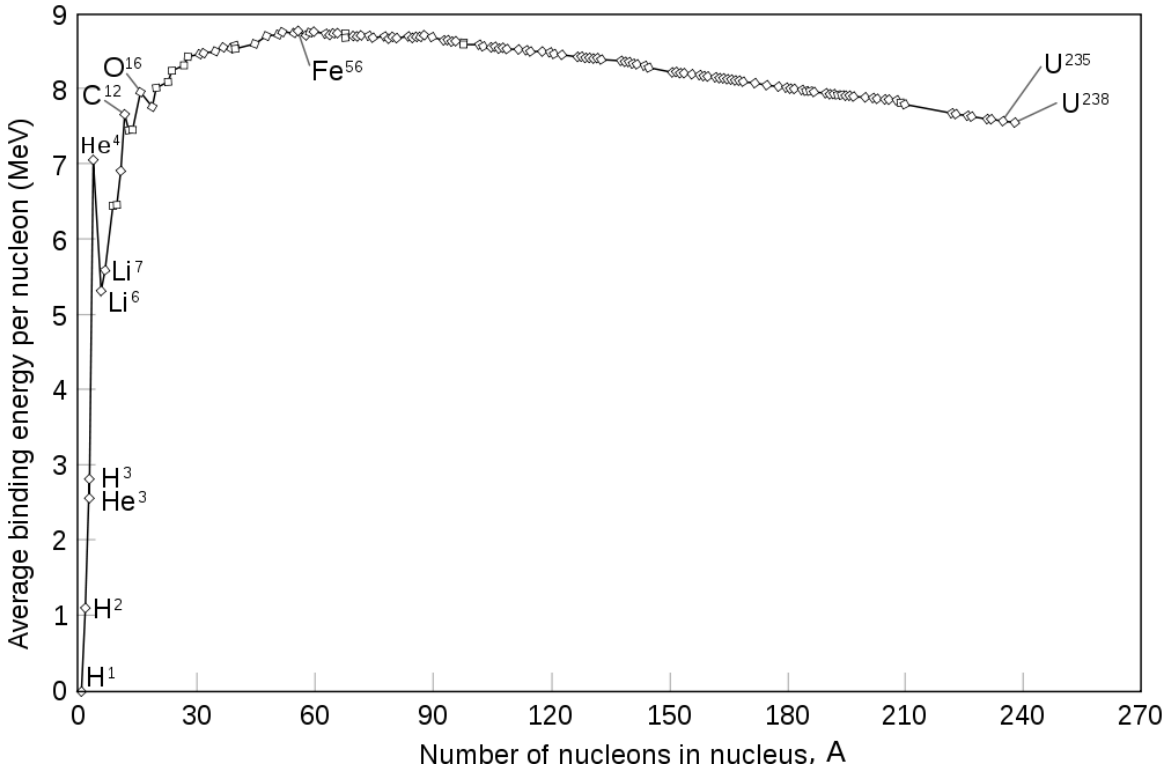

Figure 1.1: Binding Energy per Nucleon curve. Figure from Reference [3]

For the majority of the lifecycle of a star the fusion of hydrogen into helium is the main source of thermonuclear energy. Two distinct processes, the pp chains and the CNO cycles, facilitate hydrogen burning[3] in a star and will be discussed later in this section. While both processes work towards the same end, the steps taken and optimal stellar conditions for each process differ greatly. The net result from either the pp chains or the CNO cycles is the reaction

$$4\mathrm{p} \rightarrow {}^{4}\mathrm{He} + 2\mathrm{e}^{+} + 2\nu, \tag{1.4}$$

which releases a total 26.73 MeV calculated from Equation 1.3.

Figure 1.2 shows the power obtained from hydrogen burning via the pp chains and the CNO cycles as a function of stellar temperature. In lower temperature stars such as our Sun the pp chains are the dominant process. As the temperature increases, as it generally does in larger stars, the CNO cycles become the dominant process.

The total energy released by the net reaction of Equation 1.4 is 26.73 MeV, but the actual amount of energy that is absorbed by the star is slightly less than this due to energy lost from escaping neutrinos. The high densities of stellar material stops all but these neutrinos from escaping. The neutrinos thus provide the only direct means of observing the reactions taking place in the core of the Sun.

1.2.1 The Proton-Proton Chains

Following Big Bang Nucleosynthesis (BBN), the isotopic abundances in the early Universe were approximately 75% hydrogen, 25% helium, 2.5×10^{-7}% deuterium, 4.2×10^{-7}% ^{3}He and trace amounts of lithium [4] by mass. The first generation of stars consist of the elements produced in BBN, and therefore contain nothing much heavier than helium. With only the presence of hydrogen and helium, first generation stars are only able to produce energy via the pp chains regardless of the temperature. The lack of carbon, nitrogen, and oxygen needed in the CNO cycles prevents it from taking over as the dominant means of energy production as indicated in Figure 1.2. The pp chains are also the main method of energy production in stars whose mass is less than 1.5 times the mass of the Sun, due to the fact that the temperature of a star is directly related to its mass. As shown in Figure 1.2 the pp

[3]The term burning is often used to refer to all stellar thermonuclear fusion reactions that consume a specific element, i.e. hydrogen burning refers to all processes that contribute to consume hydrogen in a star.

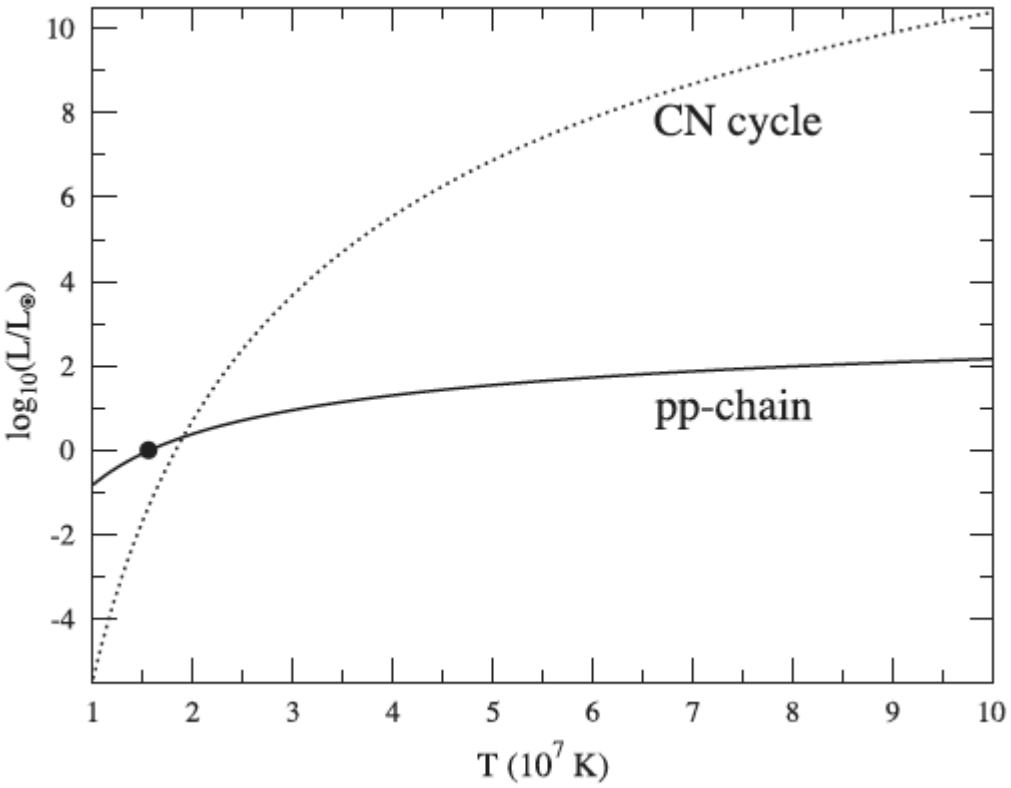

Figure 1.2: Power liberated by the pp chains and one of the CNO cycles as a function of temperature. The crossover point between the pp chains and the CNO cycles is roughly at a mass of 1.5 times that of the Sun. The black dot indicates the temperature of the Sun. Figure taken from Reference [1].

chains are dominant in low temperature stars.

There are three main branches of the pp chains, each contributing to the total energy production of the star. The contribution from each branch of the pp chains depend on the density, temperature, and chemical composition of the star [4]. Figure 1.3 outlines the different branches of the pp chains with branching ratios for the Sun given. The first step for all branches of the pp chains begins with two protons coming together to form a deuteron. This can either occur with one proton emitting a positron and becoming a neutron, or by the alternative three body pep reaction. Once a deuteron is formed it quickly combines with another proton to form ^{3}He. At this point the first chain (ppI) completes as two ^{3}He come together forming a ^{4}He nucleus and emitting two protons.

The initial reaction for the second and third branches occurs by fusing a ^{3}He with a ^{4}He (α particle), synthesizing a ^{7}Be nucleus. An alternative to feeding the ppII and ppIII branches is the hep reaction. In this reaction a ^{3}He reacts with a proton to form ^{4}He. This reaction is not part of the main three branches but is mentioned here as it is a high energy neutrino producing reaction that will be discussed later. Also of note, this reaction is theorized to contribute only a small fraction to the energy release of the pp chains due to the slow weak interaction and has never been observed.

From ^{7}Be an electron capture followed by a proton capture will occur to finish the ppII chain producing a ^{4}He nucleus and releasing the previously consumed α particle. Alternatively, a proton is captured producing ^{8}B, followed by the emission of a positron to form an excited state of ^{8}Be, which then α-decays emitting the formed ^{4}He nucleus. For the ppII and ppIII branches I have purposely distinguished the α particle which acts as a catalyst from the ^{4}He nucleus produced by labelling them differently, even though they are the same particle.

As previously stated the fusion of $4p \rightarrow {}^4He + 2\nu_e + 2e^+$ releases 26.73 MeV with only a fraction of that energy absorbed by the star. The energy lost in each branch by escaping neutrinos produced in the various reactions is outlined in Table 1.1. Subtracting the escaping neutrino energy from the total energy produced from the synthesis of ^{4}He yields the total energy gained by a star from each branch of the pp chains. As has been alluded to, more massive stars that contain an initial amount of carbon, nitrogen, and oxygen will produce the majority of their energy via the CNO cycles rather than the pp chains.

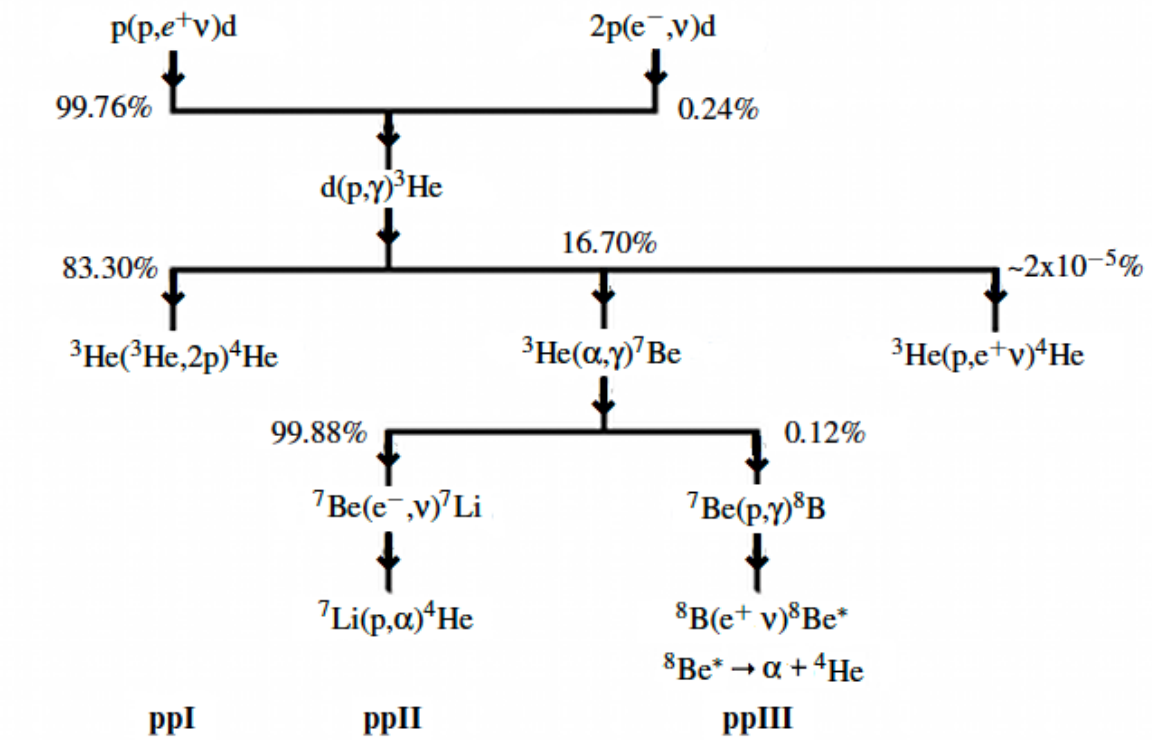

Figure 1.3: The pp chains with associated branching ratios applicable to the Sun[1]. While an α particle and ^{4}He are the same the use of α in some reactions is to highlight that this particle is acting as a catalyst and is not the ^{4}He produced in the chain.

ID	Reaction	Neutrino Energy (MeV)
1	p(p,$e^+\nu$)d	0.0 to 0.4
2	2p(e$^-$,ν)d	1.4
3	^{3}He(p,e$^+\nu$)^{4}He	0.5 to 18
4	^{7}Be(e$^-$,ν)^{7}Li	0.38, 0.86
5	^{8}B(e$^+\nu$)^{8}Be*	0 to 18

Table 1.1: Energy of emitted neutrinos from reactions in the pp chains. Reaction 3, known as the hep reaction, has never been detected due to the extremely small branching ratio and is only theorized at this time.

1.2.2 CNO cycles

The CNO cycles are more prominent than the pp chains in second or later generation stars whose mass is greater than 1.5 times the mass of the Sun. The ppI branch of the pp chains directly fuses protons together to form helium nuclei. The CNO cycles use heavier elements present in the star as catalysts to open up faster reactions, just as α particles are used in the ppII and ppIII chains. There must be an initial amount of one of the CNO elements present in the star for the CNO cycles to start. Once the process begins the total number of CNO nuclei doesn't change, but the ratio of each individual species does. Eventually an equilibrium is reached where ^{14}N is the most abundant catalyst [1].

The first cycle utilizes carbon and nitrogen isotopes to facilitate the hydrogen burning of Equation 1.4 and is known as the CNO-I or CN cycle. The sequence of reactions is shown on the left side of Figure 1.4. On the right side of the figure, the second cycle makes use of more oxygen isotopes as catalysts in the hydrogen burning process and is referred to as the CNO-II cycle. The CNO-I cycle produces approximately 1% of the Sun's energy [1]. In more massive stars than the Sun more channels are opened up allowing for additional branches in the CNO cycles.

Energy lost due to escaping neutrinos produced in the CNO cycles occurs similarly as in the pp chains. For more information on the pp chains or the CNO cycles and their associated reactions, the reader is referred to References [1] and [4].

1.3 Neutrinos

In 1930 Wolfgang Pauli introduced the idea of an undetected particle carrying away the observed difference of the energy, momentum, and angular momentum between the initial and final states in beta decay. The neutrino was first detected in 1953 in the Cowan-Reines neutrino experiment where antineutrinos reacted with protons producing neutrons and positrons [5]. Up until then, all study had been focused on the electron neutrino, but in 1962 it was shown by Lederman, Schwartz, and Steinberger that the muon also had its own neutrino [6]. Thus, when the tau lepton was discovered in 1975 it was postulated to also have a neutrino associated with it [7].

In the late 1960s when R. Davis ran an experiment to measure the number of neutrinos coming from the sun using 0.6 kilotons of the dry-cleaning fluid tetrachloroethylene, C_2Cl_4,

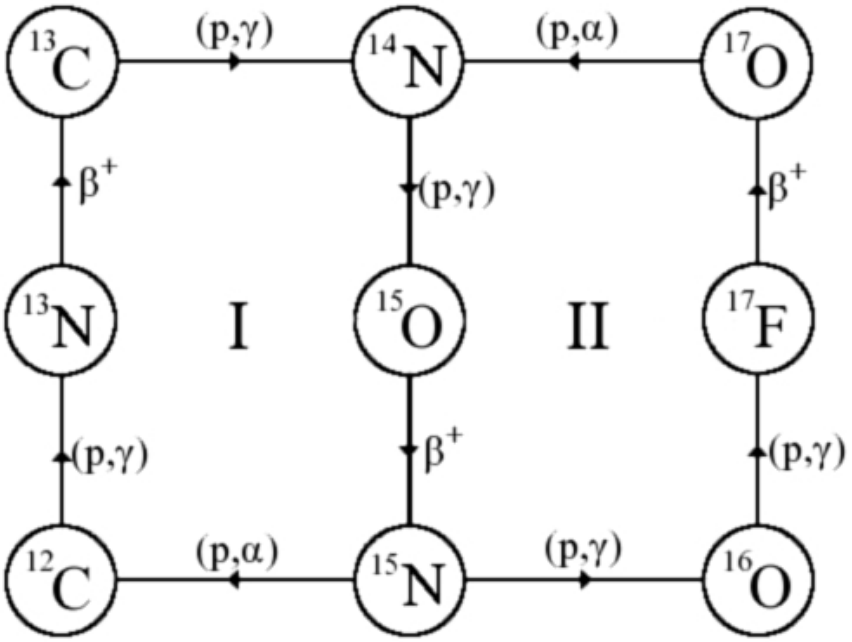

Figure 1.4: The C, N, and O isotopes serve as catalysts for the reaction shown in Equation 1.4. The CN cycle on the left and CNO cycle on the right are together referred to as the CNO bicycle.

via the capture reaction

$$\nu_e + {}^{37}\mathrm{Cl} \rightarrow \mathrm{e}^- + {}^{37}\mathrm{Al} \tag{1.5}$$

a discrepancy was first discovered between the observed capture rate of 2.55 ± 0.25 SNU and the theoretical capture rate of 9.3 ± 1.3 SNU [8]. This discrepancy and ensuing controversy came to be known as the solar neutrino problem.

1.3.1 Solar Neutrinos

Due to the high density in a stellar core, photons from fusion reactions taking place there have a mean free path of less than 10^{-10} the radius of the star [9]; this results in none of the photons created by nuclear fusion exiting the stellar core. One method to directly infer the reactions taking place in the core of a star is by observing the neutrinos that are able to exit the star due to their small probability of interaction with matter. For a star whose size is similar to the Sun the mean free path of a neutrino leaving the core is on the order of 10^7 that of the radius [10]. This results in essentially all produced neutrinos exiting the Sun's core and radiating outward. These exiting neutrinos are the only direct means of detecting the fusion reactions taking place in the core of a star as any photons produced are quickly absorbed. As shown in Figures 1.3 and 1.4 and Table 1.1, certain reactions of the pp chains and the CNO cycles emit neutrinos at a specific energy or in a specific range of energies, thereby allowing them to be detected and possibly identifying the originating reaction.

Following R. Davis in the late 1960s many experiments have been performed to detect solar neutrinos through various different channels. The reaction used in the experiment performed by Davis has a threshold neutrino energy of 0.8 MeV, making it sensitive to neutrinos from reactions 2, 3, 4, and 5 from Table 1.1 and as shown by the bar labeled "Chlorine" at the top of Figure 1.5. In 1986 the Kamiokande group in Japan made the first measurement of solar neutrinos including directional information to screen out background neutrinos [11]. Using 0.68 kilotons of ultra pure water, Ĉerenkov radiation was detected from the recoiling electrons resulting from neutrino electron scattering via the reaction,

$$\nu_e + \mathrm{e}^- \rightarrow \nu_e + \mathrm{e}^-. \tag{1.6}$$

With a threshold neutrino energy of 7.5 MeV this reaction allows only neutrinos from reaction 3 and reaction 5 of Table 1.1 to be detected. The ability to determine the direction of the incident neutrinos from the electron recoils enabled the experimenters to distinguish

neutrinos coming from the Sun from other neutrinos. The same as with Davis' results the results of the experiment once again gave a discrepancy between the number of observed neutrinos and the theoretically calculated value.

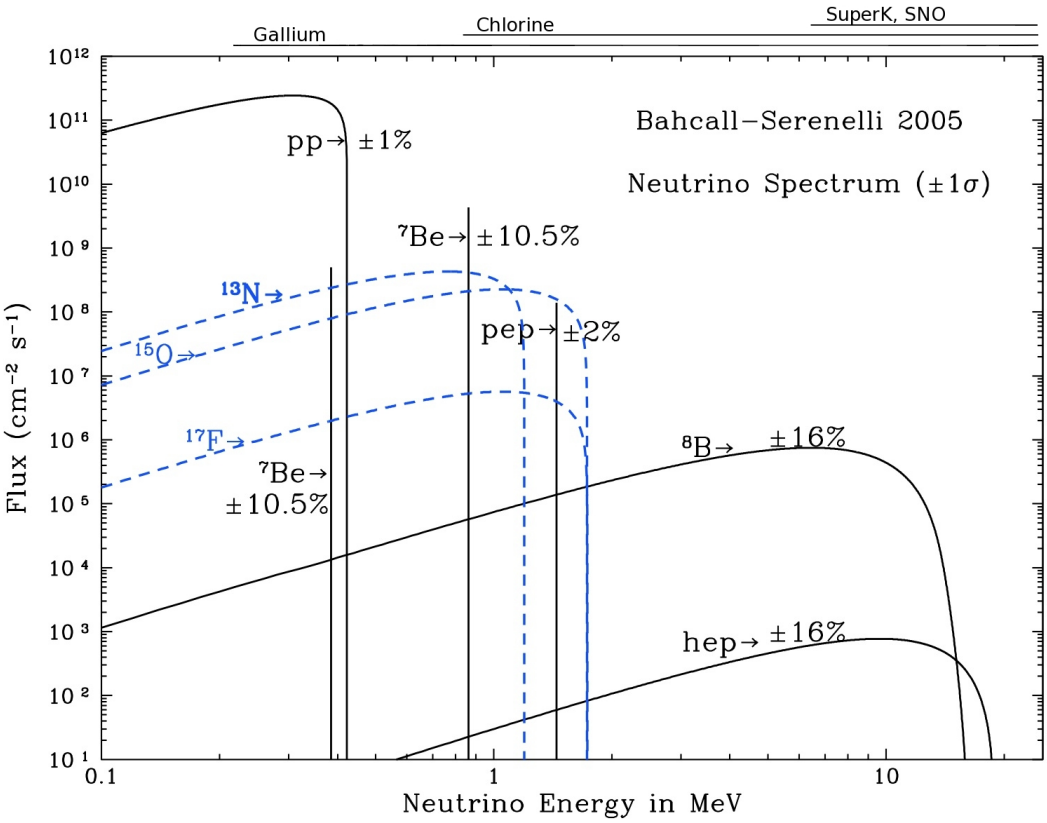

Figure 1.5: The Solar neutrino energy spectrum for all neutrinos produced in the CNO cycles and the pp chains with energies listed in Table 1.1 as predicted by the SSM. Figure from Reference [12].

In 1991 and 1992, two separate studies: SAGE in Russia [13] and GALLEX in Italy [14], again confirmed the neutrino deficit. This time the reaction used was

$$\nu_e + {}^{71}\mathrm{Ga} \rightarrow \mathrm{e}^- + {}^{71}\mathrm{Ge}, \tag{1.7}$$

which has a threshold energy of 0.23 MeV making it sensitive to all the neutrinos listed

in Table 1.1. Beginning in 1996, an expanded version of Kamiokande, Super-Kamiokande, started searching for neutrino interactions. In 1998, after analyzing more than 500 days of data, Super-K reported finding oscillations in atmospheric neutrinos, and thus, evidence for neutrino mass [15].

The theory for neutrino flavour mixing and flavour oscillations dates back to 1957 when Bruno Pontecorvo proposed neutrino-antineutrino oscillations analogous to kaon oscillations [16]. However, it wasn't until 1998 when Super-K made its announcement that there was the first experimental evidence for neutrino oscillations. Shortly following the announcement by Super-K in 2001, the Sudbury Neutrino Observatory (SNO) in Canada confirmed neutrino oscillations in neutrinos arriving from the Sun [17]. SNO was able to detect all three flavours of neutrinos via elastic scattering (ES) on electrons, as well as only electron neutrinos via a charged current (CC) reaction on deuterium. By comparing the CC solar flux of neutrinos above a threshold energy of 6.75 MeV, to the Super-Kamiokande Collaboration's ES flux rate a 3.3σ difference was observed [18] confirming neutrino oscillations.

Much study and effort has gone into knowing the precise fluxes of neutrinos coming from the Sun as these are important when making comparisons between observations and SSMs. The most recent measurement performed by the Borexino Collaboration has reported a ^{7}Be solar neutrino flux of $(3.10 \pm 0.15) \times 10^9$ cm^{-2} s^{-1} [19]. This is the first time the total uncertainty in the neutrino measurement has been smaller than the uncertainty in the SSM prediction of the ^{7}Be solar neutrino flux. In the same study a global solar neutrino analysis resulting in a total flux for pp chain neutrinos of $\Phi_{pp} = 6.06^{+0.02}_{-0.06} \times 10^{10}$ cm^{-2} s^{-1} and for CNO neutrinos of $\Phi_{CNO} < 1.3 \times 10^9$ cm^{-2} s^{-1} at the 95% confidence level was presented.

1.4 $S_{17}(0)$ History and Background

With all that is known about the Sun and the reactions taking place in its core, there is still uncertainty that surrounds it. Apart from the subdominant hep reaction, reaction 5 of Table 1.1, the neutrino producing reaction of the ppIII branch of the pp chains is the only source for solar neutrino signals in water Cerenkov solar neutrino experiments: Super-K in Japan and SNO in Canada. Therefore, predicted rates for these experiments are proportional to the rate of the ^{7}Be(p,γ)^{8}B radiative capture reaction, which at astrophysically relevant energies is the most poorly known of all observed reactions in the pp chains. This single reaction rate uncertainty introduces a large error into the SSMs that go into calculations

for theoretical rates for Super-K and SNO.

The zero energy astrophysical S-factor[4], $S_{17}(0)$, describing the ^{7}Be(p,γ)^{8}B reaction of the ppIII branch of the pp chains has been derived from measurements of ^{7}Be + ^{8}B transfer reactions. Both direct measurements from radiative capture experiments and indirect measurements from Coulomb breakup and transfer reactions provide methods of determining the value of $S_{17}(0)$.

Direct radiative capture measurements have been performed at relative kinetic energies as low as 117 keV [20] to obtain values for $S_{17}(0)$, but have been troubled with large uncertainties both experimentally and theoretically when extrapolating down to relevant solar energies. Indirect experiments provide other methods of extracting the S-factor that do not require extrapolating down to astrophysically relevant energies, by instead studying theoretically related reactions from which the zero energy S factor can be extracted. Recent published values for $S_{17}(0)$ have a range of $S_{17}(0) \approx 17 - 22$ eV b [1].

The purpose of this study is to measure the ^{8}Li valence neutron ANC and thereby make an indirect measurement of $S_{17}(0)$ using the peripheral transfer reaction ^{7}Li(^{8}Li,^{7}Li)^{8}Li.

[4]For a detailed description of astrophysical S-factors see section 2.1.3.

Chapter 2

Theory

Stellar reaction rate theory and scattering theory are both very well developed theories that include many details and subtleties. In this chapter, a brief outline of the theory and calculation that go into determining stellar reaction rates is given. An introduction to basic scattering theory covering more detailed areas that have a relevance to the work of this thesis will also be covered.

2.1 Stellar Reaction Rates

To determine which nuclear reactions are taking place in a star and with what frequency, stellar nucleosynthesis models require values for reaction rates of all possible reactions. The values for the reaction rates are strongly dependent on the temperature of the star; at higher temperatures the rates are much greater than at lower temperatures. This is due to the fact that thermonuclear reactions that take place in a stellar environment occur at sub-Coulomb barrier energies and thus, must proceed by quantum tunnelling through the Coulomb barrier. In addition to tunnelling through the Coulomb barrier any resonance at the energies of colliding pairs of nuclei increases the stellar reaction rates.

The resonant cross section for a pair of nuclei, i, that collide and form a compound nucleus in a single excited state which subsequently disintegrates into a pair of nuclei, f, may be expressed in the simple form [21]

$$\sigma = \frac{\pi}{k_i^2} \frac{\Gamma_i \Gamma_f}{(E_\lambda - E)^2 + (\Gamma/2)^2} \tag{2.1}$$

where k_i is the wave number of the colliding pair in the center of mass system, and E is their energy. E_λ represents the resonance energy of the compound system. The parameter Γ is the total width of the compound nuclear state given by the sum of the individual parameters Γ_i and Γ_f known as the partial widths, which are of the form

$$\Gamma_i = 2k_i R P_i \gamma_i^2. \tag{2.2}$$

The penetration factor which will be discussed in section 2.1.2 is denoted P_i, and the reduced width of the nuclear state γ_i^2 satisfies the condition $\gamma_i^2 \leq 1$. The reduced width corrects for the probability that a given state may have more than one configuration. The following sections outline the calculations for reaction rates in a typical stellar environment that occur via tunnelling.

2.1.1 Energy of a Star

All the variety of nuclei that were discussed in section 1.2 in the interior of a star are part of a stellar plasma, ionized and in thermal equilibrium. A common simplification to aid in the description of the interior of a star is to neglect interactions between particles and approximate it as an ideal gas [4]. Using this simplification, the velocity distribution of the nuclei in this state follows a Maxwell-Boltzmann distribution.

$$\phi(v) = 4\pi v^2 \left(\frac{m}{2\pi kT}\right)^{3/2} e^{\left(\frac{-mv^2}{2kT}\right)}. \tag{2.3}$$

where the particle mass and velocity are given by m and v respectively, the temperature is T and k is Boltzmann's constant. In terms of energy, the Maxwell-Boltzmann distribution is of the form

$$\phi(E) \propto E e^{\left(\frac{-E}{kT}\right)} \tag{2.4}$$

The peak of the distribution is located at a value of $E = kT$. The peak value of the curve represents the energy at which any given particle has the highest probability of being found. Solar core temperatures on the order of 1.57×10^7 K result in the peak of the Maxwell-Boltzmann distribution being located at an energy of

$$E_{peak} \approx 1.4\, keV. \tag{2.5}$$

With the Coulomb barrier between two protons on the order of hundreds of keV there is, classically, little chance of solar particles overcoming the Coulomb barrier.

2.1.2 Tunnelling in a Star

In 1927 Friedrich Hund first took notice of tunnelling when calculating the ground state of the double-well potential. The first application came shortly after, when in 1928 both George Gamow, and independently Ronald Gurney and Edward Condon explained alpha decay with the use of quantum tunnelling [22].

A classical comparison of quantum tunnelling is that of a ball rolling over a hill. If the initial energy of the ball is not sufficient to surmount the hill it would never be able to reach the other side and it would simply roll back down. In quantum mechanics however, a particle can, with a very small probability, tunnel through to the other side, thus crossing the barrier even though it did not have enough energy to do so classically. The difference is due to the character of matter in quantum mechanics, namely the wave-particle duality of matter.

In a star such as the Sun, core temperatures are on the order of 1.5×10^7 K, which corresponds to an energy of order 1 keV as shown in Equation 2.5. With Coulomb barrier energies between even the lightest nuclei on the order of a few hundred keV the requirement for quantum tunnelling is apparent. In addition to the Coulomb barrier, the centrifugal barrier must also be penetrated if present. The Coulomb barrier is given by the equation

$$V_C(r) = \frac{Z_1 Z_2 e^2}{r}, \tag{2.6}$$

for two particles of charge Z_1 and Z_2 and separation r. The centrifugal barrier is expressed as

$$V_{cf}(r) = \frac{L^2}{2\mu r^2} = \frac{\ell(\ell+1)\hbar^2}{2\mu r^2}. \tag{2.7}$$

where ℓ is the quantum number of the orbital angular momentum and μ the reduced mass. The wave function for a particle in such a potential may be written in the form

$$\psi(r, \theta, \phi) = \frac{U_\ell(r)}{r} Y_{\ell m}(\theta, \phi), \tag{2.8}$$

where $Y_{\ell m}(\theta, \phi)$ are spherical harmonics. The probability of the particle tunnelling through both barriers is known as its penetration factor, defined as P_ℓ

$$P_\ell(E, R_n) = \frac{|U_\ell(\infty)|^2}{|U_\ell(R_n)|^2} \tag{2.9}$$

where $U_\ell(\infty)$ represents the free particle at infinity and $U_\ell(R_n)$ represents the reduced radial wavefunction of the particle at the nuclear radius of the compound nucleus.

The penetration factor from Equation 2.9 involves radial wavefunctions only at distances r $\geq R_n$, and since only the ratio of wave functions outside the nucleus is required, the penetration factor is independent of the nuclear potential. The solution of the Schrödinger equation in this instance is a linear combination of the regular and irregular Coulomb wavefunctions, F_ℓ and G_ℓ.

$$U_\ell(R_n) = AF_\ell^2 + BG_\ell^2, \tag{2.10}$$

for constants A and B. Since $U_\ell(R_n)$ must be an outgoing wave the constants must satisfy the condition $A = iB$, and the penetration factor is

$$P_\ell(E, R_n) = \frac{1}{F_\ell(E, R_n)^2 + G_\ell(E, R_n)^2}. \tag{2.11}$$

For energies much less than the Coulomb barrier such as in the stellar core, the penetration factor, P_ℓ, can be approximated by the zero angular momentum solution [4]

$$P_0 \approx exp\left(-2\pi\eta\right), \tag{2.12}$$

where η is the Sommerfeld parameter given by $\eta = Z_1 Z_2 e^2/\hbar v$ for two particles of charge $Z_1 e$ and $Z_2 e$, and their relative speed v. In this form the penetration factor is known as the Gamow Factor. I will return to this in section 2.1.4 after introducing the astrophysical S-factor.

2.1.3 Astrophysical S-Factor

Nuclear fusion reactions between charged particles in a star are hindered by the Coulomb barrier, requiring quantum tunnelling through the potential barrier for them to proceed. The resulting cross sections are extremely small and are not easily measured in an experiment. For non resonant reactions the cross section, σ, is strongly dependent on the center of mass energy E and drops rapidly with decreasing energy due to the penetrability of the Coulomb barrier. By factorizing out the strong energy dependence of the cross section due to the penetration factor and leaving a function that is relatively constant at low energy, an experiment can be performed at higher energies and the results extrapolated down to zero energy with only a small error introduced. The astrophysical S-factor, $S(E)$, is thus defined by

$$\sigma(E) = \frac{1}{E} e^{-2\pi\eta} S(E), \tag{2.13}$$

which should only vary slightly with energy when compared to the factored elements. The $1/E$ factor is a geometrical factor and is associated with the wavelength of the incoming particle. The exponential factor is the same as shown in Equation 2.12 and represents the penetrability through the Coulomb barrier.

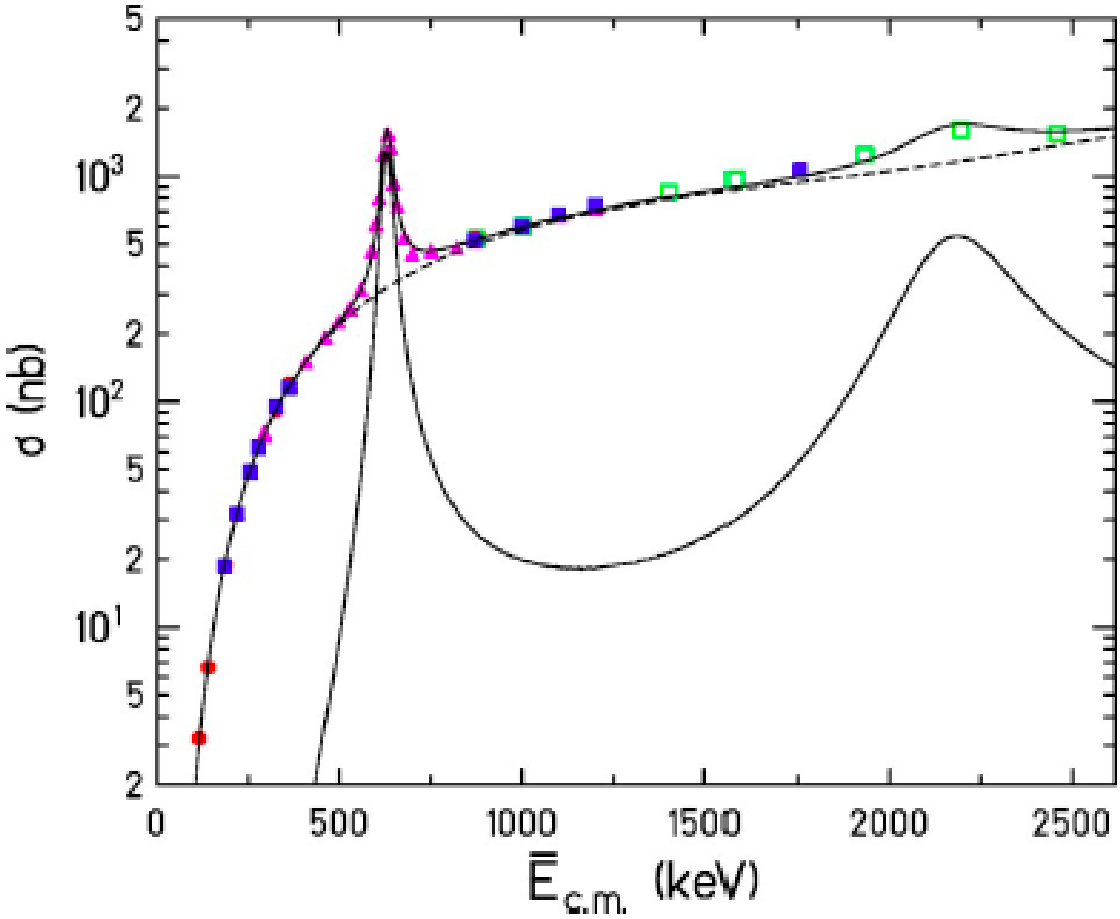

Figure 2.1: The cross section for the ^{7}Be(p,γ)^{8}B reaction from Reference [23]. The coloured points represent data from three experiments. The solid curve is a scaled calculation using the non-resonant Descouvemont and Baye (DB) theory plus fitted 1^{+} and 3^{+} resonances. The dashed curve is the DB fit only, while the lower solid line is the resonant contribution.

In Figure 2.1 the cross section for the ^{7}Be(p,γ)^{8}B reaction is shown. As the centre of mass energy drops below 500 keV the cross section falls off steeply due to the decreased penetrability, while the S-factor, shown in Figure 2.2, remains fairly constant over the entire energy range allowing much easier extrapolation down to zero energy.

2.1.4 The Gamow Window

Section 2.1.1 introduced the idea of approximating the energy distribution of a stellar plasma by a Maxwell-Boltzmann distribution (Equation 2.3). A useful quantity to define is the reaction rate between two particles

$$r_{12} = \frac{1}{1+\delta_{12}} n_1 n_2 \langle \sigma v \rangle, \tag{2.14}$$

where the quantity $\langle \sigma v \rangle$ is the thermally averaged reaction rate per particle pair and is defined by

$$\langle \sigma v \rangle = \int_0^\infty \sigma(E)\phi(v) v dv. \tag{2.15}$$

By substituting the expression for the Maxwell-Boltzmann distribution from Equation 2.3 into this equation and expressing it in terms of energy we have

$$\langle \sigma v \rangle = \sqrt{\frac{8}{\pi\mu(kT)^3}} \int_0^\infty E\sigma(E) e^{-\frac{E}{kT}} dE. \tag{2.16}$$

The reaction rate per particle pair can then be written using the S-factor from Equation 2.13 and the integral becomes

$$\langle \sigma v \rangle = \sqrt{\frac{8}{\pi\mu(kT)^3}} \int_0^\infty S(E) e^{\left(-\frac{E}{kT} - \sqrt{\frac{E_G}{E}}\right)} dE, \tag{2.17}$$

where the energy constant E_G is given by

$$E_G = 4\pi^2 \eta^2 E. \tag{2.18}$$

The two exponentials in Equation 2.17 are dominant at opposite ends of the energy spectrum, with the $e^{\sqrt{-E_G/E}}$ term small at low energies, and the $e^{-E/kT}$ term small at higher energies. The overlap of these two functions produces the peak shown in Figure 2.3,

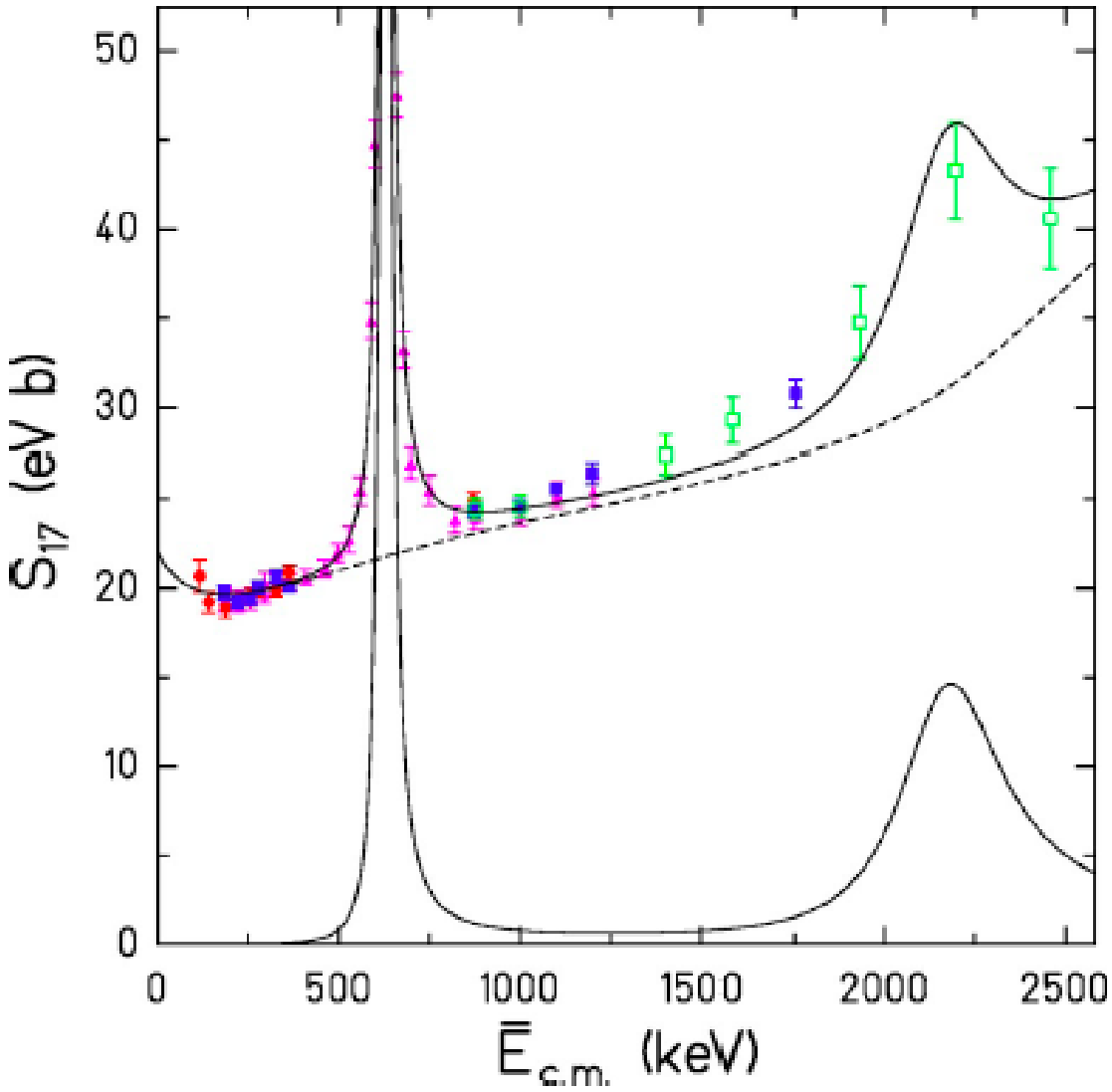

Figure 2.2: The S-factor for the ^{7}Be(p,γ)^{8}B reaction from Reference [23]. The solid curve is a scaled calculation using the non-resonant Descouvemont and Baye (DB) theory plus fitted 1^{+} and 3^{+} resonances. The dashed curve is the DB fit only, while the lower solid line is the resonant contribution.

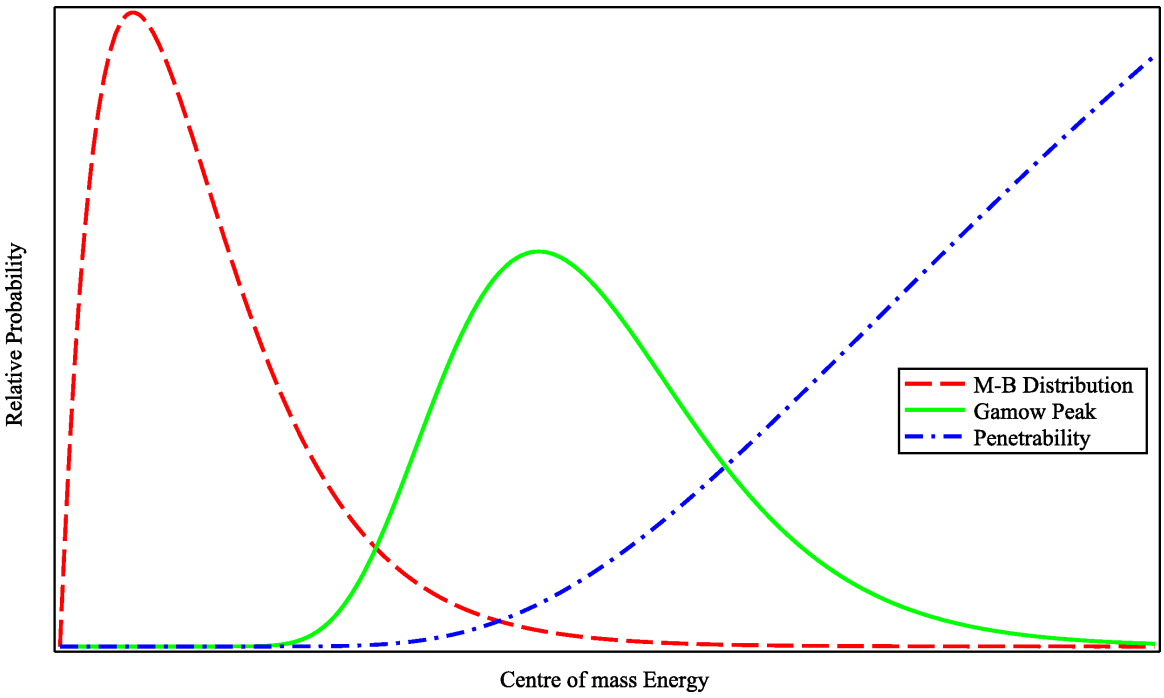

Figure 2.3: Overlap of the Maxwell-Boltzmann distribution with the penetration factor to form the Gamow peak.

referred to as the Gamow peak. The Gamow peak has a maximum at an energy E_0 given by

$$E_0 = \left(\frac{E_G k^2 T^2}{4}\right)^{\frac{1}{3}}. \tag{2.19}$$

If this peak is approximated as a Gaussian, the width of the peak is calculated as

$$\Delta = \frac{4}{3^{1/2}}(E_0 kT)^{1/2}. \tag{2.20}$$

The Gamow peak provides an effective region for nuclear reactions to occur which are below the threshold energy of the Coulomb barrier. This energy window, defined by

$$E = E_0 \pm \frac{\Delta}{2}, \tag{2.21}$$

is often referred to as the Gamow window which represents the most effective energy region for a thermonuclear reaction to occur.

2.2 Scattering Theory

The time independent Schrödinger equation describes the wavefunctions of stationary states, such as orbitals and standing waves. It is also used to solve for the cross section of reactions in terms of the interactions between reacting nuclei. To develop scattering theory I will start by solving the time-independent Schrödinger equation for a simplified case of a central potential.

2.2.1 Schrödinger Equation for a Central Potential

The time-independent Schrödinger equation can be written as

$$\left[-\frac{\hbar^2}{2\mu}\nabla^2_{\mathbf{r}} + V(\mathbf{r})\right]\psi(\mathbf{r}) = E\psi(\mathbf{r}). \tag{2.22}$$

The presence of a purely central potential, $V(\mathbf{r}) \rightarrow V(r)$, makes the choice of working in spherical coordinates (r, θ, ϕ) appropriate. In this case the Laplacian takes the form,

$$\nabla^2 = \frac{1}{r^2}\frac{\partial}{\partial r}\left(r^2\frac{\partial}{\partial r}\right) + \frac{1}{r^2\sin\theta}\frac{\partial}{\partial\theta}\left(\sin\theta\frac{\partial}{\partial\theta}\right) + \frac{1}{r^2\sin^2\theta}\frac{\partial^2}{\partial\phi^2}. \tag{2.23}$$

Solving the time independent Schrödinger equation is simplified by separation of variables, where

$$\psi(r,\theta,\phi) = R(r)\Theta(\theta)\Phi(\phi). \tag{2.24}$$

Choosing the separation constants, ℓ and m_ℓ should be done with some foresight, as they correspond to the orbital angular momentum quantum numbers. Combining equations 2.22, 2.23, and 2.24 results in three separate differential equations for the functions $R(r)$, $\Theta(\theta)$, and $\Phi(\phi)$:

$$\frac{1}{r^2}\frac{d}{dr}\left(r^2\frac{d}{dr}\right)R(r) = \left[\frac{\ell(\ell+1)}{r^2} + \frac{2\mu}{\hbar^2}\left[(V(r)-E)\right]\right]R(r) \tag{2.25a}$$

$$\sin\theta\frac{d}{d\theta}\left(\sin\theta\frac{d}{d\theta}\right)\Theta(\theta) = \left[m_\ell^2 - \ell(\ell+1)\sin^2\theta\right]\Theta(\theta) \tag{2.25b}$$

$$\frac{d^2\Phi(\phi)}{d\phi^2} = -m_\ell^2\Phi(\phi) \tag{2.25c}$$

The solutions to Equation 2.25c are by far the simplest, giving:

$$\Phi(\phi) = e^{im_\ell\phi} \tag{2.26}$$

with requirements that m_ℓ be an integer. Solutions to Equation 2.25b are of the form

$$\Theta_\ell^{m_\ell}(\theta) = \frac{(\sin\theta)^{|m_\ell|}}{2^\ell\ell!}\left[\frac{d}{d(\cos\theta)}\right]^{\ell+|m_\ell|}(\cos^2\theta-1)^\ell, \tag{2.27}$$

and are known as the associated Legendre functions ($P_\ell^{m_\ell}$) where ℓ is a non negative integer. Often the functions for Θ and Φ will be combined to form spherical harmonics,

$$Y_\ell^{m_\ell}(\theta,\phi) = \sqrt{\frac{(2\ell+1)}{4\pi}\frac{(\ell-m_\ell)!}{(\ell+m_\ell)!}}(-1)^{m_\ell}P_\ell^{m_\ell}(\cos\theta)e^{im_\ell\phi} \tag{2.28}$$

with requirements:

$$\ell = 0,1,2,3,\ldots$$
$$m_\ell = 0,\pm1,\pm2,\ldots,\pm\ell$$

Up until this point the solutions have been completely independent of the potential which only admits radial dependence. As such, the solutions already obtained for the

angular components of the Schrödinger equation given in Equation 2.28 will be the same for all potentials that have no angular dependence. The remaining radial equation which exhibits a central potential dependence can be slightly simplified with the introduction of a new function,

$$u(r) \equiv rR(r) \tag{2.29}$$

with which Equation 2.25a simplifies to

$$-\frac{\hbar^2}{2\mu}\frac{d^2u(r)}{dr^2} + \left[V(r) + \frac{\hbar^2}{2\mu}\frac{\ell(\ell+1)}{r^2}\right]u(r) = Eu(r). \tag{2.30}$$

This equation is often referred to as the radial Schrödinger equation. To further solve the radial Schrödinger equation an explicit function for the potential is required.

2.2.2 Differential Cross Section and Scattering amplitudes

In nuclear astrophysics a meeting point between experimental results and theoretical calculations is often the differential cross section. The differential cross section, $\frac{d\sigma}{d\Omega}$, describes the angular distribution of particles scattered by some potential V($\mathbf{r}$) for polar angles θ, measured from the beam direction, and azimuthal angle ϕ [24]. The scattering potential V($\mathbf{r}$) is the same as the one which appears in Equation 2.22. For scattering of one particle on another, $\mathbf{r}$ represents the relative coordinate between the two particles.

Expressing the differential cross section as the ratio of measured scattered angular flux, $\hat{j}_s$, in units of particles per unit time per steradian to incident flux, j_i, in units of particles per unit area per unit time gives the expression

$$\frac{d\sigma}{d\Omega} = \frac{\hat{j}_s}{j_i}. \tag{2.31}$$

The flux can be defined as a measure of the number of particles per unit time per unit area and is equivalent to the probability density of particles multiplied by the velocity.

$$\mathbf{j} = \mathbf{v}|\psi|^2. \tag{2.32}$$

An incident beam of well collimated, uniform energy particles, can be expressed as a plane wave. Choosing the coordinate system such that the beam is solely in the $+\hat{\mathbf{z}}$ direction with amplitude A, the incident wavefunction is expressed as

$$\psi_i = Ae^{ik_i z}. \tag{2.33}$$

Resulting in an incident flux of

$$j_i = |A|^2 \frac{\hbar k_i}{\mu}, \tag{2.34}$$

where $k_i = \mu v_i/\hbar$. The wavefunction for the scattered particles need only be expressed at values of large r, at the detector, outside the range of the scattering potential. An outgoing spherical wave will asymptotically be proportional to $e^{ik_f r}/r$ at large r, and vary with the angles θ and ϕ. Confining the angular dependence of the scattered wave in the function $f(\theta, \phi)$, the scattered wave can be written as

$$\psi_s = A\frac{f(\theta,\phi)e^{ik_f r}}{r}. \tag{2.35}$$

From this the scattered flux is found to be

$$j_s = |A|^2 \frac{\hbar k_f |f(\theta,\phi)|^2}{\mu r^2}. \tag{2.36}$$

The scattered angular flux per steradian is related to scattered flux by a factor of r^2 resulting in

$$\hat{j}_s = |A|^2 \frac{\hbar k_f |f(\theta,\phi)|^2}{\mu}. \tag{2.37}$$

Putting these expressions for the incident and scattered flux into Equation 2.31 results in a differential cross section of

$$\frac{d\sigma}{d\Omega} = \frac{k_f}{k_i}|f(\theta,\phi)|^2. \tag{2.38}$$

In the case of elastic scattering the wave number ratio is one and we are left with

$$\frac{d\sigma}{d\Omega} = |f(\theta,\phi)|^2. \tag{2.39}$$

The amplitude A of each of the functions is irrelevant as we see the differential cross section is independent of the overall normalization it provides. The function $f(\theta, \phi)$ is called the scattering amplitude which has units of length, and in general is complex valued [24].

2.2.3 Phase shifts

Consider the Schrödinger equation (2.22) with boundary conditions for a typical elastic scattering experiment. An incident flux j_i originating from a source hits a target, and a scattered flux j_s radiates outward in all directions. A solution of the form

$$\psi_{asym}(\mathbf{r}) = \psi_i(\mathbf{r}) + \psi_s(\mathbf{r}) \tag{2.40}$$

will exist where the incident wave, $\psi_i(\mathbf{r})$ represents the incident beam, and $\psi_s(\mathbf{r})$ is an outgoing scattered wave [25]. The label "asymptotic" is used to indicate that this is a solution located in free space outside the range of the interaction potential. Putting in the expression for the incident and scattered waves from equations 2.33 and 2.35 and setting the normalization to one we have

$$\psi_{asym}(\mathbf{r}) = e^{ikz} + f(\theta,\phi)\frac{e^{ikr}}{r}. \tag{2.41}$$

The solution to the Schrödinger equation worked out in section 2.2.1 can be expressed as a series of partial waves,

$$\psi(\mathbf{r}) = \sum_{\ell m} a_{\ell m} Y_\ell^m(\theta,\phi)\frac{u_\ell(r)}{r}, \tag{2.42}$$

with the spherical harmonics given in Equation 2.28 and the function $u(r)$ satisfying the radial Schrödinger equation in Equation 2.30. As previously shown, the incident wave can be expressed as a plane wave, which is the same solution as if the scattering potential were identically zero. The normalization of the incident wave was shown to cancel in the calculation of the differential cross section, and thus will be set to unity here as it will be of no consequence in further calculations. The plane wave solution can then be expanded as

$$\psi_i = e^{ik_i z} = \sum_\ell (2\ell+1) i^\ell j_\ell(kr) P_\ell(\cos\theta), \tag{2.43}$$

where j_ℓ is a spherical Bessel function, and P_ℓ is a Legendre polynomial. The set of Legendre polynomials forms an orthogonal and complete set over angles $0 \leq \theta \leq \pi$, satisfying the orthogonality and normalization conditions [24]

$$\int_0^\pi P_\ell(\cos\theta) P_{\ell'}(\cos\theta)\sin\theta d\theta = \frac{2}{2\ell+1}\delta_{\ell\ell'} \tag{2.44}$$

Note the radial dependence of Equation 2.43 is located only in the Bessel function $j_\ell(kr)$, thus a similar solution to Equation 2.22 with a scattering potential will be of the form

$$\psi = \sum_\ell (2\ell+1) i^\ell A_\ell R_\ell(r) P_\ell(\cos\theta), \tag{2.45}$$

where the radial function $R_\ell(r)$ satisfies the partial wave equation,

$$\frac{1}{r^2}\frac{d}{dr}r^2\frac{d}{dr}R_\ell(r) + \left[k^2 - U(r) - \frac{\ell(\ell+1)}{r^2}\right]R_\ell(r) = 0, \tag{2.46}$$

with substitutions $k = (2\mu E/\hbar^2)^{1/2}$ and $U(r) = (2\mu/\hbar^2)V(r)$. Outside the range of the potential $U(r)$, this differential equation is satisfied by the spherical Bessel functions, $j_\ell(kr)$ and $n_\ell(kr)$. Since we need only consider the solutions outside the range of the potential when solving for the differential cross section we can take the solution as a linear combination of the two functions [25],

$$R_\ell(r) = \cos(\delta_\ell) j_\ell(kr) - \sin(\delta_\ell) n_\ell(kr). \tag{2.47}$$

In the limit of $kr \to \infty$ the asymptotic forms of the Bessel functions are

$$j_\ell(kr) \simeq \frac{\sin(kr - \frac{1}{2}\pi\ell)}{kr}, \tag{2.48a}$$

$$n_\ell(kr) \simeq \frac{-\cos(kr - \frac{1}{2}\pi\ell)}{kr}, \tag{2.48b}$$

giving rise to the corresponding asymptotic expression for $R_\ell(r)$,

$$R_\ell(r) \simeq \frac{\sin(kr - \frac{1}{2}\pi\ell + \delta_\ell)}{kr}. \tag{2.49}$$

Comparing the asymptotic limits of the zero scattering solution given in Equation 2.43 and the scattering solution of Equation 2.45, the apparent effect a short range scattering potential has is expressed as a phase shift of the radial function by the factor δ_ℓ at large r. Substituting into Equation 2.41 the results of equations 2.43 and 2.45 with corresponding asymptotic limits given by equations 2.48a and 2.49 respectively, and using Euler's formula to express the sine functions in terms of complex exponentials we obtain

$$\sum_{\ell}(2\ell+1)i^{\ell}P_{\ell}(\cos\theta)A_{\ell}\frac{e^{i\left(kr-\frac{1}{2}\pi\ell+\delta_{\ell}\right)}+e^{-i\left(kr-\frac{1}{2}\pi\ell+\delta_{\ell}\right)}}{2ikr} = \sum_{\ell}(2\ell+1)i^{\ell}P_{\ell}(\cos\theta)\frac{e^{i\left(kr-\frac{1}{2}\pi\ell\right)}+e^{-i\left(kr-\frac{1}{2}\pi\ell\right)}}{2ikr}+f(\theta,\phi)\frac{e^{ikr}}{r}. \tag{2.50}$$

Collecting term as coefficients of the e^{-ikr} and e^{ikr} terms yields two separate equations which due to orthogonality must each be satisfied. Collecting terms for the negative exponential yields the equation,

$$\sum_{\ell}(2\ell+1)i^{\ell}P_{\ell}(\cos\theta)A_{\ell}e^{i\left(\frac{1}{2}\pi\ell-i\delta_{\ell}\right)} = \sum_{\ell}(2\ell+1)i^{\ell}P_{\ell}(\cos\theta)e^{i\frac{1}{2}\pi\ell}, \tag{2.51}$$

taking advantage of the linear independence of the Legendre polynomials this expression requires

$$A_{\ell}=e^{i\delta_{\ell}}, \tag{2.52}$$

to be satisfied. Using this result and collecting terms for the positive exponential,

$$\sum_{\ell}(2\ell+1)i^{\ell}P_{\ell}(\cos\theta)e^{i\delta_{\ell}}e^{i\left(-\frac{1}{2}\pi\ell+i\delta_{\ell}\right)} = \sum_{\ell}(2\ell+1)i^{\ell}P_{\ell}(\cos\theta)e^{-i\frac{1}{2}\pi\ell}+\frac{f(\theta,\phi)}{r}. \tag{2.53}$$

Solving this equation for the scattering amplitude and again using the linear independence of the Legendre polynomials results in an expression for the scattering amplitude,

$$f(\theta,\phi)=\frac{1}{2ik}\sum_{\ell}(2\ell+1)i^{\ell}P_{\ell}(\cos\theta)e^{-i\frac{1}{2}\pi\ell}\left[e^{2i\delta_{\ell}}-1\right]. \tag{2.54}$$

Introducing the partial wave transfer matrix (T-matrix) element defined as

$$T_{\ell}=e^{i\delta_{\ell}}\sin\delta_{\ell}, \tag{2.55}$$

with the relationship $e^{-i\frac{1}{2}\pi\ell}=i^{-\ell}$, expression 2.54 is further simplified to

$$f(\theta)=\frac{1}{k}\sum_{\ell}(2\ell+1)P_{\ell}(\cos\theta)T_{\ell}. \tag{2.56}$$

Assuming no spin polarization, the ϕ dependence may be dropped due to the spherical symmetry. Putting this result into Equation 2.39 gives an expression for the differential cross section in terms of the T-matrix,

$$\frac{d\sigma}{d\Omega} = \left| \frac{1}{k} \sum_{\ell} (2\ell + 1) P_{\ell}(\cos\theta) T_{\ell} \right|^2 \tag{2.57}$$

or in terms of the phase shift

$$\frac{d\sigma}{d\Omega} = \left| \frac{\ell}{k} \sum_{\ell} (2\ell + 1) P_{\ell}(\cos\theta) e^{i\delta_{\ell}} \sin\delta_{\ell} \right|^2 \tag{2.58}$$

Integrating the differential cross section over all directions and making use of the orthonormality and normalization condition of the Legendre polynomials shown in Equation 2.44 , the total elastic cross section is

$$\sigma = \frac{4\pi}{k^2} \sum_{\ell} (2\ell + 1) \sin^2 \delta_{\ell}. \tag{2.59}$$

We will now look at transfer reactions from a distorted wave Born approximation (DWBA) approach.

2.2.4 DWBA

In the Born approximation (BA), solutions of a scattering potential are obtained by treating the scatterer as a perturbation to free space or to a homogeneous medium. While in the simplest cases of BA the incident waves are plane waves, in the DWBA incident waves are solutions to a part, V_1, of the potential $V = V_1 + V_2$, where V_2 is treated as a perturbation to some potential V_1 that is easily solved by other methods.

As an example consider the transfer reaction,

$$X + A \rightarrow Y + B \tag{2.60}$$

where $X = Y + a$, and $B = A + a$ with a being the transferred particle. The scattering can be described in terms of the nuclei of the entrance partition, $X + A$, in which the projectile-target interaction will be given as

$$V_{XA} = V_{aA} + U_{YA}. \tag{2.61}$$

The first part of the interaction, V_{Aa}, is the binding potential for the valence particle and the core A. The second potential, U_{YA}, is the core-core potential describing the scattering between the two cores. The binding potential is real valued, while the core-core potential may be complex. In this representation, known as the prior form, the transfer matrix from Equation 2.55 is given by

$$T_{prior}^{DWBA} = \langle \chi_f^{(-)} \phi_A \phi_B | \left(V_{Aa} + U_{YA} - U_i \right) | \chi_i^{(+)} \phi_Y \phi_X \rangle, \tag{2.62}$$

where χ_i and χ_f are the distorted waves in the initial and final channels, and the factors of ϕ are square integrable states of the participating nuclei. A similar expression can be written for the exit channel where the interaction is expressed in the form

$$V_{YB} = V_{Ya} + V_{YA}. \tag{2.63}$$

This is referred to as the post form of the T-matrix

$$T_{post}^{DWBA} = \langle \chi_f^{(-)} \phi_A \phi_B | \left(V_{Ya} + V_{YA} - U_f \right) | \chi_i^{(+)} \phi_Y \phi_X \rangle. \tag{2.64}$$

The conventional DWBA makes the assumption that both the entrance and exit channel wave functions use the corresponding one-channel optical potentials, U_i and U_f, that fit the elastic scattering. These entrance and exit optical potentials are used to generate the corresponding distorted waves χ_i and χ_f and may be complex. The scattering amplitude can then be calculated from

$$f(\theta) = -\frac{\mu}{2\pi\hbar^2} T, \tag{2.65}$$

and should be the same regardless of the use of the prior or post form. Using the relationship between the scattering amplitude and differential cross section from Equation 2.39, the differential cross section can then be calculated.

2.2.5 Partial-wave expansions

The total wavefunction given by

$$\Psi_{\kappa J_T}^{M_T} = |(L J_p) J, J_t; J_T \rangle, \tag{2.66}$$

with projectile spin J_p, target spin J_t, relative partial wave orbital angular momentum L, and total system angular momentum J_T is represented in partial waves using the coupling order

$$\mathbf{L} + \mathbf{J_p} = \mathbf{J}; \;\; \mathbf{J} + \mathbf{J_t} = \mathbf{J_T}. \tag{2.67}$$

In each partition the partial wave expansion of the wavefunction is

$$\begin{aligned}\Psi^{M_T}_{\kappa J_T} = \sum_{LJ_pJJ_tM\mu_pM_j\mu_t} & \phi_{J_p}(\xi_p)\phi_{J_t}(\xi_t) i^L Y^M_L(\mathbf{R}_\kappa) \\ & \frac{1}{R_\kappa} f_\alpha(R_\kappa)\langle LMJ_p\mu_p|JM_J\rangle\langle LM_JJ_t\mu_t|J_TMT\rangle.\end{aligned} \tag{2.68}$$

where ξ_p and ξ_t are the internal coordinates of the projectile and target. The term $f_\alpha(R_\kappa)$ is the radial wave function where the set $\{\kappa, (LJ_p)J, J_t; J_T\}$ has been abbreviated by the single variable α. The i^L factors are included to simplify the spherical Bessel expansion of the incoming plane wave [26].

In a direct reaction all channels, or modes of break-up must be considered. Each channel will have a wavefunction and thus a solution to the Schrödinger equation. Adopting the coupled reaction channels (CRC) formalism the coupled partial-wave equations are of the form

$$\begin{aligned}\left[E_{\kappa pt} - T_{\kappa L}(R_\kappa) - U_\kappa(R_\kappa)\right] f_\alpha(R_\kappa) = & \sum_{\alpha',\Gamma>0} i^{L'-L} V^\Gamma_{\alpha:\alpha'}(R_\kappa) f_{\alpha'}(R_\kappa) \\ & + \sum_{\alpha',\kappa'\neq\kappa} i^{L'-L} \int_0^{R_m} V_{\alpha:\alpha'}(R_\kappa, R_{\kappa'}) f_{\alpha'}(R_{\kappa'}) dR_{\kappa'}.\end{aligned} \tag{2.69}$$

where the partial-wave kinetic energy operator is

$$T_{\kappa L}(R_\kappa) = -\frac{\hbar^2}{2\mu_\kappa}\left(\frac{d^2}{dR^2_\kappa} - \frac{L(L+1)}{R^2_\kappa}\right). \tag{2.70}$$

The term $U_\kappa(R_\kappa)$ is the diagonal optical potential with nuclear and Coulomb components, and R_m is a radius limit larger than the ranges of $U_\kappa(R_\kappa)$ and of the coupling terms.

The local coupling interactions of multipolarity Γ are given by $V^\Gamma_{\alpha:\alpha'}(R_\kappa)$, and the non-local couplings between mass partitions are given by $V_{\alpha:\alpha'}(R_\kappa, R_{\kappa'})$. They are defined as

$$V_{\alpha:\alpha'} = \langle \phi_{p\alpha}\phi_{t\alpha}|H_m - E|\phi_{p\alpha'}\phi_{t\alpha'}\rangle \tag{2.71}$$

and for the non-local case the post and prior forms are

$$\begin{aligned}\langle\phi_{p\alpha}\phi_{t\alpha}|H_m - E|\phi_{p\alpha'}\phi_{t\alpha'}\rangle = \\ V^{post}_{\alpha:\alpha'} + [T_\alpha + U_\alpha - E_\alpha]\, K_{\alpha:\alpha'}, \\ \text{and} \\ V^{prior}_{\alpha:\alpha'} + K_{\alpha:\alpha'}\left[T_{\alpha'} + U_{\alpha'} - E_{\alpha'}\right].\end{aligned} \tag{2.72}$$

where

$$\begin{aligned} V^{post}_{\alpha:\alpha'} &= \langle\phi_{p\alpha}\phi_{t\alpha}|V_\alpha|\phi_{p\alpha'}\phi_{t\alpha'}\rangle, \\ V^{prior}_{\alpha:\alpha'} &= \langle\phi_{p\alpha}\phi_{t\alpha}|V_{\alpha'}|\phi_{p\alpha'}\phi_{t\alpha'}\rangle, \\ K_{\alpha:\alpha'} &= \langle\phi_{p\alpha}\phi_{t\alpha}|\phi_{p\alpha'}\phi_{t\alpha'}\rangle. \end{aligned} \tag{2.73}$$

The wavefunction overlap operator $K_{\alpha:\alpha'}$ arises from the non-orthogonality between the transfer basis states defined around different centers in different mass partitions. The scattering theory discussed up to this point has been very general; the next section will deal with more specific scattering mechanisms important for this study.

2.3 Indirect Methods

Many capture reactions that take place in a stellar environment prove difficult to measure at astrophysically relevant energies in a laboratory. The Coulomb repulsion between the particles makes the cross section at these low energies extremely small, making experiments at these energies practically impossible. One method of bypassing this hurdle is to develop an indirect method of inferring the desired reaction rate from measurements at high energies.

The astrophysical S-factor discussed in section 2.1.3 is often determined at higher energies and extrapolated down to zero energy. This method is not ideal as some error in extrapolation is introduced. Another method of determining the S-factor at zero energy is from the asymptotic normalization coefficient (ANC) which is dependent on the bound state ANC but not on the continuum properties [24].

2.3.1 Transfer Reactions

There are two basic types of transfer reactions: pickup and stripping reactions. A pickup reaction is a reaction where the projectile gains, or picks up, a valence nucleon or cluster of

nucleons from the target. In a stripping reaction the target nucleus gains, or strips, a valence nucleon or cluster of nucleons from the projectile. Both describe the same basic reaction of transferring up to several nucleons between projectile and target where the difference is simply the direction in which the transfer proceeds.

Consider a stripping reaction where a projectile transfers a neutron to a target nucleus with the coordinate system shown in Figure 2.4. In the case of this stripping reaction the

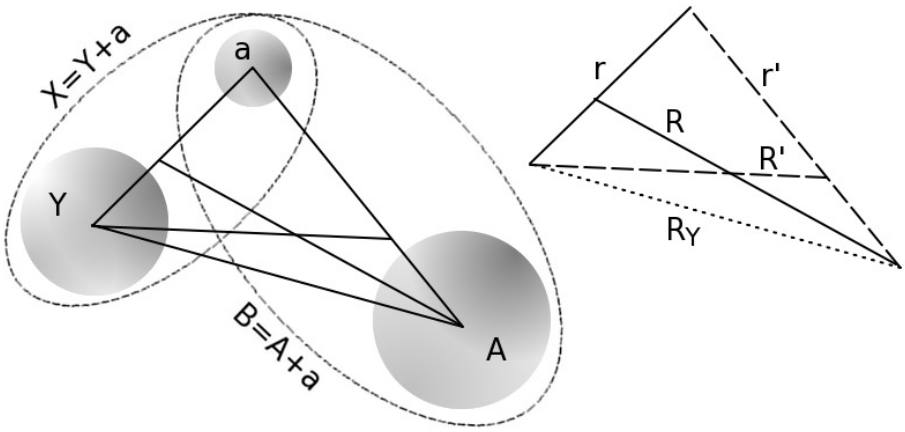

Figure 2.4: Stripping reaction with associated coordinates for the reaction $X + A \rightarrow Y + B$ where $X = Y + a$, and $B = A + a$ with a being the transferred particle.

initial bound state of the projectile and the final bound state of the residual nucleus will satisfy the eigenvalue equations:

$$[H_X - \epsilon_X]\,\phi_X(\mathbf{r}) = 0, \tag{2.74a}$$

$$[H_B - \epsilon_B]\,\phi_B(\mathbf{r}') = 0, \tag{2.74b}$$

for Hamiltonians $H_X = T_{\mathbf{r}} + V_X(\mathbf{r})$ and $H_B = T_{\mathbf{r}'} + V_B(\mathbf{r}')$, while the difference of the eigenvalues ϵ_X and ϵ_B gives the Q-value for the reaction. From the matrix elements of the Hamiltonian for the three bodies involved the dynamical details of the transfer coupling arise [24]. This Hamiltonian for the two cores, Y and A, and the valence particle, a, shown in Figure 2.4 can be written as

$$H = T_{\mathbf{r}} + T_{\mathbf{R}} + V_X(\mathbf{r}) + V_B(\mathbf{r}') + U_{AY}(\mathbf{R}_Y), \tag{2.75}$$

where $U_{AY}(\mathbf{R}_Y)$ is the core-core optical potential. The Hamiltonian can be expanded in both prior and post forms as discussed in section 2.2.4, producing identical solutions. If the wavefunctions are all described by only s-wave ($\ell = 0$) states, the remnant term can be neglected, and the interaction potential has a small range, then at sub-Coulomb-barrier incident energies the details of the nuclear potentials become irrelevant. The radial wave equation, for transfer reactions, can then be simplified to

$$u_{\ell'}(R')D_0 \left[1 + \rho_{eff}^2 \frac{2\mu_X}{\hbar^2}\epsilon_X\right] = D u_{\ell'}(R'), \tag{2.76}$$

where ρ_{eff} parametrizes the finite-range effective radius of the rate of oscillation of the source wave function $\psi_i(R)$, and μ_X is the reduced mass of the valence particle in the projectile. The effective zero-range coupling constant for sub-Coulomb transfer, D, is given by

$$D = (1 + k_X^2 \rho_{eff}^2) D_0, \tag{2.77}$$

for a bound-state wave number $k_X = \sqrt{2\mu_X \epsilon_X/\hbar^2}$ of the projectile.

From the details of the projectile bound state the parameters D_0 and D may be derived [24]. The zero-range constant is defined by the integral

$$D_0 = \sqrt{4\pi} \int_0^\infty r V_0(r) u_0(r) dr, \tag{2.78}$$

and the parameter D can be found from the integral

$$D = \sqrt{4\pi} \int_0^\infty \frac{\sinh(k_X r)}{k_X} V_0(r) u_0(r) dr. \tag{2.79}$$

Comparing equations 2.78 and 2.79, as the range of the potential becomes smaller the value of D approaches that of D_0. The finite-range effective radius, ρ_{eff}, of Equation 2.77 is a measure of the mean radius of the potential $V_0(r)$. It is also important to note that the parameter D reflects the asymptotic strength of the wavefunction $u_0(r)$ as $r \to \infty$, as it is the magnitude of this tail which is important in sub-Coulomb reactions:

$$u_0(r) \xrightarrow[r\to\infty]{} \frac{2\mu_X}{\hbar^2} \frac{1}{\sqrt{4\pi}} D e^{-k_X r}. \tag{2.80}$$

The strength of the tail of the wavefunction is an important term which will be discussed in the next section.

2.3.2 Asymptotic Normalization Coefficients

Consider again the generic transfer reaction illustrated in Figure 2.4.

$$X + A \rightarrow Y + B, \tag{2.81}$$

where $X = Y + a$, $B = A + a$, and a is the transferred particle. Proceeding in a DWBA framework for analysis, the amplitude of this reaction summed over all spin projections M_a of the transferred particle a at a relative kinetic energy E_i and center of mass reaction angle θ is

$$M(E_i, \cos\theta) = \sum_{M_a} \langle \chi_f^{(-)} I_{Aa}^{B}(\mathbf{r}_{Aa}) | \Delta V | I_{Ya}^{X}(\mathbf{r}_{Ya}) \chi_i^{(+)} \rangle, \tag{2.82}$$

where $\chi_i^{(+)}$ and $\chi_f^{(-)}$ are the distorted waves in the initial and final channels, ΔV is the transition operator, or interaction potential, which can be expressed in both the post and prior forms,

$$\Delta V_{post} = V_{Ya} + U_{YA} - U_f, \tag{2.83a}$$

$$\Delta V_{prior} = V_{Aa} + U_{YA} - U_i. \tag{2.83b}$$

The first term of equations 2.83a and 2.83b, V_{Ya} and V_{Aa}, is a binding potential between the core nucleus and the valence particle, while the U_{YA} terms are the core-core potentials. The final term of each equation is the optical potential, which can be written for the initial and final channels as U_i and U_f respectively. The binding potentials are real, but the core-core potential and optical potentials will typically have both real and imaginary components.

The final terms in Equation 2.82, of the form $I_{\beta\gamma}^{\alpha}(\mathbf{r}_{\beta\gamma})$, are the overlap functions of the bound state wavefunctions of particles α, β, and γ; where α is the bound state of particles β and γ. The overlap functions are given by the expression

$$
\begin{aligned}
I^{\alpha}_{\beta\gamma}(\mathbf{r}_{\beta\gamma}) &= \langle \phi_\beta(\xi_\beta)\phi_\gamma(\xi_\gamma)|\phi_\alpha(\xi_\beta,\xi_\gamma;\mathbf{r}_{\beta\gamma})\rangle \\
&= \sum_{\ell_\alpha m_{\ell_\alpha} j_\alpha m_{j_\alpha}} \langle J_\beta M_\beta j_\alpha m_{j_\alpha}|J_\alpha M_\alpha\rangle\langle J_\gamma M_\gamma \ell_\alpha m_{\ell_\alpha}|j_\alpha m_{j_\alpha}\rangle \\
&\qquad\qquad i^{\ell_\alpha} Y_{\ell_\alpha m_{\ell_\alpha}}(\hat{\mathbf{r}}_{\beta\gamma}) I^{\alpha}_{\beta\gamma\ell_\alpha j_\alpha}(r_{\beta\gamma}),
\end{aligned}
\tag{2.84}
$$

for bound state wavefunctions ϕ, with internal coordinates ξ which include spin-isospin variables, and the spin and spin projections J and M. The $\mathbf{r}_{\beta\gamma}$ parameter is the relative coordinate of nuclei β and γ, with $\hat{\mathbf{r}} = \mathbf{r}/r$. The values of j_α and m_{j_α} are the total angular momentum of particle γ and its projection in the nucleus $\alpha = (\beta\gamma)$. The orbital angular momentum and its projection of the relative motion between particle β and γ in the bound state of α are given by ℓ_α and m_{ℓ_α}, while the terms of the form $\langle j_1 m_1 j_2 m_2|j_3 m_3\rangle$ are Clebsch Gordan coefficients. The spherical harmonics, $Y_{\ell_\alpha m_{\ell_\alpha}}(\hat{\mathbf{r}}_{\beta\gamma})$, and the radial overlap function, $I^{\alpha}_{\beta\gamma\ell_\alpha j_\alpha}(r_{\beta\gamma})$, describe the angular and radial dependences respectively.

The radial overlap function is often approximated by a model wavefunction of the bound state α as

$$
I^{\alpha}_{\beta\gamma\ell_\alpha j_\alpha}(r_{\beta\gamma}) = A_{\beta\gamma\ell_\alpha j_\alpha}\phi_{n_\alpha\ell_\alpha j_\alpha}(r_{\beta\gamma}),
\tag{2.85}
$$

where $A_{\beta\gamma\ell_\alpha j_\alpha}$ is an amplitude that is related to the spectroscopic factor, $S_{\beta\gamma\ell_\alpha j_\alpha}$, by the relationship

$$
S_{\beta\gamma\ell_\alpha j_\alpha} = |A_{\beta\gamma\ell_\alpha j_\alpha}|^2.
\tag{2.86}
$$

Here we have introduced the spectroscopic factor, $S_{\beta\gamma\ell_\alpha j_\alpha}$, for the nucleus α in the configuration of $(\beta\gamma)$ with quantum numbers ℓ_α and j_α.

The reduced DWBA cross section, expressed as $\sigma^{DW}_{\ell_B j_B \ell_X j_X}$, is dependent upon the optical model parameters and geometric parametrization of the potentials used to reproduce the bound states. Expressing the differential cross section for the reaction of Equation 2.81 in terms of $\sigma^{DW}_{\ell_B j_B \ell_X j_X}$ results in

$$
\frac{d\sigma}{d\Omega} = \sum_{j_B j_X} S_{Aa\ell_B j_B} S_{Ya\ell_X j_X} \sigma^{DW}_{\ell_B j_B \ell_X j_X}.
\tag{2.87}
$$

Since the reduced DWBA cross section depends on the optical potential parameters and the geometric parameters of the potentials used to calculate the bound states, the extracted values of the phenomenological spectroscopic factors are also model dependent [27].

Spectroscopic factors are essentially defined by the overlap function between the wavefunctions of the nucleus X with its valence nucleon, a, and the wavefunction of the nucleus Y, where $X = Y + a$. The dominant contribution to the spectroscopic factor for peripheral transfer reactions comes from the surface and outer regions of the nuclei.

As a model independent quantity, the asymptotic normalization coefficient (ANC) can be used in the DWBA calculation without the same problems as the spectroscopic factor. Defining the ANC, $C^{\alpha}_{\beta\gamma\ell_\alpha j_\alpha}$, as the amplitude of the tail of the radial overlap function

$$I^{\alpha}_{\beta\gamma\ell_\alpha j_\alpha}(r_{\beta\gamma}) \xrightarrow[r_{\beta\gamma}>R_N]{} C^{\alpha}_{\beta\gamma\ell_\alpha j_\alpha} \frac{W_{-\eta_{\beta\gamma},\ell_\alpha+\frac{1}{2}}(-2\kappa_{\beta\gamma}r_{\beta\gamma})}{r_{\beta\gamma}}, \tag{2.88}$$

where R_N is the nuclear interaction radius between β and γ, $W_{-\eta_\alpha,\ell_\alpha+\frac{1}{2}}(-2\kappa_{\beta\gamma}r_{\beta\gamma})$ is the Whittaker function which describes the asymptotic behaviour of the bound state wavefunction of two particles. Where the wavenumber given by $\kappa_{\beta\gamma} = \sqrt{2\mu_{\beta\gamma}\epsilon_{\beta\gamma}}$ and the Sommerfeld parameter $\eta_{\beta\gamma}$ are of the bound state $\alpha = (\beta\gamma)$.

Defining the single particle ANC, b, as the amplitude of the tail of the bound-state wavefunction at large r gives the relation

$$\phi_{n_\alpha\ell_\alpha j_\alpha} \xrightarrow[r_{\beta\gamma}>R_N]{} b_{\beta\gamma\ell_\alpha j_\alpha} \frac{W_{-\eta_{\beta\gamma},\ell_\alpha+\frac{1}{2}}(-2\kappa_{\beta\gamma}r_{\beta\gamma})}{r_{\beta\gamma}}. \tag{2.89}$$

From equations 2.85, 2.88, and 2.89 the relationship between the ANC, the single particle ANC and the spectroscopic factor for the bound state α is obtained.

$$\left(C^{\alpha}_{\beta\gamma\ell j}\right)^2 = S_{\beta\gamma\ell j} b^2_{\beta\gamma\ell j}. \tag{2.90}$$

Two important properties of the DWBA analysis arise due to this condition. First, it guarantees the correct absolute normalization of the peripheral DWBA amplitude [27]. Secondly, the calculated DWBA differential cross section's dependence on the geometry of the bound state wavefunction is significantly reduced. To illustrate this, Equation 2.87 is rewritten using Equation 2.90

$$\frac{d\sigma}{d\Omega} = \sum_{j_B j_X} \frac{(C^{B}_{Aa\ell_B j_B})^2}{b^2_{Aa\ell_B j_B}} \frac{(C^{X}_{Ya\ell_X j_X})^2}{b^2_{Ya\ell_X j_X}} \sigma^{DW}_{\ell_B j_B \ell_X j_X}. \tag{2.91}$$

For peripheral reactions, only values where $r_{Ya} > R_X$ and $r_{Aa} > R_B$ will contribute to the DWBA radial integrals, where r_{Ya} and r_{Aa} are the separations, and R_X and R_B represent the nuclear interaction radii between the constituents of both nuclei X and B. Therefore, each

of the bound state wavefunctions entering the expression for $\sigma^{DW}_{\ell_{Bj_B}\ell_X j_X}$ can be approximated by its asymptotic form, with the product of the single particle ANCs containing the only dependence on the geometry of the bound state potentials. Reparameterizing, we may write the differential cross section as

$$\frac{d\sigma}{d\Omega} = \sum_{j_B j_X} (C^B_{Aa\ell_B j_B})^2 (C^X_{Ya\ell_X j_X})^2 R_{\ell_B j_B \ell_X j_X}, \tag{2.92}$$

where the factor

$$R_{\ell_B j_B \ell_X j_X} = \frac{\sigma^{DW}_{\ell_{Bj_B}\ell_X j_X}}{b^2_{Aa\ell_B j_B} b^2_{Ya\ell_X j_X}} \tag{2.93}$$

contains all the dependence on the geometry of the bound state potentials. This results in the parameterization of the peripheral reaction differential cross section in terms of the ANCs of the initial and final states, which are insensitive to the geometries of the bound state potentials, rather than the spectroscopic factors.

The ANC of any projectile or target bound-state wavefunction may also be expressed as the asymptotic coefficient of the Whittaker function, which, for uncharged particles is a decaying exponential [24].

$$u_\ell(r) \xrightarrow[r>R_n]{} C_\ell W_{-\eta,\ell+\frac{1}{2}}(-2k_p r) \approx C_\ell e^{-k_p r}, \tag{2.94}$$

where k_p is the bound-state wavenumber of the projectile or target.

Comparing Equation 2.94 to Equation 2.80 the ANC is related to the parameter D, the asymptotic strength of the wavefunction, by

$$C_\ell = \frac{2\mu_p}{\hbar^2} \frac{1}{\sqrt{4\pi}} D. \tag{2.95}$$

As was shown in section 2.3.1, transfer reactions at sub-Coulomb energies are dependent on the strength of the exponential tail of a bound-state wavefunction, and thus are dependent on the ANC.

2.3.3 Extraction of the ANC

Transfer reactions have been used extensively to extract spectroscopic factors and when peripheral, to extract ANC values [28]. Analyzing a transfer experiment using DWBA theory, the spectroscopic factors are extracted from the data by a ratio of the differential cross sections

$$\frac{\frac{d\sigma}{d\Omega}^{\text{exp}}}{\frac{d\sigma}{d\Omega}^{\text{theory}}} = S^{\text{exp}}. \tag{2.96}$$

Consider again the transfer reaction from section 2.2.4, $A(X,Y)B$, where $X = Y + a$ and $B = A + a$ with a being the transferred particle or cluster. The exact transfer matrix elements in the prior and post forms are

$$T^{exact}_{prior} = \langle \Psi^{(-)exact} | V_{Aa} + U_{YA} - U_i | \Phi_{I_Y:I_X}(\mathbf{r}_{Ya}) \chi_{\mathbf{k_i}}(\mathbf{R}_i) \rangle, \tag{2.97a}$$

$$T^{exact}_{post} = \langle \Phi_{I_A:I_B}(\mathbf{r}_{Aa}) \chi_{\mathbf{k_f}}(\mathbf{R}_f) | V_{Ya} + U_{YA} - U_f | \Psi^{(+)exact} \rangle. \tag{2.97b}$$

Replacing one of the exact solutions by a distorted wave multiplying a corresponding bound state, $\phi(\mathbf{r})\chi(\mathbf{R})$, will give the DWBA transfer matrix,

$$T^{DWBA}_{fi} = \langle \chi^{(-)}_f(\mathbf{R}_f) \Phi_{I_A:I_B}(\mathbf{r}_f) | V | \Phi_{I_Y:I_X}(\mathbf{r}_{Ya}) \chi_i(\mathbf{R}_i) \rangle, \tag{2.98}$$

where the transfer operator V contains the appropriate core-core (U_{YA}), binding (V_{Aa}, V_{Ya}), and optical (U_i, U_f) potentials for either a prior or post form. Inputting values for the required potentials allows a DWBA differential cross section to be calculated and compared to the experimental cross section to extract the spectroscopic factor from Equation 2.96. The spectroscopic factor along with the single particle ANC can be used in conjunction with Equation 2.90 to obtain a value for the ANC.

For the specific case of the ^{7}Be(p,γ)^{8}B reaction, the numerical relationship between $S_{17}(0)$ and the ^{8}B ANCs can be expressed by the relationship [29, 30],

$$S_{17}(0) = 38.6(C^2_{p_{1/2}}(^8\text{B}) + C^2_{p_{3/2}}(^8\text{B}))\,\text{eV b fm}. \tag{2.99}$$

This relationship arises from the purely peripheral nature of the reaction and the relationship between the overlap functions and the ANC described in Equation 2.88

Chapter 3

Experimental Procedure

In this chapter details on the experimental facilities and equipment used will be given. As well the reaction being studied will be discussed.

The experiment was performed using the TUDA (TRIUMF-U.K. detector array) chamber in the ISAC I facility at TRIUMF in Vancouver, Canada. Two different detectors were used in the TUDA chamber; a LEDA detector and an S2 detector. The Louvain-Edinburgh Detector Array [31] (LEDA) is a single sided silicon strip detector that was specifically designed for use with the TUDA chamber and the S2 is a double sided silicon strip detector.

3.1 TRIUMF

Founded in 1968 by Simon Fraser University, the University of British Columbia and the University of Victoria, TRIUMF is Canada's national laboratory for particle and nuclear physics and currently has 17 member universities located across Canada. The lab is based around a 520 MeV H^- cyclotron that is capable of producing a current exceeding 10^{12} H^- ions per second and delivering multiple beams at different energies simultaneously.

The lab was originally used for the production and study of mesons, but with the addition of the ISAC facilities many avenues of research with the production of radioactive ion beams have opened up.

3.2 RIB facilities

The two ISAC (Isotope Separator and ACcelerator) facilities utilize linear accelerators for post-acceleration of radioactive and stable ion beams to deliver the desired beam to a number of detectors such as DRAGON, 8pi, TITAN, and TUDA.

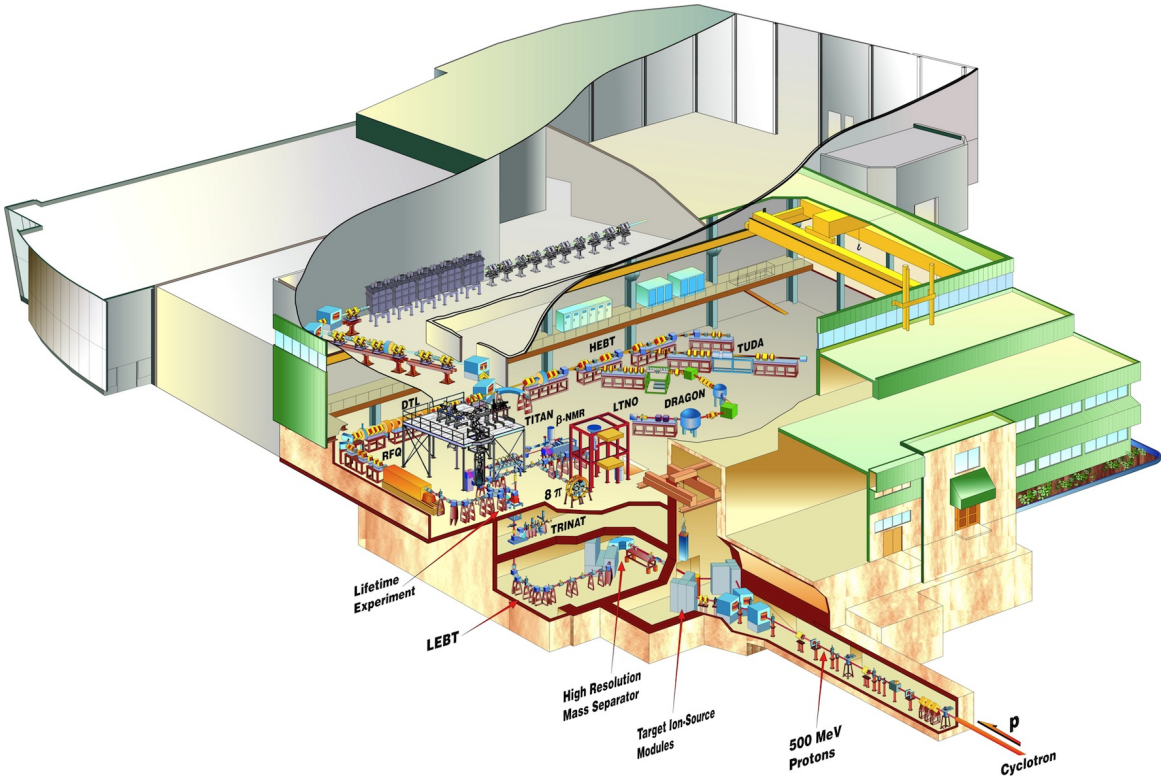

Figure 3.1: ISAC experimental hall

3.2.1 Beam Production

The radioactive ion beams used in the ISAC facilities are produced at ISAC using the ISOL (isotope separation on-line) technique. A suitable target such as silicon carbide, tantalum, or niobium is bombarded with protons from the 520 MeV cyclotron producing a myriad of radioactive and stable nuclei. The produced nuclei then diffuse out of the target and are ionized; the specific ion of interest is separated by mass and delivered as a low energy ion beam into the low-energy beam transport section (LEBT).

3.2.2 Beam Transport and acceleration

In the LEBT, the beam is pre-bunched and transported through a switchyard to either the low-energy experimental area or an eight meter long radio frequency quadrupole (RFQ), to accelerate the beam of mass number A up to a fixed energy of 150A keV while also providing transverse focussing. The following section, the medium-energy beam transport (MEBT) section chops and strips the beam to the final charge state to mass number ratio ranging from $1/7 \leq q/A \leq 1/3$. The beam is then rebunched and transported into the drift tube linac (DTL), which provides final acceleration to experiments in the ISAC I hall up to an energy of 1.8A MeV via a series of successively larger copper vacuum tanks within the skin of which the RF field oscillates back and forth against the phase of the central anode. The final stage before arriving at the experiment is the high-energy beam transport (HEBT) section in which several quadrupoles and rebunchers maintain the time structure and focus the beam.

For high-energy experiments in the ISAC II hall the DTL beam is deflected along an S-bend transfer line to the ISAC-II super conducting linac (SC-linac) for acceleration above the Coulomb barrier to a maximum energy ranging from 6.5A MeV to 16.5A MeV depending on the q/A value.

3.3 TUDA

The TUDA chamber shown in Figure 3.2 comprises two cylindrical sections used to house the detectors on either side of the target chamber. Detectors can be placed either upstream or downstream of the target in the cylindrical sections for detection of scattering events at both forward and backward scattering angles.

The end flange of the chamber is easily removed allowing the entire detector assembly to be withdrawn from the chamber along sliding rails. The target chamber houses the target ladder upon which a number of targets, collimators and diagnostics may be placed in the target position allowing for easy changes without breaking the vacuum.

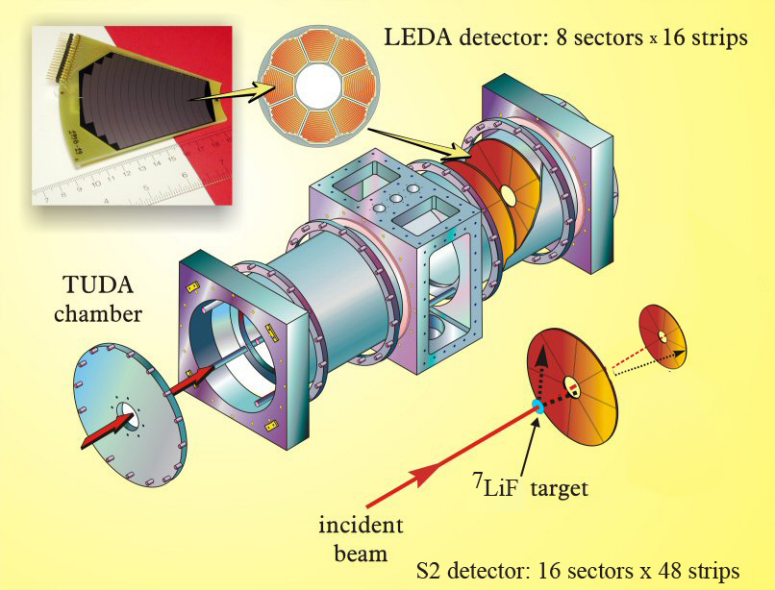

Figure 3.2: TUDA chamber as arranged in the experiment.

3.3.1 Detectors

LEDA

One of the two detectors used in the experiment was a single-sided silicon strip detector called a Louvain-Edinburgh Detector Array, or LEDA. This detector consisted of 8 separate sectors each with 16 elements (see the upper left corner of Figure 3.2 and Figure 3.3), and are p-n junction type reverse-biased strip detectors. The active area of the silicon is set in a transmission style printed circuit board (PCB) mount, containing the voltage tracks connecting the strips on the front side and the back side via ultrasonically-bonded wires to the output connector, which is of the unprotected insulation-displacement connector (IDC) type [31].

The pitch between strips for a sector can be found in Table 3.1 along with the active area for each strip. The energy resolution of individual detector elements for 5.486 MeV α particles is approximately 23 keV FWHM. A more detailed account of the LEDA detector can be found in Reference [31].

In this experiment, the LEDA detector was mounted 72 mm downstream from the

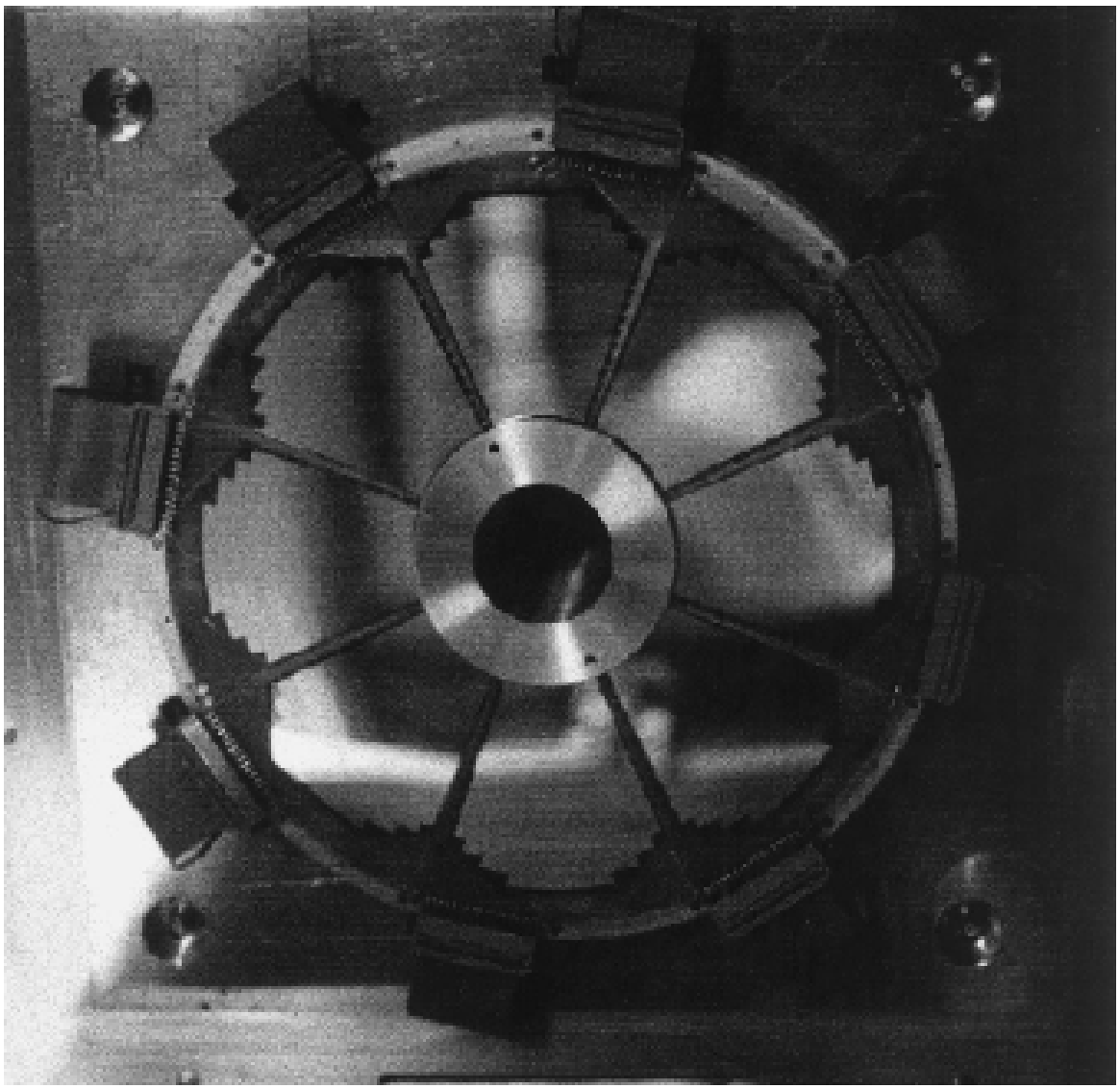

Figure 3.3: Image of the LEDA detector

Element No.	$\Delta\phi$ (deg)	Inner radius (cm)	Outer radius (cm)	Area (cm^2)
1	39.82	5.000	5.490	1.79
2	40.00	5.500	5.990	1.97
3	40.17	6.000	6.490	2.15
4	40.30	6.500	6.990	2.32
5	40.42	7.000	7.490	2.50
6	40.52	7.500	7.990	2.68
7	40.61	8.000	8.490	2.86
8	40.69	8.500	8.990	3.04
9	40.76	9.000	9.490	3.22
10	40.82	9.500	9.990	3.40
11	40.88	10.000	10.490	3.58
12	40.93	10.500	10.990	3.76
13	40.98	11.000	11.490	3.94
14	35.89	11.500	11.990	3.61
15	28.75	12.000	12.490	3.01
16	18.91	12.500	12.990	2.06

Table 3.1: Physical dimensions for each element of a LEDA sector. Each element is a strip along the sector with the given angular size, inner and outer radii, and physical area.

target ladder in the TUDA chamber and covered an angular range of 36 to 60 degrees in the laboratory frame.

S2

The second type of detector used in the experiment was an S2, a double sided silicon strip detector. The S2 detector consists of a single element that is divided into 16 sectors on the backside and 48 rings on the front and is a p-n junction type reverse-biased detector. Having an inner radius of 11.535 mm and an outer radius of 35.000 mm, the ring separation on the junction side is 100 μm. The separation between sectors on the ohmic side is 200 μm.

The S2 detector was mounted 130 mm downstream from the target ladder in the TUDA chamber and covered an angular range of 5 to 15 degrees in the lab frame.

3.4 Experiment Setup

With the LEDA and S2 detectors mounted 72 mm and 130mm downstream from the target ladder in the TUDA chamber the resulting laboratory angular coverage was 36 - 60 degrees for the LEDA and 5 - 15 degrees for the S2. The placement of the two detectors was chosen such that there would be a coincident detection between ^{7}Li nuclei in the S2 detector between lab angles of 5 - 10 degrees and ^{8}Li nuclei between 47 - 59 degrees in the LEDA.

The interference between elastic scattering and neutron transfer in the ^{7}Li(^{8}Li,^{7}Li)^{8}Li reaction produces characteristic oscillations in the differential cross section as a function of the scattering angle. From the analysis of the differential cross section the ANC for the valence neutron in ^{8}Li can be determined.

The target used was ^{7}LiF on a carbon backing. The target and backing thickness were 25 μg/cm^2, and 10 μg/cm^2 respectively. A ^{7}LiF target was chosen due to the compound being stable in air. Although a pure ^{7}Li target would have been optimal, it would have required special handling to prevent oxidation.

Prior to the radioactive beam being delivered to the TUDA chamber, the beam line was tuned with a stable $^{16}O^{4+}$ beam. Mounted on the target ladder within the TUDA chamber were 10 mm, 2 mm, and 1 mm collimators to aid during beam tuning. At the back of the TUDA chamber a Faraday cup (FCup) was mounted to read the beam current. Following beam tuning with the stable beam the radioactive $^{8}Li^{2+}$ beam was sent through with a

reading on the FCup at the back of the TUDA chamber of 5-7 pA. In order to measure the total flux of beam particles to be used for normalization purposes a channeltron electron multiplier was also placed in the TUDA chamber.

3.5 Instrumentation, data acquisition and detector calibration

The LEDA and the S2 detectors were instrumented via IDC cabling to preamplifier units which sat directly behind the detectors in the TUDA chamber. An external refrigeration cooling system using a mixture of 50% ethanol and 50% water circulated coolant throughout a network of hoses and copper tubes attached to the PCB to prevent overheating of the preamplifiers due to them being confined within a vacuum.

Figure 3.4 shows a schematic display of the electronics used in the data acquisition for the TUDA chamber. The output from the preamplifiers, along with other I/O connections such as pulser inputs, and preamp power were routed via coaxial cable connections on the rear flange. The signals then proceeded into a copper shielded electronics shack which houses the instrumentation and data acquisition systems. The copper shielding used in the electronics shack effectively forms a Faraday cage, reducing background noise which may interfere with the low voltage signals and sensitive instrumentation. A separate clean ground is also used within the electronics shack to further reduce background interference.

The data acquisition electronics is based around VME using VME ADCs (Silena 9418 analog to digital converters), TDCs (CAEN V767 time to digital converters) and scalers (CAEN V560). There is also a custom module for overall control of the data acquisition system which was designed and built at the Daresbury laboratory. Data readout is via the VME bus. The system consists of 512 ADC and TDC channels with 32 scaler channels which are housed in two VME crates linked by a SBS VME $\rightarrow$ VME interconnect. This link makes the two VME crates appear as one as far as access from the VME control CPU is concerned. During this experiment the system was set to trigger on a coincidence between the RF of the beam acceleration system and a signal in either Si detector.

The Silena 9418 is a single width VME module with a high resolution analog to digital converter, excellent integral and differential linearity, fast conversion time and programmable features. The structure of the 9418 is that of a multi-stretcher configuration connected to a high speed conversion module allowing the storing of up to 32 simultaneous pulses that can

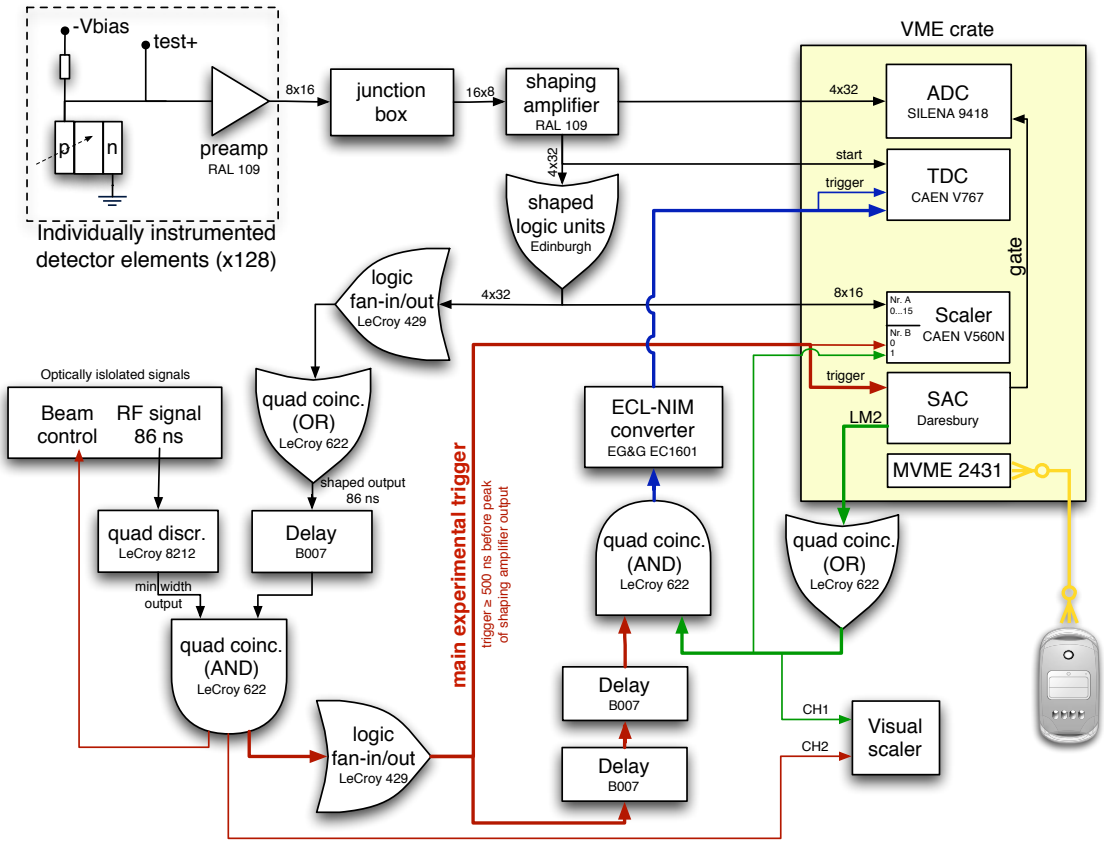

Figure 3.4: Schematic setup of the electronics for the TUDA chamber.

be converted in a fast sequence. The conversion section and the linear gate stretcher are both separated PCB modules, "Piggy - Back" plugged on the multilayer VME motherboard. The resolution, with a conversion time of 10 μs for all channels, is obtained using a fast 12 bit ADC. A sliding scale compensation technique has been implemented in order to improve the differential linearity. Major functions like rise time protection and low level threshold are software programmable with respective resolutions of 4 and 8 bits. Rise time protection can be monitored externally and a full functionality test of the board can be performed.

The CAEN V767 is a one-unit wide VME 6U module that houses 128 independent time to digital conversion channels. The unit houses four TDC chips, developed by the CERN/ECPMIC Division. The TDC is a General Purpose time-to-digital converter, with 32 channels per chip. The integrated circuit is developed as a full custom device in complementary metal oxide semiconductor (CMOS) 0.7 μm technology, and allows "COMMON START" operation with a typical bin size of 0.8 ns. All channels can be enabled for the detection of rising and/or falling edges and for each channel there is a digital adjust for the zero-ing of any offsets and pedestals.

The data acquisition processor is a Motorola MVME2431 single width VME board module. This contains a PowerPC 750 microprocessor running at 350 MHz with 32 Mbyte of SDRAM, an on-board fast Ethernet controller and a 64 bit VME interface. The LynxOS real time software kernel is used (release 3.1.0). LynxOS is a UNIX-like system enhanced for real-time use. The OS is initially booted from a Sun workstation but once the data acquisition software components are loaded and running no further access to the Sun is required unless additional software components are required by manual intervention.

All components of the data acquisition software system are controlled and monitored via MIDAS (Multi Instance Data Acquisition System). Remote connections from outside the electronics shack enabled starting and stopping of data acquisition without needing to enter the electronics shack. Data was stored in separate data files, each approximately 200 megabytes in size, corresponding to roughly 2 hours of beam time.

An energy calibration run was performed before the experiment commenced and immediately following it using a triple alpha source containing the isotopes Plutonium-239 (^{239}Pu), Americium-241 (^{241}Am), and Curium-244 (^{244}Cm), each of which have two alpha peaks at energies of 5.105 and 5.156 MeV, 5.443 and 5.486 MeV, and 5.763 and 5.805 MeV respectively. Pulser data obtained before the experiment were used to calibrate the TDCs for post experiment analysis.

It should be noted here that while the intention was to detect the low energy recoils in the LEDA detector in coincidence with the small scattering angle ejectiles detected in the S2 this was not the result. Possibly due to a power outage and reinitialization of the data acquisition system (DAQ) after initial calibration and setup, a software threshold in the discriminators or ADCs reverted to a higher default value, which prevented the DAQ from triggering on the low energy recoils required for coincidence. Unfortunately, due to presence of other coincidences between the S2 and LEDA detectors at similar energies, this oversight was not realized until the run was completed, during the data analysis phase. While not having coincident ^{7}Li to separate the desired ^{8}Li events from the large background at low angles due to elastic scattering from ^{19}F and ^{12}C created many unexpected difficulties, the data from the S2 detector were still reliable, albeit with larger errors and for a reduced angular range than if the coincident nuclei had been recorded. This will be further discussed in Chapter 5.

3.6 The ^{7}Li(^{8}Li,^{7}Li)^{8}Li reaction

The reaction that is the focus of this thesis is the ^{7}Li(^{8}Li,^{7}Li)^{8}Li reaction. The benefit of studying this reaction over previous direct reactions that have been studied for $S_{17}(0)$ analysis is apparent upon examination of Equation 2.91. The two ANC terms $C^{B}_{Aal_{B}j_{B}}$ and $C^{X}_{Yal_{X}j_{X}}$, as well as the single particle ANC terms $b_{Aal_{B}j_{B}}$ and $b_{Yal_{B}j_{B}}$, are identical for this reaction, thereby simplifying the expression and reducing the associated errors. As well, indirect measurements do not suffer from the large uncertainties due to extrapolation down to zero energy that direct measurements require.

3.6.1 Peripheral nature of the reaction

In order to obtain valence particle spectroscopic information from a transfer reaction the theoretical prediction for the reaction cross section is normalized to the experimental data, see Equation 2.96. This is provided that the theoretical calculation involved a bound state wavefunction normalized to unity.

The dependence of the cross section on the overall normalized bound state wavefunction has been tested in References [28] and [32]. Results have shown that the spectroscopic factor S in Equation 2.96 is not constant but largely model dependent. This is due to the fact that the cases tested refer to transfer reactions of a peripheral nature, where only

the tail of the overlap wavefunction between initial and final states contribute significantly to the transfer cross section. For a peripheral reaction the DWBA transfer matrix from Equation 2.98 expressed in the prior form for the lithium transfer reaction of this study can be expressed with the initial and final bound state wavefunctions replaced by the peripheral approximation from Equation 2.89:

$$T_{fi}^{PRIOR} = \left\langle b\frac{W(2\kappa r)}{r} \right| \left(V_{^7Li+n} + U_{^7Li+^7Li} - U_{^7Li+^8Li}\right) \left| b\frac{W(2\kappa r)}{r} \right\rangle . \tag{3.1}$$

Extracting the single particle ANCs, we are left with the model independent Whittaker function describing the initial and final states. The single particle ANC, b, will then simply be a factor multiplying the overlap of the initial and final states. From Equation 2.57 the relationship between the differential cross section and the transfer matrix will introduce a factor of b^4. This normalization of the theoretical differential cross section in Equation 2.96 results in

$$\frac{\frac{d\sigma}{d\Omega}^{\text{peripheral}}_{\text{expt}}}{\frac{\frac{d\sigma}{d\Omega}^{\text{peripheral}}_{\text{theory}}}{b^4}} = Sb^4 = \text{Constant}, \tag{3.2}$$

for a peripheral reaction.

By maintaining a constant spectroscopic amplitude for all calculations and varying the depth of the binding potential to reproduce the binding energy, the theoretical differential cross section for the transfer reaction should only vary by the normalization factor b^4. The calculated values for $(\frac{d\sigma}{d\Omega})_{\text{theory}}$ for the lithium transfer reaction using different radii and diffuseness for the binding potential normalized to b^4 are displayed in Figure 3.5

From the plot shown in Figure 3.5 the elastic transfer reaction ^{7}Li(^{8}Li,^{7}Li)^{8}Li shows a peripheral behaviour. There is a small contribution from the nuclear interior at higher scattering angles as can be seen by the spreading out of the calculated differential cross sections. As the experimental data from this experiment does not exceed 110° in the center of mass frame this will not be an issue and the reaction can be considered peripheral for the purpose of DWBA analysis.

Set #	r	a	V	$\chi^2(\times 10^{-3})$	$b^2_{p_{3/2}}$(fm)
1	2.20	0.65	52.56	13.2	0.531
2	2.25	0.65	50.46	9.76	0.543
3	2.30	0.65	49.15	8.04	0.554
4	2.35	0.65	47.23	6.28	0.567
5	2.40	0.65	46.09	5.63	0.579
6	2.45	0.65	44.30	5.43	0.591
7	2.50	0.65	43.19	5.79	0.603
8	2.55	0.65	41.62	7.05	0.616
9	2.60	0.65	40.14	9.13	0.630
10	2.65	0.65	38.73	12.0	0.643
11	2.70	0.65	37.83	14.3	0.658
12	2.50	0.50	43.96	13.1	0.482
13	2.50	0.55	43.79	7.42	0.518
14	2.50	0.60	43.53	5.00	0.560
15	2.50	0.70	42.80	9.61	0.651
16	2.50	0.75	42.35	16.2	0.706
17	2.50	0.80	41.85	25.4	0.762

Table 3.2: Variation in the parametrization of potential 2 in Table 4.1 with corresponding single particle ANC values. Included are the corresponding χ^2 values determined by comparison of the computed bound state wavefunction to the VMC wavefunction of R. Wiringa [33] which may be seen in Figure 6.1.

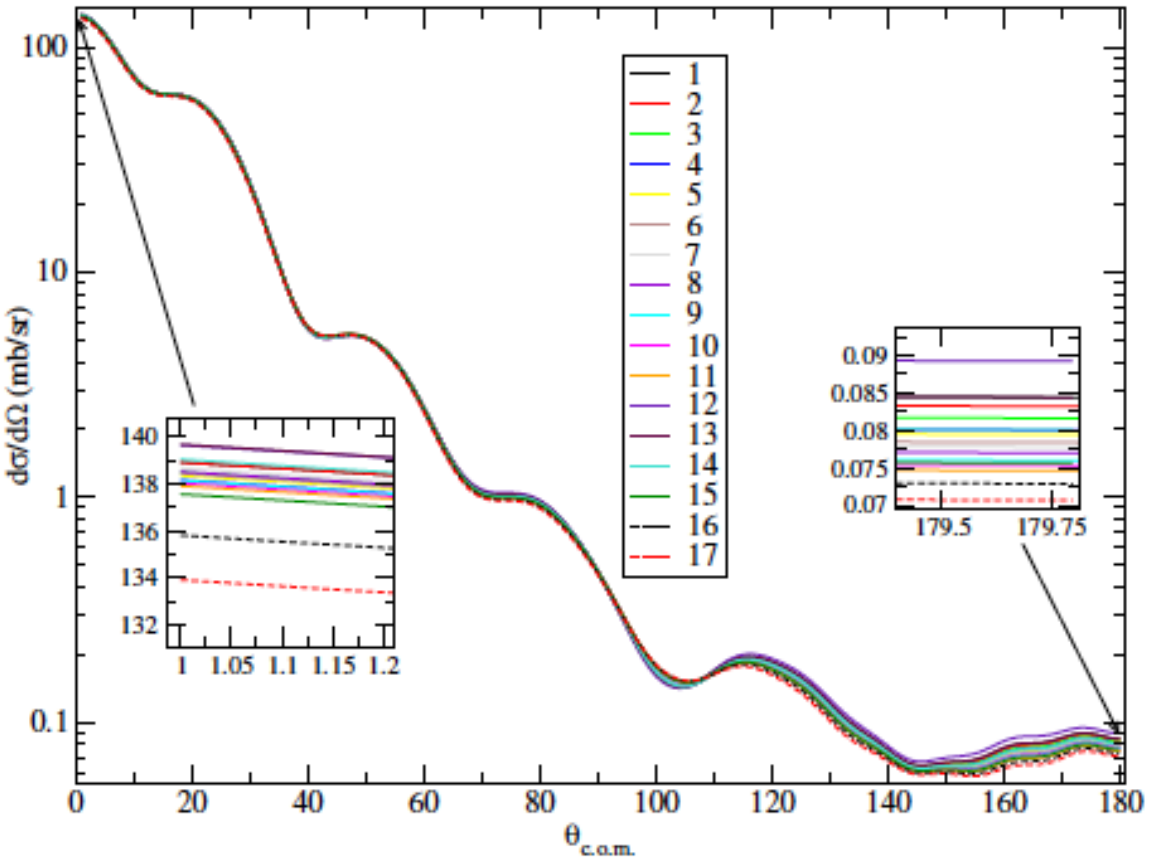

Figure 3.5: DWBA calculations for the ^{7}Li(^{8}Li,^{7}Li)^{8}Li reaction at 13 MeV normalized to b^4. Only the transfer cross section is shown with data sets labeled by the corresponding binding potential parametrization of Table 3.2. Included are enlargements of two sections at $\theta = 0°$ and $\theta = 180°$ in order to assess the spread at each extreme. Figure from Reference [34]

Chapter 4

Analysis Software

Modern day nuclear physics experiments require sophisticated software for acquiring, sorting, calibrating, reducing and analyzing the data. Many programs are written specifically to perform a single calculation or task and are generally maintained as needed by a single user or a small user group. There also exists a large group of software programs that are developed and widely used across the field. Two of these widely used programs that are used in this thesis will be discussed in this chapter. The first software program is ROOT, which is used for calibration and sorting of data collected from the experiment. The second piece of software is FRESCO and the associated SFRESCO codes used for performing DWBA calculations and fitting theoretical cross sections to the data. Before discussing those topics the data acquisition system used will be briefly discussed.

4.1 MIDAS

The TUDA data acquisition system MIDAS is built from a package of software components and techniques originally developed for Eurogam but is now considerably extended and used for a wide range of applications. The applications of MIDAS currently include Eurogam, Euroball, Exogam, Megha, Charissa, GREAT, TIARA and others.

The Midas GUI is based on a script language known as Tcl/Tk. Although Sun originally sponsored this development, in recent years the package is available on a wide range of hardware platforms including Sun Solaris and Microsoft Windows. Tcl/Tk has a Motif-like graphical user interface which makes it fully compatible with the CDE window manager used on Sun Solaris systems. All documentation and files for MIDAS can be found at

http://npg.dl.ac.uk/MIDAS/index.html.

4.2 ROOT

ROOT was developed in the context of the NA49 experiment at CERN to handle the large amount of data produced by the experiment. Around 10 terabytes of data were generated per run which provided the ideal environment for developers René Brun and Fons Rademakers to develop and test their conceived object oriented design for next generation data analysis. ROOT was to replace aging FORTRAN libraries that had reached their limits and could not scale up to the challenges offered by the Large Hadron Collider due to amounts of data a few orders of magnitude larger than anything seen before [35].

The experiment of this thesis by no means had the large amount of data that ROOT was originally designed to handle, as data files are on the order of 200 megabytes per run; however, ROOT still provided an excellent environment for data calibration, sorting events, and fitting histograms.

ROOT is not a standalone program, it is a data analysis framework. For the command line and script processor, ROOT uses CINT as its C++ interpreter. Along with ROOT, a software program called tudaROOT written by Jonty Pearson was used to convert the data files from the experiment, originally in the MIDAS format, into ROOT data files. For more details concerning ROOT or for source code please refer to Reference [35].

4.2.1 Framework

Working inside an existing framework eliminates the need to develop tools and code for basic routines and algorithms. An apt comparison to programming inside a framework is building a house in a city. In a city there is already infrastructure in place for plumbing, electricity, and telephone; these are not needed to be developed, merely connected. Building a house in the country where none of this infrastructure exists and needs to be developed along with the house is similar to programming outside a framework, where all the infrastructure needs to be developed along with the program.

Another benefit of working within a framework is that the routines and algorithms in the framework have already been tested and found accurate and reliable. A drawback of a framework is that you are constrained to work within its boundaries, which in the case of the ROOT framework did not pose a problem for the analysis for the experiment of this

thesis. The main uses of the ROOT framework here are reduction, calibration and sorting of data, as well as collecting events into histograms and the fitting of the histograms. Most of these applications will be discussed in Chapter 5. Before getting to that, I will briefly touch on ROOT's handling of histograms.

4.2.2 Histograms

Histograms are a basic component of data analysis in nuclear physics experiments. They provide a simple method of displaying a large number of events, as well as a visual means of reducing data by implementing cuts via either kinematics or timing conditions. The histogram class in the ROOT framework supports one, two, and three dimensional histograms with either one byte, short, integer, float, or double values per channel. All histograms support fixed or variable bin sizes.

Filling a histogram in the ROOT framework is performed by a simple "FILL" command with a required call value based on the data being collected. The histogram class contains a "Fill" method which computes the bin number corresponding to the given arguments and increments the bin. Several other methods exist that perform the functions of adding, dividing and multiplying histograms together or by a constant value. The ability to easily create and fill histograms is only one of the many benefits granted by working in the ROOT framework.

4.2.3 Fitting Histograms

The advantage of using the ROOT framework to fit histograms is evident when fitting multiple histograms. By using an input file to define predetermined limits, fit results can quickly be obtained and compared for various kinematic or timing cuts. The framework also supports fitting multiple peaks in a single range and background estimates.

The minimization package used by ROOT, MINUIT[1], originally written in FORTRAN by Fred James, was converted to a C++ class by René Brun. The "MINUIT" package acts on a multi parameter FORTRAN function to which one must give the generic name "FCN". The function "Fit" defines the MINUIT fitting procedure as being being either a chi-squared or binned likelihood minimization. It is the task of MINUIT to find the values of the parameters which give the best fit.

[1]For more information on the MINUIT package see Appendix C

4.3 FRESCO

The computer code FRESCO [36], developed by Ian J. Thompson, incorporates many approaches to various aspects of reaction theory. The code is a comprehensive, state-of-the-art program for modeling nuclear reactions by performing calculations for coupled channels that have a finite-range transfer interaction among any number of mass partitions, and any number of nuclear excitations in each partition. A public version of the code along with detailed documentation can be downloaded from the website `www.fresco.org.uk`.

Following the theory laid out in chapter 2, FRESCO calculates and stores the kernels of the non-local interactions of the form of Equation 2.72, and then solves the coupled-channel set for each iteration of Equation 2.69. The stored kernels are then used to integrate the wave function (2.68) to generate the source terms for the next iteration.

The projectile or the target of any partition can also have local couplings for the rotational or single-particle excitations generated; as well, local form factors for zero-range or local energy approximations may also be used. These various local interactions may also be included iteratively resulting in a multistep DWBA. Alternatively the first few coupled channels may be grouped together and solved by exact coupled-channels methods.

Input files are used to define and set up the parameters, partitions, potentials, and overlaps used for a reaction calculation. Appendix A outlines the various sections of a FRESCO input file using an elastic scattering example and a transfer reaction example, and gives a detailed listing of the parameters.

4.3.1 ^{7}Li(^{8}Li,^{7}Li)^{8}Li

For a transfer reaction the entrance and exit channels need to be explicitly stated separately for FRESCO. In the case of the ^{7}Li(^{8}Li,^{7}Li)^{8}Li the entrance and exit channels are identical. This has the advantage of only needing a single optical potential for both the entrance and exit channels; as well, only a single binding potential is required. The initial values used for the potentials are shown in Table 4.1.

The state of the second partition is defined only by the optical potential index and by the key “copyp=-1”. The “copyp” key tells FRESCO that this level is an exchange copy of the same numbered level in the previous partition, that is, a copy with projectile and target nuclei exchanged.

kp	Interaction	V	V_{SO}	r_V	a_V	W_V	r_W	a_W	r_C	Ref.
1	$^7Li + ^8Li$	175		0.64	0.8	16.9	1.09	0.8	1.3	[34]
2	$(n + ^7Li)_{p_{3/2}}$	43.19	0.0	2.5	0.65				2.5	[38]
4	$(n + ^7Li)_{p_{1/2}}$	42.14	4.9	2.391	0.520				2.391	[39]
10	$^7Li + ^7Li$	4.66		0.173	1.617	5.60	1.589	0.397	1.3	[40]

Table 4.1: Interaction potentials used for FRESCO calculation of ^{7}Li(^{8}Li,^{7}Li)^{8}Li reaction at 11 MeV. The "kp" value corresponds to the index of the potential as it appears in the input file of Figure B.3. Real and imaginary depths, V and W, are expressed in MeV. Radii and diffusenesses are in fm. The radii of the optical potentials are reduced, and full radii follow the convention $R_i = r_i(A_t^{1/3}+A_p^{1/3})$ where i is either V or W. Potential 1 is the optical potential for the interaction between the ^{7}Li + ^{8}Li nuclei. Potentials 2 and 4 are binding potentials for the $p_{3/2}$ and $p_{1/2}$ orbitals respectively, and potential 10 is the core-core interaction.

With no optical potential for the ^{8}Li+^{7}Li reaction at 11 MeV to be found in the literature, the initial optical potential used is taken from Reference [34]. The parameters of this potential are derived from systematic studies of ^{8}Li elastic scattering data at laboratory energies from 13 to 20 MeV with targets in the mass range of 1 to 58 amu [41]. Separate binding potentials are needed for both the $p_{3/2}$ and $p_{1/2}$ states for the valence neutron in ^{8}Li. The $p_{3/2}$ binding potential is taken from Reference [38], while the $p_{1/2}$ binding potential is taken from Reference [39]. The core-core potential is a volume-dominated optical potential for the interaction between ^{7}Li and ^{7}Li taken from a study at laboratory energies from 5 to 40 MeV [40].

The overlap and coupling is also simplified due to the symmetry of the reaction and only requires the overlap for the valence neutron on ^{7}Li. The spectroscopic amplitude, however, must appear twice, once for each vertex in the reaction. The initial values for the $p_{3/2}$ and $p_{1/2}$ spectroscopic amplitudes are set to the values from Reference [33]. During the fitting process the $p_{3/2}$ spectroscopic amplitude is allowed to vary while the $p_{1/2}$ amplitude remains fixed at the initial value. Due to the requirement of each amplitude to appear in the FRESCO input file twice, the actual value of the spectroscopic factor for each orbital is given by the product of the amplitudes for the entrance and exit channels [42]. With the reduced amount of usable data collected during the experiment the number of degrees of freedom to fit for both spectroscopic amplitudes would have significantly reduced the quality of or even limited the possibility of obtaining a convergent fit. Lacking the angular

coverage to separately determine both the $p_{1/2}$ and $p_{3/2}$ spectroscopic amplitudes the $p_{1/2}$ spectroscopic amplitude is held fixed. This is discussed further in Section 5.3

This input file provides a starting place for fitting theoretical calculations to the data. Initial fits are performed to adjust the entrance and exit optical potential by fixing the spectroscopic amplitudes at currently accepted values and allowing only the optical potential parameters to vary. Once a χ^2 minimization is reached for the optical potential, the resulting values are substituted in as starting values for a new minimization where the optical potential for the entrance and exit channels as well as the $p_{3/2}$ spectroscopic amplitude are fit. Full details of the analysis and results from the SFRESCO fit can be found in section 5.3.

4.4 SFRESCO

A first calculation of the cross section using FRESCO will often produce results that differ from experimental data. Whether the reaction model is too simplified or the input parameters are not accurate enough the FRESCO calculation may be improved upon by using the program SFRESCO, the Search version of FRESCO. SFRESCO uses the MINUIT routines to search for a χ^2 minimum when comparing the outputs of FRESCO with datasets.

Along with a standard input file as described in section 4.3, an input file for SFRESCO and a SFRESCO script are required to perform a SFRESCO minimization. The input file specifies the FRESCO input and output files, the number and types of the search variable, and the experimental data sets to be compared against. The script is a simple method of entering commands to SFRESCO to perform the fit as desired; alternatively the commands may be entered manually via the command line. As a simple example of a SFRESCO minimization, an elastic scattering example of a proton scattering off of ^{112}Cd is provided below.

4.4.1 p + ^{112}Cd elastic scattering

The following example is from the FRESCO User's Guide which may be found at the website `www.fresco.org.uk`. A basic input file (Figure B.4) for FRESCO is required that defines the energy, partitions, states, and the potentials needed for the calculation. The potential is defined here using the "type" variable which indicates the shape of the potential. Type 0 is for Coulomb potentials, type 1 for volume central potentials, type 2 for surface

central potentials, type 3 for spin-orbit potentials for the projectile, and type 4 for spin-orbit potentials for the target.

The SFRESCO input file shown in Figure B.6 begins with the filename of the FRESCO input file and the desired output filename. The following line indicates the number of parameters to be fit followed by the number of experimental datasets. The header "&variable" lists the parameters to vary during the minimization. In this example all the parameters are variables of the interaction potential and are of the type "kind=1". The individual variables are identified by the values of: "kp", the index of the potential, "pline", the line within the potential, and "col", the column number for the given line. The optional "potential" value is used to override the default values given in the FRESCO input file. A final "step" value sets the initial magnitude for trial changes. Other optional values not included are minimum and maximum values for the parameter, "valmin" and "valmax", respectively.

Type	**Description**
0	Angular distribution for fixed energy
1	Excitation and angular cross-section double distributions
2	Excitation cross section for fixed angle
3	Excitation function for the total, reaction, fusion, or inelastic cross section
4	Excitation phase shift for fixed partial wave
5	Desired factor for bound-state search
6	Specific experimental constraint on some search parameter.

Table 4.2: SFRESCO data types

Experimental datasets are identified by their "type". A list of the different types available are summarized in Table 4.2. A data file may be used to input the dataset by entering a filename, or the data can be listed in the input file by replacing the filename with "data" as is done in this example. A value may be supplied for the number of data points to read in; if a value is not supplied all the listed data are used. The value of "iscale" indicates the units of the data and is -1 for relative data, 0 for absolute data in units of fm^2/sr, 1 for b/sr, 2 for mb/sr, and 3 for μb/sr. To indicate the desired format for the output, "idir" is set to -1 for cross section data given as astrophysical S factors, 0 for data given in absolute units, and 1 as a ratio to Rutherford. The reference frame for which the dataset is given is indicated by the value of the input parameter "lab" and is "T" or "F" for laboratory angles and cross sections. Finally, if "abserr" is true, the third column of the dataset is treated as

absolute errors.

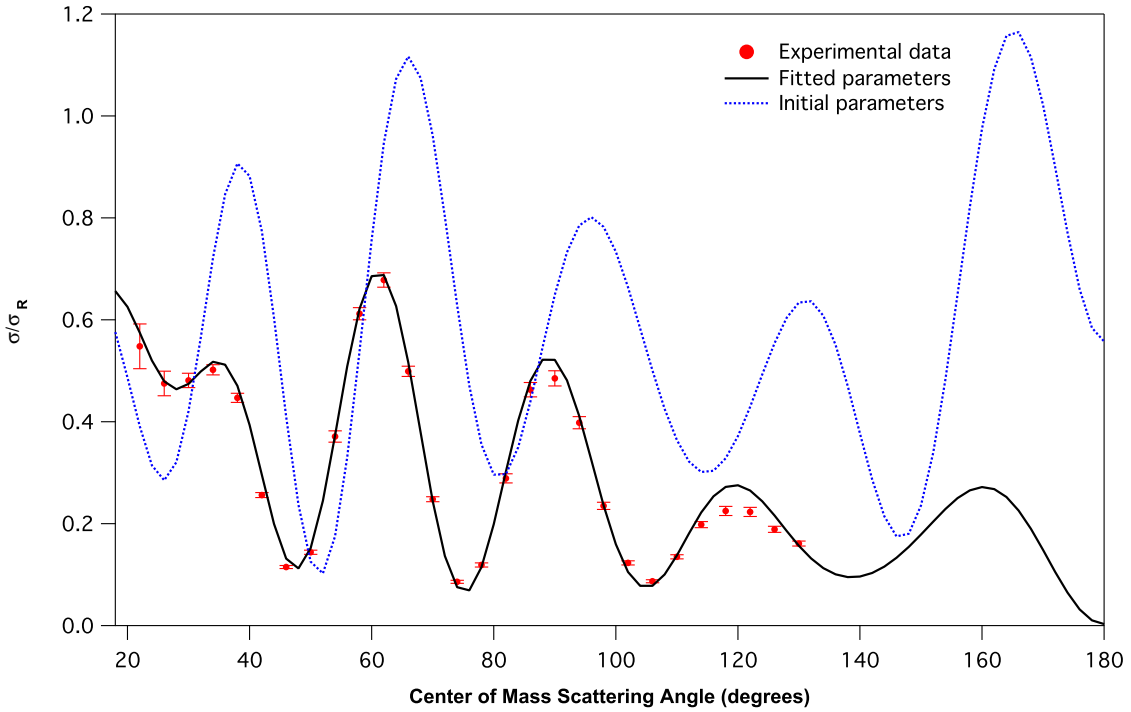

Figure 4.1: Data and calculations of proton scattering on ^{112}Cd at 27.90 MeV with initial and fitted potential parameters.

SFRESCO may be run using an input script, as shown in Figure B.5, or by directly interacting with the command line. When multiple minimizations are required or the run time is long a script proves useful. A minimum set of commands is required and includes: the SFRESCO input filename, “min”, “migrad”, “end”, and “plot”. The “min” command calls MINUIT interactively using the starting values and variables defined in the SFRESCO input file. This is followed by “migrad” which within MINUIT performs a MIGRAD[2] search. The “end” command returns to SFRESCO from MINUIT, the “plot” command is not required for a minimization; its function is to produce a file with the data and theory curves for display with the program xmgr, a 2d plotting tool. Many more commands are available and a full list may be found in appendix A.

[2]For more information on MINUIT and the MIGRAD minimizer please refer to Appendix C

Parameter	Initial Value	Final Value
V	45.5 MeV	52.18 MeV
W	1.5 MeV	2.90 MeV
WD	4.5 MeV	8.18 MeV
r_0	1.17 fm	1.18 fm

Table 4.3: SFRESCO fit results for p + ^{112}Cd elastic scattering from input files displayed in Figures B.4 and B.6

The results of the SFRESCO minimization from the input of Figures B.4 and B.6 are displayed in Figure 4.1. The initial FRESCO calculation is shown as well as the final FRESCO calculation using the final values for the parameters that were varied. The fitted parameters are displayed in Table 4.3.

4.4.2 Minuit Error

From SFRESCO, the solution of a minimization problem using Minuit is itself straightforward. The calculation or interpretation of the resulting parameter uncertainties is considerably more complicated. Specific complications for this fit arise from multi-parameter error definition and interpretation. With more than one free parameter problems may arise in interpreting errors from Minuit. The output from Minuit gives an error matrix from which the individual parameter error values are calculated.

The error matrix, also called the covariance matrix, is the inverse of the matrix of second derivatives. The diagonal elements of the error matrix are the variances (squares of the standard deviations) of the corresponding parameters, and the off-diagonal elements indicate the degree of correlation, positive or negative, between the corresponding pairs of parameters [43]. Calculations of the error in this fashion take into account effects of correlations among parameters.

In order to ensure accurate error values from the fitting procedure an extra call was made to Minuit instructing it to calculate the Hessian matrix. The call calculates the full matrix of second derivatives of the function with respect to the currently variable parameters, and inverts it, printing out the resulting error matrix.

Chapter 5

Data Analysis

Progressing from a collection of signals in various ADCs, and TDCs to a final result requires many different stages of data processing and analysis. The next two chapters discuss details of the data reduction and analysis, as well as the fitting of theory to the results of the experiment.

5.1 Detector Calibration

The first step before performing data reduction is to perform energy and time calibrations for the detectors and associated electronics. This ensures that all detected events are properly adjusted for variations between the separate elements. Specific problems with detector readouts may also need to be identified and addressed. Other steps involving the physical properties of the detectors ranging from actual position relative to the beam spot and amount of active area present in an azimuthal range need to be calculated and corrected. Once all this initial calibration is complete, the data extraction and subsequent analysis can commence. Applying gates on the energy and time spectra to select areas of interest can reduce background and aid in identifying loci, eventually leading to a final reduction of the data for fitting. After removing as much background as possible and applying appropriate adjustments and corrections, the theory can be fit to data to obtain the final results.

5.1.1 Energy and Time calibration

As was discussed in Chapter 3, the detectors were calibrated before the experiment and immediately following it using a triple–α source. The α peaks are fit with gaussian functions, resulting in a centroid channel number for each energy peak in each ADC. These centroid channel numbers are then fit with a linear function to reproduce the known energies of the α's corrected for energy loss from SRIM calculations [44]. The energy calibration for each ADC channel consists of an offset and a gain variable.

The TDCs were calibrated using a pulser prior to the commencement of the run. The pulse generator was connected to all TDC channels. The result is a readout where all channels are triggered with a simultaneous event. From this pulser data the individual TDC channels were calibrated by applying an offset value to raw data during analysis. The calibrated data from the TDC shows a uniform time from the pulser whereas before the calibration slight variations on the timing were present due to variations in the individual electronics of each channel.

5.1.2 Beam Offset

The presence of ^{19}F in the target resulted in elastic scattering which could be analyzed for detector calibration. Comparing the absolute numbers of scattered ^{8}Li among the sectors detected in the S2 detector between laboratory angles of 5 to 15 degrees an asymmetry shown in Figure 5.1, is observed. This asymmetry arises from a slight displacement of the beam spot from the center of the detectors.

The calculated angular range for the recoil and ejectile from the ^{7}Li(^{8}Li,^{7}Li)^{8}Li reaction can be seen in Table 5.1. The LEDA detector covers a range from 36 to 60 degrees in the laboratory frame. For a coincidence event in this range one particle is detected at the lower range of accepted angles by the LEDA detector, while the other event is detected near the middle of the detector's range. This fact aided in the confirmation of the beam offset. Due to the beam offset the angular coverage of each sector in the detector is shifted. Sectors that are closer to the beam axis have an angular range that is shifted down, while sectors on the opposite side of the detector where the beam axis is shifted away from the sector result in an upward shift in the angular range. Comparing these coincidence events an asymmetry is also observed. Although the effect is much smaller in the LEDA than in the S2 due to the differences between the angular size of each detector, this asymmetry observed in both

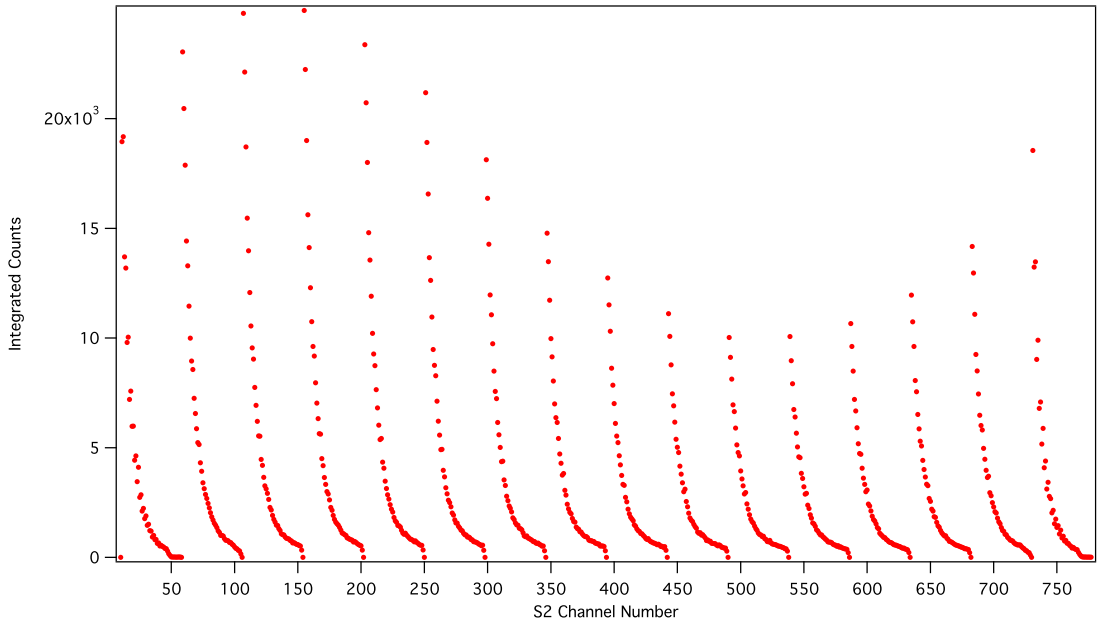

Figure 5.1: Elastic scattering of ^{8}Li from ^{19}F. The x-axis represents the S2 channel number starting at x=0 for sector 0 ring 0 and incrementing by ring (i.e. x=1 represents sector 0 ring 1, x=2 represents sector 0 ring 2). Each sector consists of 48 rings and there are a total of 16 sectors.

detectors indicates a beam offset from the detector centers.

Ejectile angle (°)	Recoil angle (°)
35	49.52
38	47.09
41	44.58
44	42.02
47	39.41
50	36.77
53	34.09
56	31.40
59	28.68

Table 5.1: Kinematically calculated range of the recoil and ejectile angles in degrees from the ^{7}Li(^{8}Li,^{7}Li)^{8}Li reaction. The LEDA detector covers a range from 36 to 60 degrees.

Using the data from ^{19}F elastically scattered events a minimization was performed to determine the offset of each detector from the beam axis. By varying the offset values and thus the correlated scattering angle the asymmetry is minimized and the beam offset is determined.

	S2 offset	
Run Group	x (±0.001) (cm)	y (±0.001) (cm)
1	0.061	0.144
2	0.058	0.143
3	0.082	0.119
4	0.023	0.117

Table 5.2: Calculated beam offset based on asymmetry of elastically scattered ^{19}F events

On account of the superior angular resolution due to segmentation in the S2 detector as well as significantly higher event counts, the offset for the S2 detector introduces a larger effect than the offset for the LEDA detector. Due to the larger spacing of the rings the effect of the offset was found to be negligible in the LEDA detector. The offset values from the minimization from the S2 data are displayed in Table 5.1.2 in units of centimeters. The multiple entries for the offset correspond to groupings of run files from the experiment. Each significant change to the offset is correlated with a logged change in the beam tune during

the experiment. Since the effect of the offset on the data from the LEDA detector was negligible no offset was used for the data from the LEDA.

5.1.3 Detector Geometry

Corrections for the amount of active area present in a given angular range due to inactive areas of the detectors, as well as the effects of the offset between the beam spot and the detector centers, are accounted for via Monte Carlo simulations. A program was written to evaluate the fraction of events striking the active area of each detector segment as a function of laboratory angle.

The Monte Carlo program generates a large number of events with a random scattering angle within a preset range. Each event is then compared to the detector geometry and it is determined whether it impacted a region of active area on the detector and is thus considered a good hit, or impacted a dead region and is counted as a miss. The detector efficiency for a given angular range is calculated as the number of good hits in that angular range divided by the total number of events simulated.

For the S2 detector the width of each bin is set to 1.0 degree and a total of 5×10^7 events are generated in each bin. The LEDA detector was simulated with bin sizes ranging from 1.6° to 2.5° corresponding to the distinct rings in the detector. As well as the primary event the LEDA also required the simulation of a second event on the opposite side of the detector within a range corresponding to the coincident recoil. The number of primary events generated for the LEDA detector was 10^7 with each primary generating a single coincident recoil event.

The resulting geometric coverage of each 1° (laboratory angle) bin in the S2 detector ranged from 12% for bins on the edge of the detector to 78%. The decision to use 1° bin sizing in the S2 detector rather then the natural bin size from the individual rings of the detector was due to the effect of the offset. Due to the small size of the rings the offset created large shifts in the scattering angle between opposite sides of a single ring. By using a much larger bin size than the physical size of a ring, binning errors introduced from the offset are reduced. This choice to use large bin sizes in the S2 detector was also due to the lack of coincident recoils and resulting difficulty separating the data from background events. The high statistics in a given bin provided a reliable means for precise data reduction through the multiple peak fitting procedure discussed in section 5.2.3.

The geometric efficiency of the S2 as a function of scattering angle varies over a large

range mostly due to the exclusion of sectors 0 and 15 due to the crosstalk effect which will be discussed in section 5.1.5. With the exclusion of two sectors and the effects of the offset, the bins representing data from the edge of the detector had very little active area for detection and thus small percentages of geometric coverage.

The LEDA detector, as previously discussed, did not require using an offset as the S2 detector did. Each bin from the LEDA detector therefore reflected the data collected in a complete ring in the detector. The resulting geometric coverage of each bin in the LEDA detector ranged from 74% to 85%. The angular size of the bins in the LEDA detector varied slightly due to the geometry of the detector and ranged from 1.6° to 2.5° (laboratory angle).

5.1.4 Split Events

The S2 detector is a type of double sided silicon detector (DSSD), and therefore requires an energy constraint between the rings and the sectors to eliminate unequal energy detection. Ions implanted in a DSSD should produce equal peak heights on both sides of the detector resulting in an equal energy being recorded for both sides. If an unequal energy is detected between the two sides the event is generally considered unreliable and is discarded. Another issue encountered with the S2 detector was an energy splitting or sharing between adjacent channels.

Analysis of a full readout of all ADCs for the S2 that recorded a hit during an event led to the following observations. With three ADCs recording a hit during a readout, it was found that the sum of two events occurring in adjacent sectors or rings resulted in the same energy recorded by the third ADC, which corresponds to either a ring or sector hit respectively. Another case that required special attention is when two distinct events occurred in the S2 during the same readout. For this situation recorded signals are compared and if the individual events are distinguishable, they are paired up accordingly and processed as two distinct events.

The initial results of placing a gate on the energies between the sectors and rings of the S2 was a large reduction of the background. When corrections for split energy events and double events are included, the effects are a further reduction of the background and a repositioning of a number of lower energy events to higher energies. The total number of events processed within the range of 9 MeV to 12 MeV without any cuts or gates is shown in Table 5.3. The number of excluded events due to the energy gate is counted and is found to be slightly less than the difference between the first two entries. This discrepancy is due

Range	Number of Events
9 - 12 MeV	7.90×10^7
Equal Energy Gate	6.27×10^7
Omitted	1.55×10^7
Equal Energy + corrections	6.61×10^7

Table 5.3: Total number of events processed in the S2 detector prior to and following the application of energy gates to the data. The final entry includes all events after equal energy gates and corrections to events discussed due to energy splitting between adjacent channels.

to a double counting effect in the un-gated range from split energy events. The final entry in Table 5.3 includes the corrections from the energy gate as well as from split energy events. It is slightly greater than the number of events processed with only the energy gate due to the inclusion of events that are excluded by the 9 to 12 MeV energy window due to energy splitting effects previously discussed.

Two dimensional histograms depicting the events detected in the S2 detector between 9 and 12 MeV are displayed in Figure 5.2. The top left panel represents the first entry in Table 5.3. The top right panel shows the events remaining after removing all events that did not have equal energies within 3% between the sectors and rings of the detector. In the bottom left panel the events omitted between the top two panels are displayed, and the final panel shows the events after the energy gate and corrections for split energy events are included.

5.1.5 S2 Crosstalk

During the first stages of sorting the collected data from the S2 detector a peculiarity was noticed in the two sectors located immediately adjacent to the pinout region, where signals emerge on the detector. These sectors (sector 0 and sector 15) show an oscillatory pattern overlaid on top of the expected $\frac{1}{\sin^4(\theta/2)}$ function for elastically scattered ^{8}Li events from a ^{19}F nucleus. The top panel of Figure 5.3 shows the elastically scattered events from the ^{19}F nuclei for sectors 0 and 15. The bottom panel depicts the expected and typical results for an elastic scattering spectrum which is observed in all other sectors.

The two sectors 0 and 15 are different from the other sectors since they are adjacent to the edge of the detector in terms of azimuthal angle and the tracks over the silicon wafer to

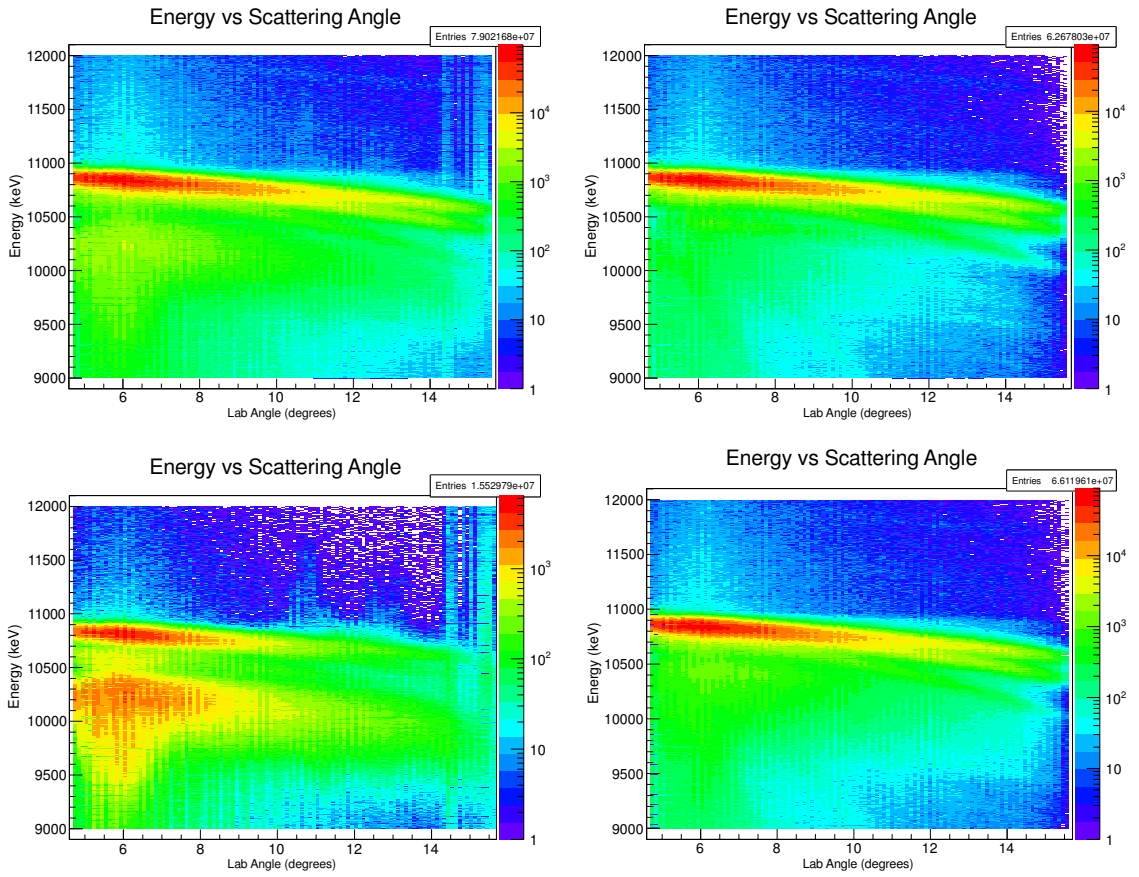

Figure 5.2: Top Left: All events in the S2 with energy detected in a ring between 9 and 12 MeV. Top Right: Events in the S2 with a 3% agreement between ring and sector energy. Bottom Left: Events excluded between top two histograms. Bottom Right: All events between 9 and 12 MeV with equal energy and corrections for events with split energy.

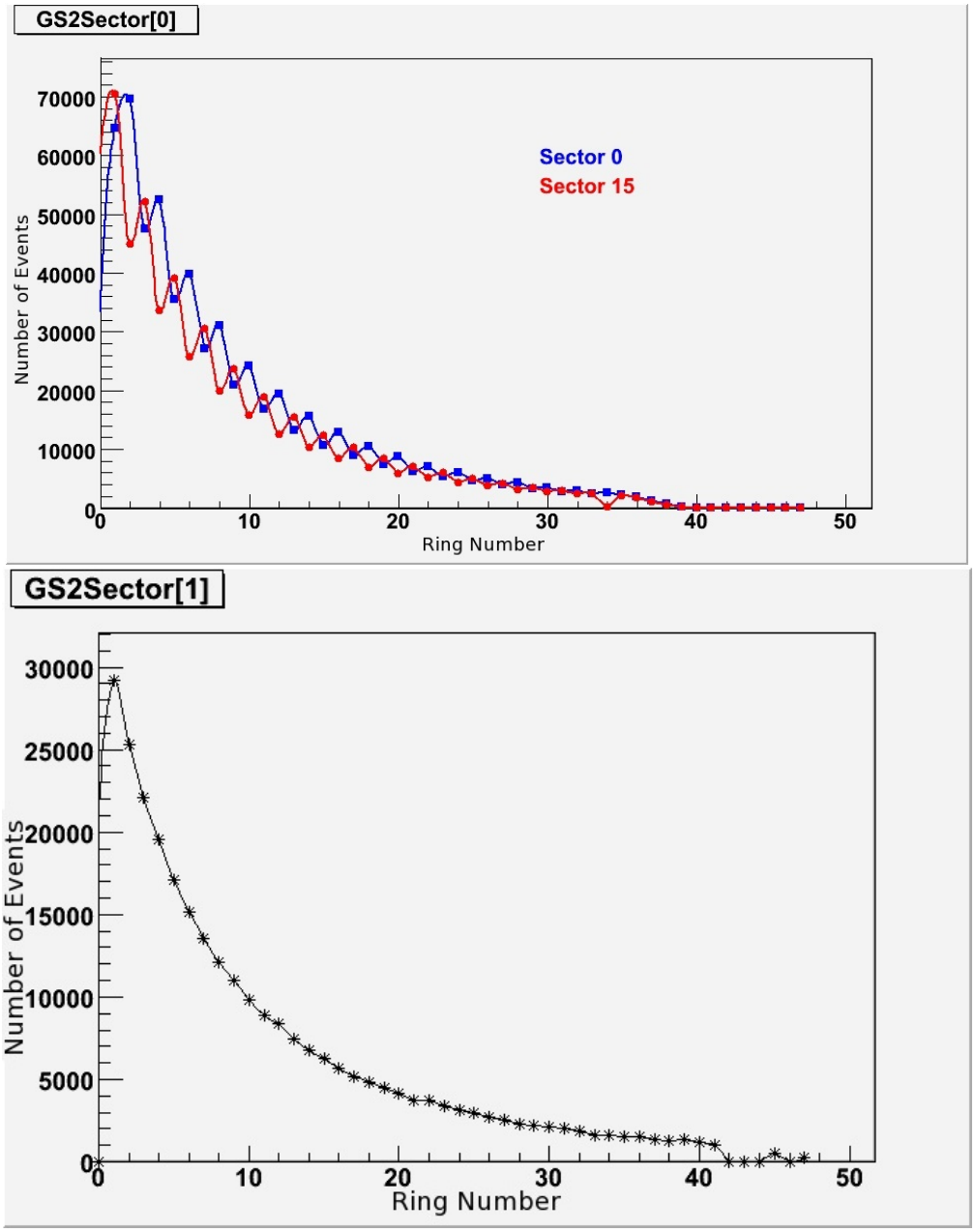

Figure 5.3: Top panel shows the cross talk observed in sectors 0 and 15 in the S2 detector creating an oscillatory output. Bottom panel shows the observed output for elastic scattering from sector 1. Similar output is observed in all other sectors as well. Both figures show ^{8}Li elastically scattered from ^{19}F as a function of S2 ring number.

the inner strips. The suspected cause of the problem is a type of crosstalk or inter-strip effect (i.e. a hit somewhere other than the active area defined by the p+ and n+ implantation) [45]. Requiring equal energies in the sectors and rings of the S2 detector was tested as a solution to the observed crosstalk effect. However, even with a stringent requirement of a 1% agreement between energies from the two sides of the detector, the oscillatory behavior was still observed.

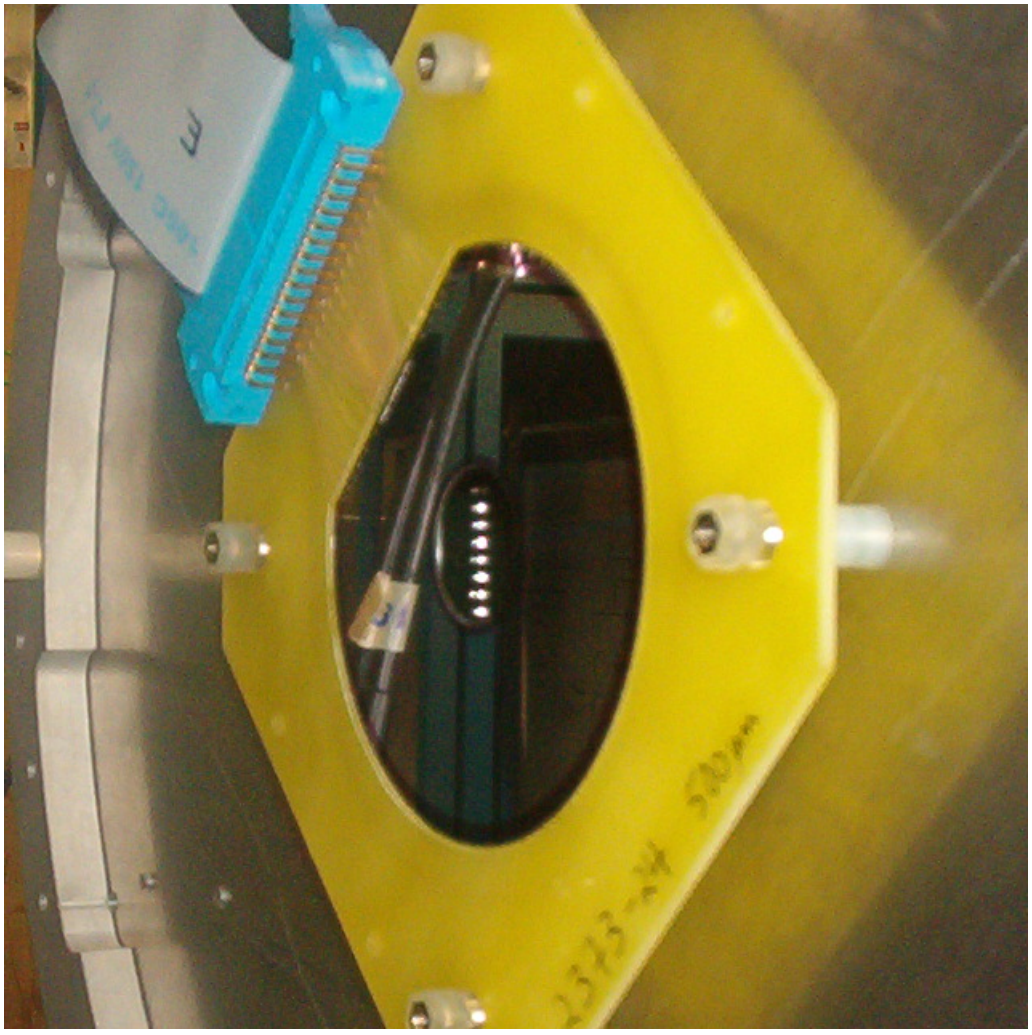

Figure 5.4: S2 detector mounted in the TUDA chamber.

After further investigation of the matter without discovering a concrete solution, it was

decided to omit the events from sectors 0 and 15 in the S2 detector. These two sectors amount to under 1/8 of the active area of the detector. The exclusion of the two sectors is only a minor problem, as the statistics at the small scattering angles covered by the S2 detector are quite sufficient even with the omitted events.

5.2 Data Reduction

Following implementation of the corrections and techniques discussed in the previous sections of this chapter, the spectra are analyzed and further refinements are made by imposing energy and timing cuts. Optimizing the cuts and the gates on the data, the background is reduced while accepting as many good events as possible. Identifying the remaining background peaks helps when applying multiple peak fits to the data in the S2 detector. By performing a multiple peak fit the data in the S2 can be extracted even though a recoil coincident event with the LEDA detector was not available.

5.2.1 Background Reduction

With previous background reduction and corrections applied, the data from the S2 detector is further constrained by energy and time cuts. Previous energy gates between the rings and sectors in the S2 detector as discussed in section 5.1.4 ensure that the energy deposited in the rings and sectors agrees within 3%. This value is used as a rough initial cut to remove most background events in the S2. A further refinement by means of a manually created gate results in the sector energy vs. ring energy cut shown in Figure 5.5.

Timing data is also used to gate on the loci of interest and reduce background events. Identification of various peaks in the TDC data was done by placing tight windows on known loci in the energy spectrum and assessing the corresponding peak in the timing data. A timing window is placed between channels 306 and 328 on the ring channels and between channels 310 and 328 on the sector channels. When both the refined energy cut and the timing cut are applied, the energy-angle data from the S2 detector appear in Figure 5.7. TDC spectra for the S2 detector are shown in Figure 5.6. The spectra include full TDC data before any energy or timing cuts are made for both the sectors and the rings as well as the comparison following the implementation of energy and timing cuts.

Data from the LEDA detector were easily reduced by using coincidences to separate events of interest from background. The kinematics of the ^{7}Li(^{8}Li,^{7}Li)^{8}Li reaction are such

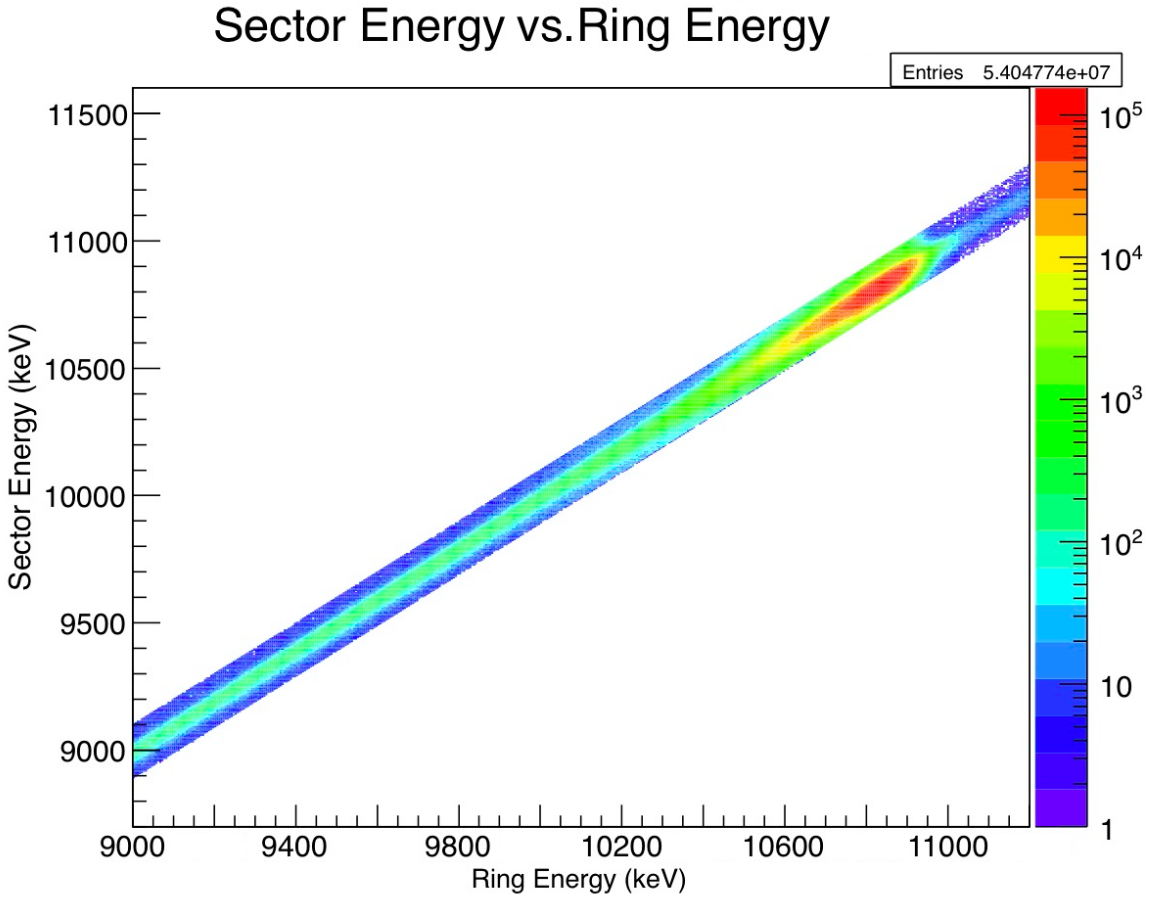

Figure 5.5: Sector energy vs. ring energy cut in the S2 detector.

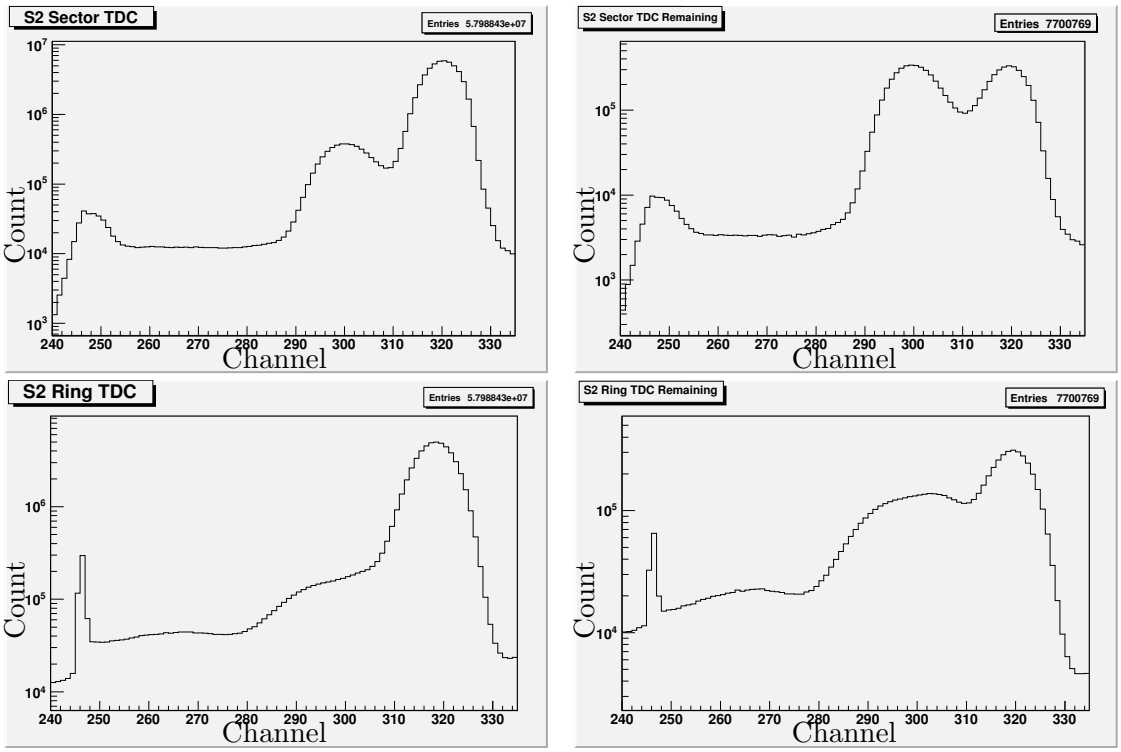

Figure 5.6: TDC spectrum from the S2 detector. The top two figures are the TDC data from the sectors while the bottom two are from the rings. The figures on the left hand side represent the full uncut TDC data for either the sectors or the rings. On the right hand side are the excluded events after energy and timing cuts are made.

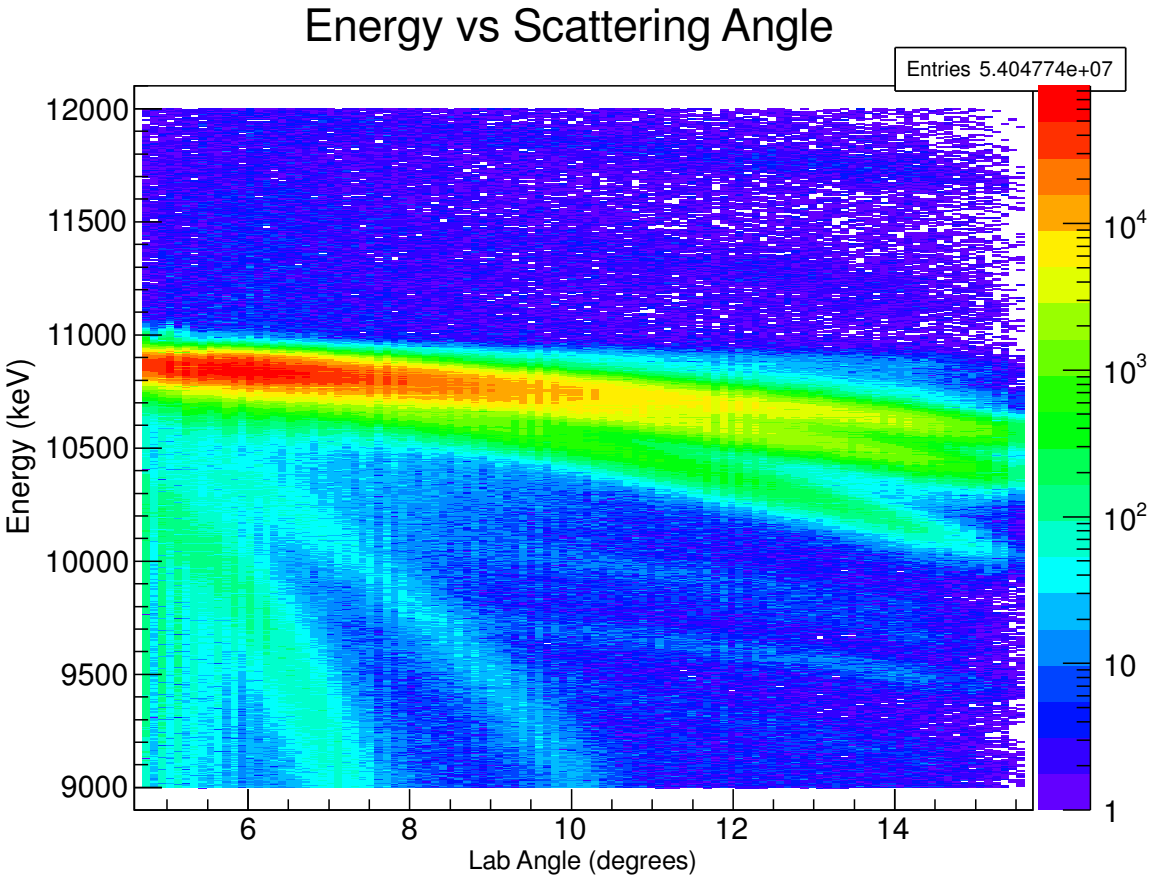

Figure 5.7: Two dimensional laboratory energy vs. angle histogram depicting the S2 data with all energy and time cuts applied. Identification of the various loci is shown in Figure 5.9. The two faint loci above the beam energy of 11 MeV located around 12 MeV and 11.5 MeV are from the positive Q value reaction of the neutron transfer between ^{8}Li and ^{12}C to the ground state and the first excited state of lithium, ^{12}C(^{8}Li,^{7}Li)^{13}C and ^{12}C(^{8}Li,^{7}Li*)^{13}C respectively.

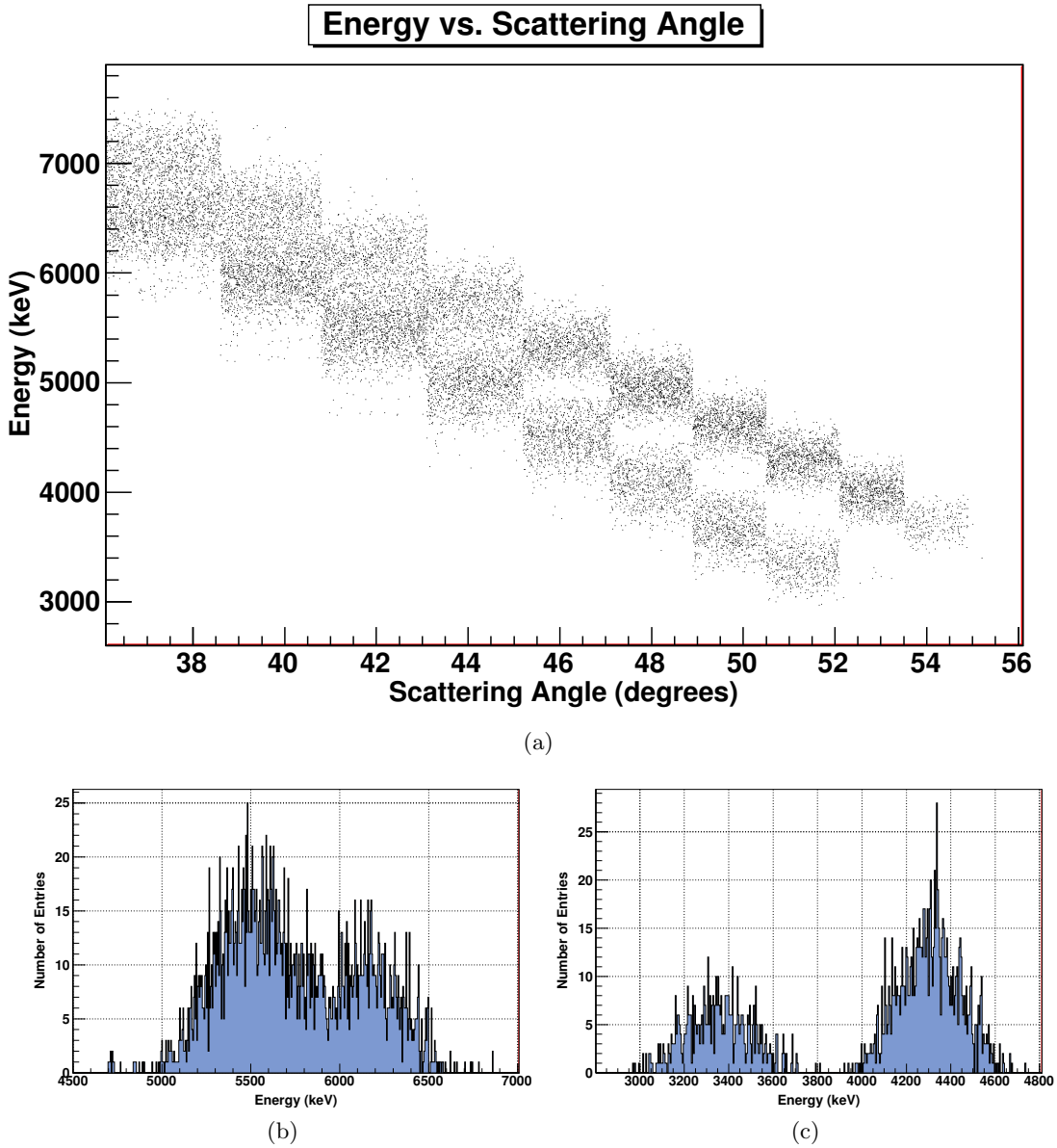

(a)

(b)

(c)

Figure 5.8: Coincidence events in the LEDA detector are shown in Figure (a). The energy spectra of the $41.0 - 43.1$ degree bin and the $50.5 - 52.0$ degree bin are shown in Figures (b) and (c) respectively. The higher energy locus represents ^{7}Li events and the lower energy locus represents ^{8}Li events.

that the angular range of both the recoil and the ejectile fall within the range of the LEDA detector. When placing the energy cuts care was taken to ensure events were not double counted. Following the detection of an event inside the ^{8}Li window and coincidence event inside the ^{7}Li window, the individual energies are summed and compared to an acceptance gate on their total energy. The total energy gate is corrected for energy loss through the target and dead layer of the LEDA detector based on energy loss calculations from SRIM [44]. Energy loss through the target is on the order of 80 keV, while energy loss through the dead layer of the LEDA ranged from 130 keV to 180 keV. Longitudinal and lateral straggling were also calculated and found to be on the order of 2.03° and 1.25° respectively through the target and 2.16° and 1.57° respectively in the detectors for ^{8}Li at 11 MeV.

Figure 5.8 shows the detected coincidences of ^{7}Li and ^{8}Li in the LEDA detector. The top panel depicts the data at a scattering angle of 39 degrees and the bottom panel at a scattering angle of 49 degrees. The ^{7}Li events are located at a higher energy than the ^{8}Li events at a given angle. Due to the coincidence requirement and the total energy gate the background in the LEDA is effectively reduced to zero.

5.2.2 S2 data reduction

Initial plans for data analysis were for the ^{8}Li events in the S2 detector to be separated out from the large number of background events due to elastic scattering through coincidences with ^{7}Li in the LEDA detector. The kinematics of the ^{7}Li(^{8}Li,^{7}Li)^{8}Li reaction are such that when the ^{8}Li recoil is incident within the angular range of the S2, then the low energy ^{7}Li recoil would fall within the angular range of the LEDA detector. As previously mentioned, this did not happen because no LEDA events at low energy were recorded.

This abnormally high cutoff energy in the LEDA detectors could originate from one of two scenarios; either the cutoff value was set in post processing software or in the hardware. Following the discovery of the missing coincidence, all software programs were checked to ensure the low energy coincidence events from the LEDA were not being removed in data processing. After no artificially introduced cutoff value was discovered in the software, the conclusion that it was a low threshold for the Silena 9418/6V ADCs was reached. Typical thresholds for the ADC for a TUDA experiment omit the lowest 48 channels [45], however it appears that somehow all events in the lowest 128 channels of the ADC were discarded resulting in the coincidence events being discarded. The cause for the abnormally high thresholds is unknown, but appeared to be a default setting of a previous experiment [45].

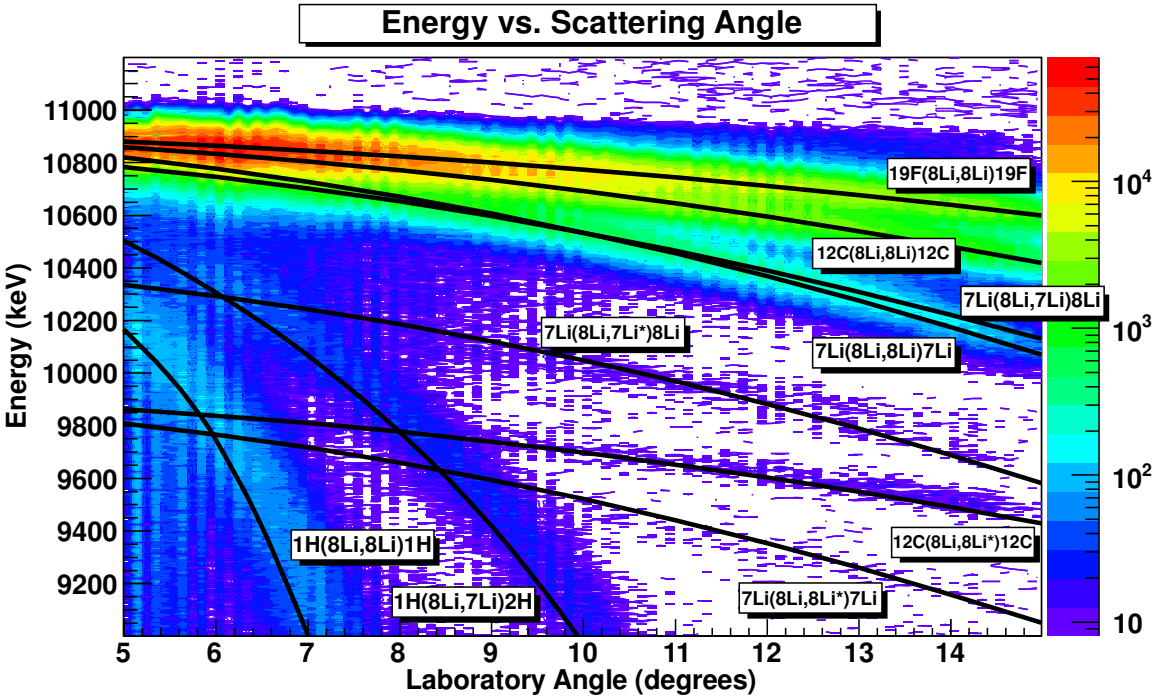

Figure 5.9: Two dimensional histogram of data from the S2 detector after final cuts with identified loci. No evidence for the loci representing the ^{19}F(^{8}Li,^{8}Li*)^{19}F, ^{19}F(^{8}Li,^{7}Li)^{20}F, ^{7}Li(^{8}Li,^{8}Li)^{7}Li*, and the ^{7}Li(^{8}Li,^{7}Li)^{8}Li* reactions were evident above the background.

While these coincidence events were missed, the data from the S2 detector are not completely lost. With the extensive background reduction and tight cuts placed on the data as previously discussed, the lithium events are separable in a limited range. In Figures 5.7 and 5.9 the ^{8}Li and ^{7}Li elastic scattering locus can be seen separated from the background due to elastic scattering off of carbon and fluorine above 12 degrees.

5.2.3 Fitting the S2 data

Without the coincidences to separate the ^{8}Li and ^{7}Li elastic scattering locus from the background, a multiple peak fit for the S2 data is required. Even though the S2 detector collected data between 4.7 and 15.7 degrees in the laboratory frame, the kinematics of the reactions made separating the lithium locus from the larger carbon and fluorine loci impossible at angles below 9 degrees. From 9 degrees and up the lithium peak is sufficiently separated from the background to perform a reliable multiple peak fit.

The full multi-peak fit includes: a linear background, three gaussians for ^{8}Li scattered from lithium, carbon, and fluorine respectively, and a fourth gaussian for a background peak. The fourth gaussian describes a small peak with a nearly uniform energy profile over the entire angular range which we attribute to elastic scattering from heavy contaminants; Fe, Te, Ba, and Pb were all known to be present in the target at trace levels. The tail of this locus is visible in Figure 5.7 around an energy of 10.8 MeV above the fluorine elastic locus . Performing the fit while excluding this background gaussian resulted in a poor overall fit to the data; however, the resulting values for the amplitude of the lithium peak are similar to the fits with the background gaussian included. The average change in the integral of the lithium peak was a reduction of 1% when including the background peak.

Constraints placed on the fitting parameters for the multiple peak fit were left fairly loose. The individual widths of the gaussians are required to be within 50% of each other, while the mean values of the fits are required to be within 5% of the calculated values taking into account kinematics and energy loss calculations.

A typical multiple peak fit for the S2 data is shown in Figure 5.10. In green is the elastic lithium peak, and in red is the total fit. The black peaks are elastic scattering from carbon, fluorine and trace heavy contaminants. The small peaks located around 9.6 MeV and 9.9 MeV, which are not shown in Figure 5.10 but are visible in Figure 5.9, are inelastic scattering to the first excited state in ^{8}Li and ^{7}Li. The peak at 9.6 MeV is the ^{8}Li from inelastic scattering to the first excited state of ^{8}Li at 0.98 MeV from carbon. The peak at 9.9

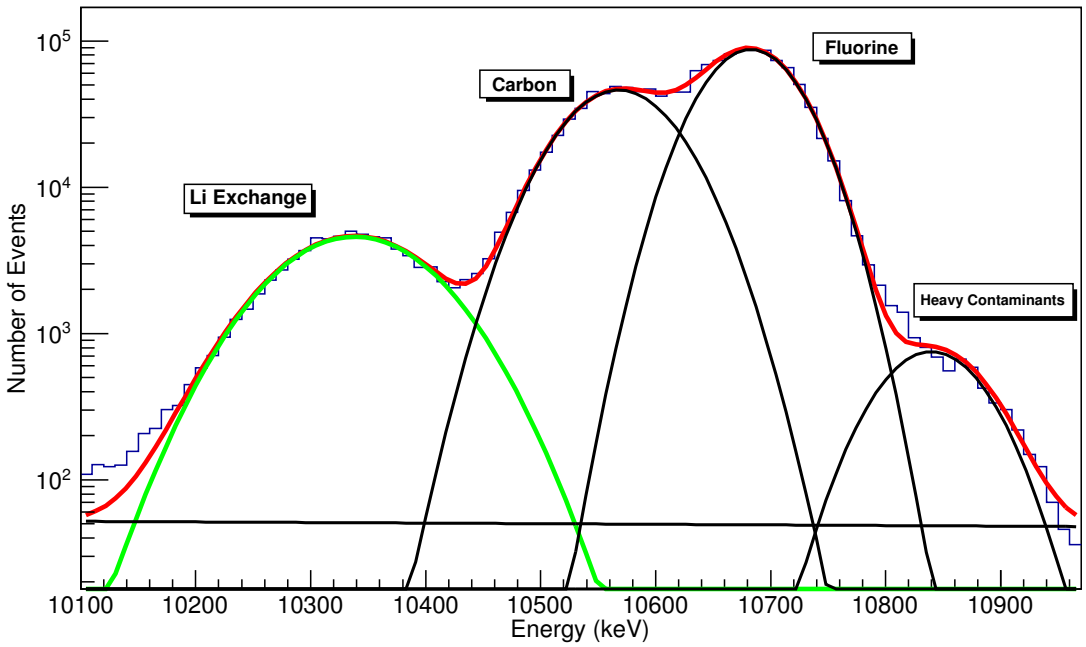

Figure 5.10: Data from the S2 detector between 12 and 13 degrees in the laboratory frame. The green curve represents ^{8}Li and ^{7}Li particles from the ^{7}Li + ^{8}Li reaction. The black curves are elastic scattering from carbon, elastic scattering from fluorine, and a background peak that is nearly uniform across all angles in the S2 detector at the beam energy attributed to elastic scattering from trace heavy contaminants. The red curve is the sum of the four gaussians and the linear background.

MeV is attributed to ^{8}Li from inelastic scattering to the first excited state in ^{7}Li at 0.48 MeV from the ^{7}Li(^{8}Li,^{7}Li)^{8}Li reaction. Due to the small size of these peaks their contributions are included in a linear background. Also approximated as a part of the linear background is the small peak located above the beam energy around 11.3 MeV, also not shown in Figure 5.10 but visible in Figure 5.9, which is the result of scattering to the first excited state of ^{7}Li in the neutron transfer reaction with carbon. The small peaks are omitted from view in Figure 5.10 to show the details in a narrower range around the peaks of interest. The small excess of events above the fit at the low energy tail of the "Li Exchange" peak amounts to only 0.37% of the total ^{8}Li and ^{7}Li events from the ^{7}Li(^{8}Li,^{7}Li)^{8}Li reaction deduced from the fit.

5.2.4 Error estimates

The errors assigned to the reduced data from the S2 and LEDA detectors are the results of multiple sources. As each detector requires unique data analysis methods, their sources of errors will be discussed separately.

For the S2 detector the large number of events resulted in small statistical error values. Typical statistical errors from the gaussian fits are on the order of $\pm$1.5% or less. The largest sources of error for the S2 data are due to systematics. These errors arise from the extensive measures required to reduce the background and the difficulty in accurately performing multiple peak fits. The similar timing and energy of ^{8}Li nuclei scattered at small angles from either ^{19}F or ^{7}Li enabled the use of the ^{19}F peak to estimate the systematic error due background reduction cuts and fitting. By comparing the peaks for the ^{19}F scattering before and after implementing background reduction an estimated error of $\pm$5% due to the energy and time gates placed on the S2 data is estimated. The final source of error for the S2 detector arises from a variation in the determined beam offset position. Varying the offset by 0.10 cm in all directions and comparing the results, a systematic error of $\pm$4.7% from the beam offset applies to the S2 data.

The errors for the data from the LEDA detector have similar sources as the errors for the data from the S2 detector; their values however, are notably different. Starting with the much higher statistical uncertainty for the angular range of the LEDA detector the statistical errors range from $\pm$3% to $\pm$6% and are the most significant source of error for the LEDA data. The ability to use a coincident detection to separate the LEDA data from the background either eliminated or greatly reduced the systematic errors compared to the

S2 data. Systematic errors due to the placement of the gates on the coincidence events in the LEDA are determined by shifting the position of the gate and comparing the results. Even with unreasonably large shifts applied to the coincidence gate the change in the results is minimal, translating into a systematic error of only ±0.6%. The same method of varying the beam offset position as employed for the S2 data results in a systematic error on the LEDA data due to the beam offset of ±2.5%. This value is lower then the value for the S2 detector due to the rings being larger in the LEDA detector and thus less sensitive to slight offsets from the central position.

Detector	Statistical Error	Systematic Error	Total
S2	0.3-1.5%	6.9%	6.9 - 7.1%
LEDA	2.8-6.2%	2.6%	3.8 - 6.7%

Table 5.4: Contributions to the error for the angular distribution data from the S2 and LEDA detectors.

The error associated with the Monte Carlo program for determining detector geometrical coverage discussed in Section 5.1.3 has been included in the error values for the beam offset for each detector. The method used to estimate the error from the beam offset also accounted for the error associated with the Monte Carlo program itself when the value was calculated.

Total error values for the various angular bins covered by the S2 and LEDA detectors after adding the separate sources of systematic error together in quadrature with the statistical error fall into the range of ±4% to ±7%. Even with the significantly larger statistics in the S2 detector compared with the LEDA detector, the error on the S2 data is larger than that from the LEDA due to the extra measures required to extract the data from background events.

The final results of all the data reduction, multiple peak fitting and error analysis discussed in this chapter are shown in Figure 5.11. Data for the S2 includes the offset corrections and has the data binned in 1 degree bins in the laboratory frame. The LEDA data are presented using the natural bin size based on the ring spacings. These results are used to fit the optical potential parameters and spectroscopic amplitude using SFRESCO.

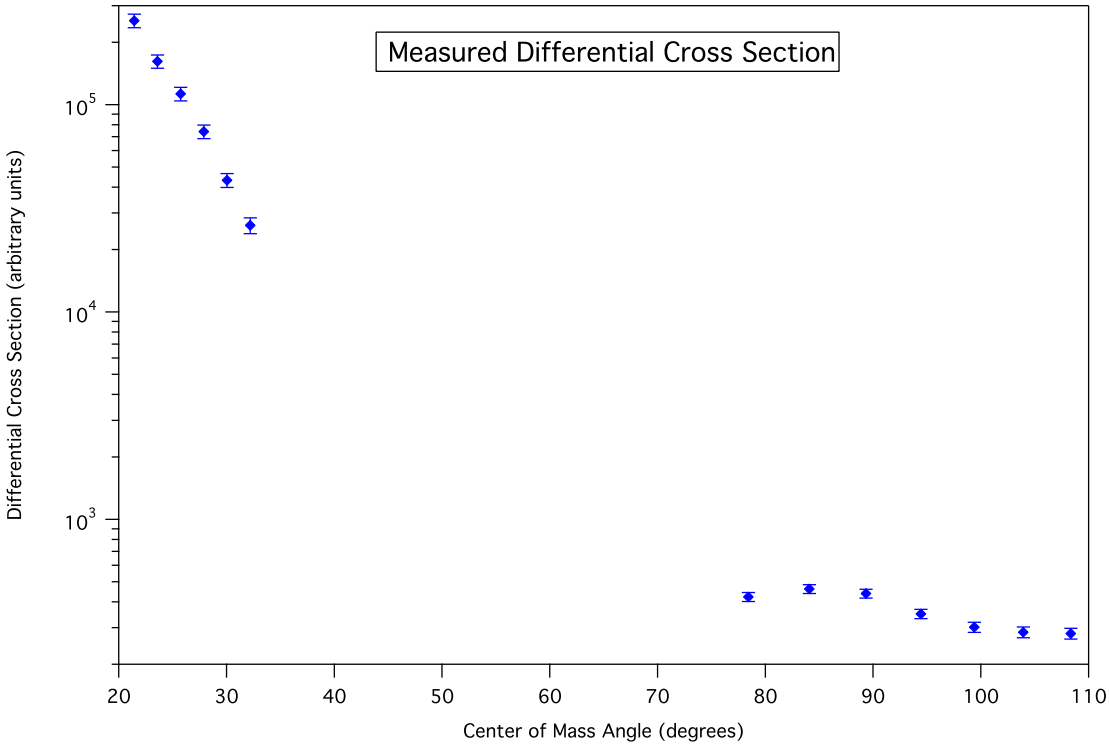

Figure 5.11: Measured differential cross section of the ^{7}Li(^{8}Li,^{8}Li)^{7}Li reaction at $E_{lab} = 11$ MeV following corrections for detector geometry and beam offset. All statistical and point-to-point systematic errors are included.

5.3 SFRESCO Fit

Our initial intentions were to run the experiment at three separate energies (8 MeV, 11 MeV, and 13 MeV). With the three separate runs the spectroscopic amplitude could be individually fit at all energies since its value is energy independent. The only energy dependent values in the fit are the parameters for the entrance and exit channel optical potentials. Due to limited beam time the decision was made to omit the 8 MeV run during the experiment. The run at 13 MeV displayed a broad background of unknown origin in both detectors that dwarfed all other signals in the LEDA detector and is of comparable size to the other peaks in the S2 detector. An unfortunate effect of this large background is a peak height of only one tenth the peak height observed in the 11 MeV run for data in the LEDA detector. Another problem is that the multi-peak fit in the S2 is prone to very large systematic errors. The resulting errors with the small number of events and difficulty of accurately reducing the background resulted in the 13 MeV data being unusable.

The optical potential for the interaction between the ^{8}Li and ^{7}Li nuclei at 11 MeV was initially set to the values from the potential for the interaction at 13 MeV taken from reference [34]. The FRESCO input file used for all SFRESCO fits is shown in Figure B.3 and the SFRESCO input file is of the form shown in Figure B.7. Included in this SFRESCO input file are variables for the normalization of the dataset and the spectroscopic amplitude. The variable "norm1" is required to fit for the normalization of the dataset to the calculated absolute differential cross section determined by SFRESCO. The $p_{3/2}$ spectroscopic amplitude fit value is initially set at the value from Wiringa [33]. These details will be further discussed in Chapter 6.

Chapter 6

Angular Distribution Analysis

The results of the data extraction, processing, and reduction will be discussed in this chapter, highlighting the details of the fitting process and different methods used in obtaining an accurate fit.

6.1 Binding Potential and Single Particle ANC

The spectroscopic amplitude obtained from a SFRESCO fit is the square root of the spectroscopic factor, S, shown in Equation 2.90. In order to calculate the $p_{3/2}$ ANC from the spectroscopic factor, the single particle ANC given by the parameter $b_{p_{3/2}}$ in Equation 2.90, is required.

Table 3.2 shows various valence neutron binding potentials that were examined for the ^{8}Li nucleus. Potential 7, the binding potential of Davids and Typel [38] produced the best quality of fit of published potentials when the computed bound state wavefunction was compared to the Variational Monte Carlo (VMC) wavefunction of R. Wiringa [33] shown in Figure 6.1. From the variation of the binding potential parameters an improvement to the quality of fit when compared to the VMC results of R. Wiringa was obtained.

The fit results from all the potentials listed in Table 3.2 are shown in Figure 6.1, the best fitting parameters to the VMC wavefunction of R. Wiringa are from potential 14. The parameters of this new potential and the Davids and Typel potential are shown in Table 6.1. These binding potentials are both for the $p_{3/2}$ orbital; as explained above, the binding potential for the small $p_{1/2}$ orbital component is held fixed. The potential used for the $p_{1/2}$ orbital is given in Table 4.1. The fitting process described next is performed using potential

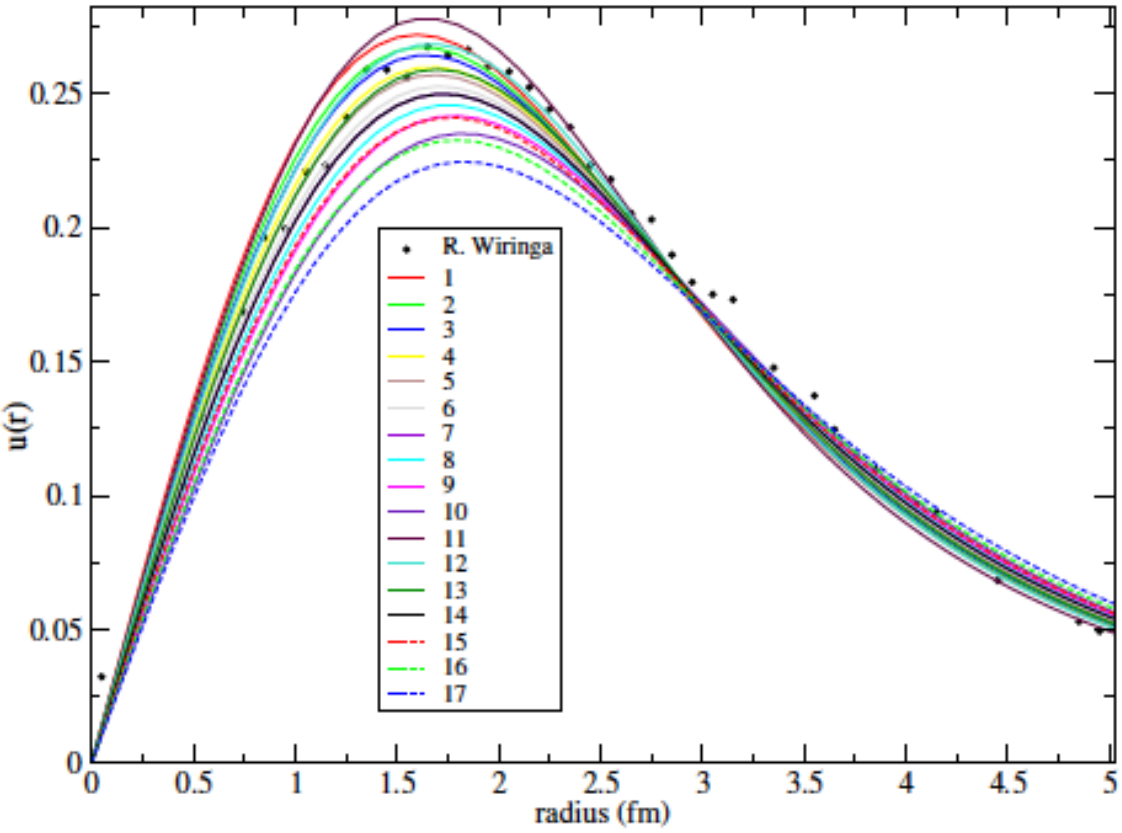

Figure 6.1: Bound state reduced radial wavefunctions for the valence nucleon in the A=8, T=1 system. Dots show VMC calculations by R. Wiringa [33] of $\langle {}^7\mathrm{Li}—{}^8\mathrm{Li}\rangle_{\mathrm{p}_{3/2}}$. The binding potential parameters are given in Table 3.2.

Pot #	V (MeV)	r_V (fm)	a_V (fm)	$b^2(\mathrm{fm}^{-1})$	Ref
1	43.19	2.50	0.65	0.604	[38]
2	43.53	2.50	0.60	0.560	[34]

Table 6.1: Binding potentials for the $\mathrm{p}_{3/2}$ orbital of the valence neutron of ^{8}Li with corresponding single particle ANC values from reference [34].

2 from Table 6.1 for the $p_{3/2}$ orbital. Further calculations will thus be using the square of the single particle ANC value of 0.560, obtained from reference [34].

6.2 Data fitting

Without previously determined values for the parameters of the optical potential the problem is to fit for both the optical potential parameters and the spectroscopic amplitude simultaneously. An initial fit is performed for only the optical potential parameters while the normalization factor and the spectroscopic amplitude are held fixed. A secondary fit is then performed using the results from the initial fit as starting values for the optical potential parameters, and the normalization and spectroscopic amplitude are allowed to vary. It was required to add a fitting parameter for the normalization as it could not be measured during the experiment due to unreliable readings from the channeltron. The purpose of the initial fit is to reduce the degrees of freedom by fixing variables that have previously determined values and allowing a subset of the variables to approach their minima independently.

6.2.1 Initial fit

As previously discussed in section 4.3.1 no optical potential for the ^{8}Li+^{7}Li reaction at exactly 11 MeV is to be found in the literature, therefore the parameters of this potential are derived from systematic studies of ^{8}Li elastic scattering data at laboratory energies from 13 to 20 MeV with targets in the mass range of 1 to 58 amu [41]. The core-core potential for the interaction between ^{7}Li and ^{7}Li is shown in Table 4.1. The full FRESCO input file is the same as that shown in box B.3 except for the binding potential discussed in section 6.1.

The spectroscopic amplitudes for the $p_{1/2}$ and $p_{3/2}$ orbitals are fixed at the values derived from variational Monte Carlo calculations of 0.0737 and 0.868 respectively [33]. The initial value for the normalization factor is set at 9.4×10^{-2}, which was determined by varying only the normalization parameter. The results of the initial fit are shown in Table 6.2 along with the initial values for the optical potential. The parameters for this initial fit are left unconstrained.

These results shown in Table 6.2 are used as starting values for the optical potential parameters in a secondary fit. This secondary fit allows for the optical potential parameters, the spectroscopic amplitude, and the normalization factor to be fit simultaneously.

	V (MeV)	r_V (fm)	a_V (fm)	W (MeV)	r_W (fm)	a_W (fm)
Initial	175	0.64	0.8	16.9	1.09	0.8
Fit	175	0.50	0.96	5.3	1.5	0.53

Table 6.2: Parameters for the entrance and exit channel optical potential for the $p_{3/2}$ orbital interaction between ^{8}Li and ^{7}Li. The fit parameters are the results of an SFRESCO minimization to the dataset using initial parameters for the potential taken from reference [34].

6.2.2 Secondary Fit

The results of the initial fit shown in Table 6.2 are used as starting parameters for the optical potential in a new fit where the spectroscopic amplitude for the $p_{3/2}$ orbital is varied as a fit parameter. Prior to the secondary fit, a Minuit scan[1] for each fit parameter is performed. The purpose of running the Minuit scan is to aid in selecting the limits to be placed on the fitting parameters and in ensuring these limits are not too narrow. Results of the Minuit scan can be seen in Figure 6.2. Constraints placed on the fit parameters are on the order of ±20%. The results from the secondary SFRESCO minimization are summarized in Table 6.3. The results of the fit are also displayed in Figure 6.3, which shows the SFRESCO fit to the data as a solid line and the data as points.

	V	r_V	a_V	W	r_W	a_W	norm	$a_{3/2}$
Value	173.8	0.4995	0.957	5.28	1.514	0.531	9.35×10^{-3}	0.884
Error	2.8	0.0084	0.017	0.37	0.021	0.082	0.44×10^{-3}	0.218

Table 6.3: Fit results from SFRESCO for the optical potential parameters, normalization, and spectroscopic amplitude for the $p_{3/2}$ orbital. Limits placed on the parameters prior to performing the fit are indicated in the individual plots for each parameter in Figure 6.2. Units for the depths are in MeV, the reduced radii are in fm, and the diffusenesses are in fm.

Due to the omission of the data from the 8 MeV and 13 MeV runs on account of the problems discussed in Chapter 5, the theoretical fit to the data is limited to the single dataset from the 11 MeV run. This limitation of using only a single dataset results in a

[1]For more information on the Minuit scan function please refer to Appendix C.

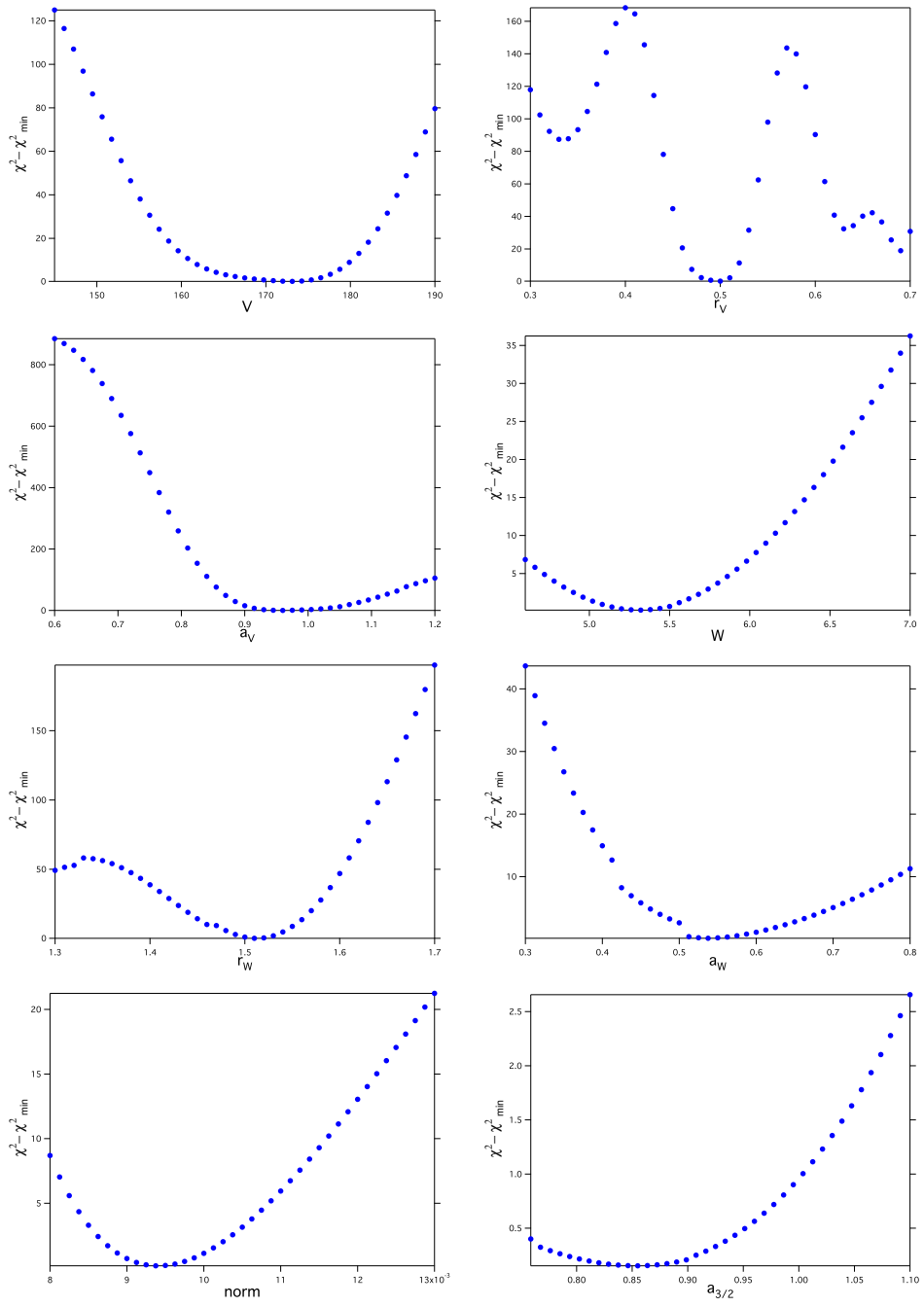

Figure 6.2: Results of the Minuit scan function based on the parameter limits used for the SFRESCO fit.

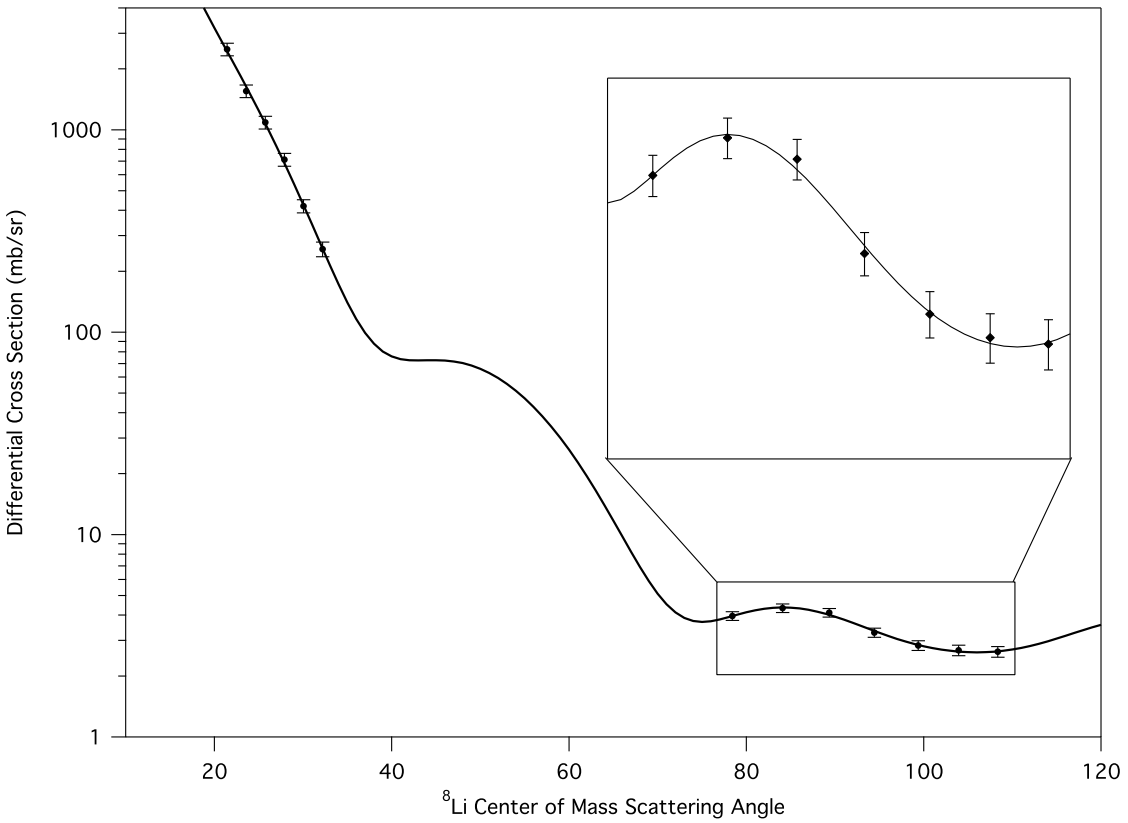

Figure 6.3: Measured and calculated differential cross section for the ^{7}Li(^{8}Li,^{8}Li)^{7}Li reaction at $E_{lab} = 11$ MeV. Fit results from SFRESCO correspond to the values shown in Table 6.3.

substantial error for the final extracted value of the spectroscopic amplitude. The initial objective of fitting for the spectroscopic amplitude at the three beam energies to reduce the error was not realized.

Chapter 7

Results and Discussion

From the results of the fit for the spectroscopic amplitude in Chapter 6 the ANC for the valence neutron in ^{8}Li is determined and a value for $S_{17}(0)$ is calculated. The value obtained for the S factor is discussed and compared to previously measured and calculated values.

7.1 Previous Results

There have been numerous estimates made of the astrophysical S factor $S_{17}(0)$ through direct and indirect methods. The paper by R. H. Cyburt, B. Davids, and B. K. Jennings of Reference [2] has a compilation of previously measured values of S_{17}. Using these previous values for the S factor two estimates are recommended by the authors:

$$S_{17}(0) = 20.7 \pm 1.2\,\mathrm{eV\,b}, \tag{7.1}$$

using only results from radiative capture experiments, and

$$S_{17}(0) = 17.5 \pm 2.5\,\mathrm{eV\,b}, \tag{7.2}$$

from experiments that used Coulomb dissociation reactions. The errors for both of these values arise from assuming the complete independence of the individual data sets used to calculate the values.

7.1.1 ANC

The previous measurement resulted in a value for the $p_{3/2}$ orbital ANC for ^{8}Li of

$$C^2_{p_{3/2}} = 0.384 \pm 0.038\,\mathrm{fm}^{-1} \tag{7.3}$$

The reaction of the study was ^{13}C(^{7}Li,^{8}Li)^{12}C at 63 MeV [32]. A value was also obtained from the same study for the $p_{1/2}$ orbital of

$$C^2_{p_{1/2}} = 0.048 \pm 0.006\,\mathrm{fm}^{-1} \tag{7.4}$$

Of particular interest is the ratio between $C^2_{p_{1/2}}$ and $C^2_{p_{3/2}}$, the two ANC values, which was measured for the first time in this study. The error is derived from the uncertainties arising from the angular range used in the fits and uncertainties in the optical potentials.

$$\frac{C^2_{p_{1/2}}}{C^2_{p_{3/2}}} = 0.13 \pm 0.02. \tag{7.5}$$

7.1.2 S factor

In order to calculate the $S_{17}(0)$ from the ^{8}Li ANC the ratio between the ANCs of the mirror systems $\langle ^8\mathrm{B}(2^+)|^7\mathrm{Be}(\frac{3}{2}^-)\rangle$ and $\langle ^8\mathrm{Li}(2^+)|^7\mathrm{Li}(\frac{3}{2}^-)\rangle$ is required. In Reference [46], the relation between ANCs and charge symmetry breaking nucleon-nucleon (NN) interactions in mirror states is studied. Ratios between mirror ANCs are calculated using two separate effective NN potentials: the Volkov potential V2 [47], and the Minnesota (MN) potential [48].

		$C^2_{p_{1/2}}$	$C^2_{p_{3/2}}$	C^2_p
V2	^{8}B	0.0886	0.6850	0.7736
	^{8}Li	0.0706	0.6539	0.7244
	Ratio	1.256	1.048	1.068
MN	^{8}B	0.0811	0.5602	0.6413
	^{8}Li	0.0682	0.5193	0.5875
	Ratio	1.189	1.079	1.092
$\mathrm{Ratio}_{\mathrm{Average}}$		1.22 ± 0.03	1.06 ± 0.02	1.08 ± 0.01

Table 7.1: Calculated squares of ANCs (in fm^{-1}) for $p_{1/2}$ and $p_{3/2}$ orbitals and their sums. Calculations were performed with two NN potentials, V2 and MN. The ratios of similar quantities for the mirror overlap are given for each potential [46]. The average of the ratios of the two potentials is also given.

Experimental measurements of the ^{8}Li neutron ANC from Reference [32], and the ^{8}B proton ANC from Reference [28] were compared with the theoretically calculated values. In both cases the experimentally determined ANC values were much smaller than the calculated values, but the ^{8}B/^{8}Li ANC ratios were in excellent agreement.

Using the theoretically determined ratios along with experimental values for the ^{8}Li ANCs from Reference [32], the S factor, $S_{17}(0)$, was calculated in Reference [46]. Using the V2 potential a value of $S_{17}(0) = 17.8 \pm 1.7$ eV b was obtained, and a value of 18.2 ± 1.8 eV b was obtained using the Minnesota (MN) potential.

The most recent evaluation, reported by Adelberger et al.,

$$S_{17}(0) = 20.8 \pm 0.7(\text{expt}) \pm 1.4(\text{theor})\,\text{eVb} \tag{7.6}$$

from Reference [1] is based only on direct radiative capture measurements.

7.2 New Results

The results presented in Chapter 6 will be analyzed and compared to previously published values. Calculated values for the ^{8}Li $p_{3/2}$ ANC and resulting $S_{17}(0)$ are presented and discussed.

7.2.1 ANC

Referring to Figure B.3 the $p_{3/2}$ spectroscopic amplitude appears twice in the FRESCO input file, once for the entrance channel and once for the exit channel. Equation 2.87 shows that it is the product of the spectroscopic factors of the entrance and exit channels that contribute to the differential cross section. Since the spectroscopic amplitudes are directly related to the spectroscopic factors through Equation 2.86, and due to the symmetry of the lithium transfer reaction only one of the spectroscopic amplitudes for a given orbital needs to be fit while the second may remain fixed. The results of the SFRESCO fit shown in Table 6.3 give the spectroscopic amplitude for the entrance channel $p_{3/2}$ coupling value with the exit channel $p_{3/2}$ coupling value fixed at the initial value of 0.868. From these values the spectroscopic factor S, shown in Equation 2.90, is calculated to be

$$S_{3/2} = 0.77 \pm 0.19. \tag{7.7}$$

From Equation 2.90 the ANC value for a given orbital is calculated from the spectroscopic factor and the single particle ANC. Using the single particle ANC value for potential 2 from Table 6.1, the $p_{3/2}$ ANC value is calculated,

$$C^2_{p_{3/2}}(^8\mathrm{Li}) = 0.43 \pm 0.11\,\mathrm{fm}^{-1}. \tag{7.8}$$

Without being able to separately fit for both the $p_{1/2}$ and $p_{3/2}$ spectroscopic amplitudes, the $p_{1/2}$ ANC must be calculated from the $p_{3/2}$ ANC. The ratio between the two ANC values is taken from experimental results [32] and shown in Equation 7.5. Theoretical calculations using the MN potential have also been shown to agree with this ratio [46]. The V2 potential however predicts a much lower ratio of 0.108. Using the experimentally determined ratio that agrees with the MN predicted ratio results in a $p_{1/2}$ ANC of

$$C^2_{p_{1/2}}(^8\mathrm{Li}) = 0.056 \pm 0.016\,\mathrm{fm}^{-1}. \tag{7.9}$$

These values are in good agreement with previous measurements by L. Trache et al. from Reference [32]. From the ^{13}C(^{7}Li,^{8}Li)^{12}C neutron transfer reaction at 9 MeV/nucleon values of $C^2_{p_{3/2}}(^8\mathrm{Li}) = 0.384 \pm 0.038\,\mathrm{fm}^{-1}$ and $C^2_{p_{1/2}}(^8\mathrm{Li}) = 0.048 \pm 0.006\,\mathrm{fm}^{-1}$ were obtained.

Using the average of the ratio between the ^{8}Li and ^{8}B nuclei for the V2 and MN potentials from Table 7.1, the ^{8}B ANC values are calculated from the expressions $C^2_{p_{1/2}}(^8\mathrm{B}) = 1.22\,C^2_{p_{1/2}}(^8\mathrm{Li})$, and $C^2_{p_{3/2}}(^8\mathrm{B}) = 1.06\,C^2_{p_{3/2}}(^8\mathrm{Li})$ to be

$$C^2_{p_{1/2}}(^8\mathrm{B}) = 0.068 \pm 0.020\,\mathrm{fm}^{-1}, \tag{7.10}$$

and

$$C^2_{p_{3/2}}(^8\mathrm{B}) = 0.46 \pm 0.11\,\mathrm{fm}^{-1}. \tag{7.11}$$

Excellent agreement is observed when comparing these results to previously measured values of G. Tabacaru et. al, $C^2_{p_{1/2}}(^8\mathrm{B}) = 0.052 \pm 0.006$ fm^{-1} and $C^2_{p_{3/2}}(^8\mathrm{B}) = 0.414 \pm 0.043$ fm^{-1} [29].

7.2.2 S factor

From the calculated ^{8}B ANCs from section 7.2.1 the astrophysical S factor, $S_{17}(0)$, is calculated using Equation 2.99. A value of

$$S_{17}(0) = 20.2 \pm 4.4\,\mathrm{eVb}, \tag{7.12}$$

is obtained.

This value is slightly larger than but completely consistent with that implied by previous ANC measurements. Compared to values from previous Coulomb dissociation experiments from Reference [2], the discrepancy between the values is on the order of 1σ. When compared to the higher value obtained from previous radiative capture experiments from Reference [2], and the latest evaluation from Reference [1] shown in Equation 7.6, there is excellent agreement.

7.3 Future Work

Due to limitations discussed in Chapter 3, the amount of usable data collected in this experiment was significantly less than expected, resulting in a large uncertainty on the spectroscopic amplitude. The results obtained are somewhat less precise than previous measurements. With increased data, at multiple beam energies, the error would certainly be reduced due to better optical model parameter determination.

A future study could investigate the transfer reaction ^{12}C(^{8}Li,^{7}Li)^{13}C which has a positive Q-value of 2.9 MeV. The positive Q-value makes separating events from background straight forward. As well, there are available optical potentials between lithium and carbon in the literature at select energies.

7.4 Conclusion

For the first time the ^{7}Li(^{8}Li,^{7}Li)^{8}Li reaction has been studied. The ^{8}Li valence neutron $p_{3/2}$ ANC has been measured, finding $C^2_{p_{3/2}}(^{8}\text{Li}) = 0.43 \pm 0.11$ fm^{-1}. Using the experimentally measured ratio between the $p_{1/2}$ and $p_{3/2}$ ANC values the $p_{1/2}$ ANC is calculated, resulting in $C^2_{p_{1/2}}(^{8}\text{Li}) = 0.056 \pm 0.016$ fm^{-1}. Using the average of the V2 and MN potentials the ^{8}B ANC values are calculated as $C^2_{p_{1/2}}(^{8}\text{B}) = 0.068 \pm 0.20$ fm^{-1} and $C^2_{p_{3/2}}(^{8}\text{B}) = 0.46 \pm 0.11$ fm^{-1} for the $p_{1/2}$ and $p_{3/2}$ orbitals respectively. From these values the astrophysical S factor, $S_{17}(0)$ is calculated to be $S_{17}(0) = 20.2 \pm 4.4$ eV b.

$S_{17}(0)$, the astrophysical S factor for the radiative capture reaction ^{7}Be + p $\rightarrow$ ^{8}B + γ, has been determined through a measurement of the ANC in the mirror nuclear system. Due to the large uncertainty, the present result is consistent with both the radiative capture measurements, and the previous indirect ANC determinations, which imply a smaller value

of $S_{17}(0)$. Improvements to the current ANC determination could be achieved with measurements of ^{8}Li + ^{7}Li elastic scattering of similar precision at different ^{8}Li beam energies.

Appendix A

FRESCO

This appendix contains FRESCO examples and tabled listings of the input parameters used to create a FRESCO input file.

A.1 FRECO Examples

An input file for a FRESCO calculation defines all the required potentials and parameters for the specified reaction. There are two different styles in which the input file can be created: a standard input, or a namelist style. In the standard input file all the variables must be inputted in a precisely formatted style where each column of the input text file is reserved for a certain variable. Rows are divided into groups corresponding to the various cards defining a logical grouping of variables for different aspects of the input. In a namelist style input file the user defines the card of interest by a character string and each variable may be freely defined by use of a "variable=value" command. The namelist style input is much easier to read and understand and as such will be the only type of input file used here.

A.1.1 Elastic scattering

As a first example, elastic scattering of deuterons incident on ^{7}Li will be calculated. Elastic scattering is the simplest calculation that can be performed with FRESCO as both the projectile and target remain in their ground states, and no particles are transferred. The incident energy of the deuterons is set to 11.8 MeV. All input code for FRESCO may be found in appendix B.

The first line of the input file is reserved for a character string of maximum 80 characters for identification and naming purposes. It has no effect on the FRESCO calculation. The "NAMELIST" command informs FRESCO that the input is in the namelist style and not the standard input. The first section under the header, "&FRESCO" introduces the parameters involved in the numerical calculations. The parameters include but are not limited to: limits and step sizes for the radius used in integrating the Schrödinger equation, starting and maximum values of the total angular momentum to include, start and end angles for the output cross section as well as step size, and the laboratory energy of the projectile. Refer to Table A.3 in appendix A for a complete listing of parameters and their functions.

Under the "&PARTITION" header all the mass partitions and the corresponding channels to be considered in the reaction are stated. Information for the name, mass and proton number of the projectile and target are input. Value names for the projectile information are followed by a "p" and value names for the target information are followed by a "t". The Q-value for the reaction is given by the value named "qval" and is in MeV. The number of states to include in this partition is given by the value of "nex". Each pair of states must then be defined under the following header "&STATES".

The spin, parity and excitation energy for each pair of projectile and target states are defined under the "&STATES" header. The optical potential for the distorted wave describing the relative motion between the projectile and target is given by the index "cpot". If multiple pairs of states are to be included in the calculation this header must be repeated once for each pair.

The final information required to complete a simple elastic scattering example is the optical potential for the interaction between the nuclei. All parameters for the potentials to be used in a calculation are contained under the "&POT" header and must be specified for each required potential. Potentials are identified by an index labeled "kp", with all parameters following the index. The atomic mass of the interacting nuclei and the Coulomb radius are defined with parameters "at/ap" and "rc". These "at/ap" values are used to calculate the physical radii from the expression $R = r_c(ap^{1/3} + at^{1/3})$, while the rc term is the reduced Coulomb radius. The real, volume, Woods-Saxon potential parameters are given by "V", "rv" and "av", while the imaginary volume parameters are given by "W", "rw" and "aw". Spin-orbit interaction parameters use the names "vso", "rso" and "aso".

The "&OVERLAP" and "&COUPLING" headers are used to define non-local coupling

form factors for rearrangement reactions which are not required for elastic scattering calculations and will be discussed in section A.1.2.

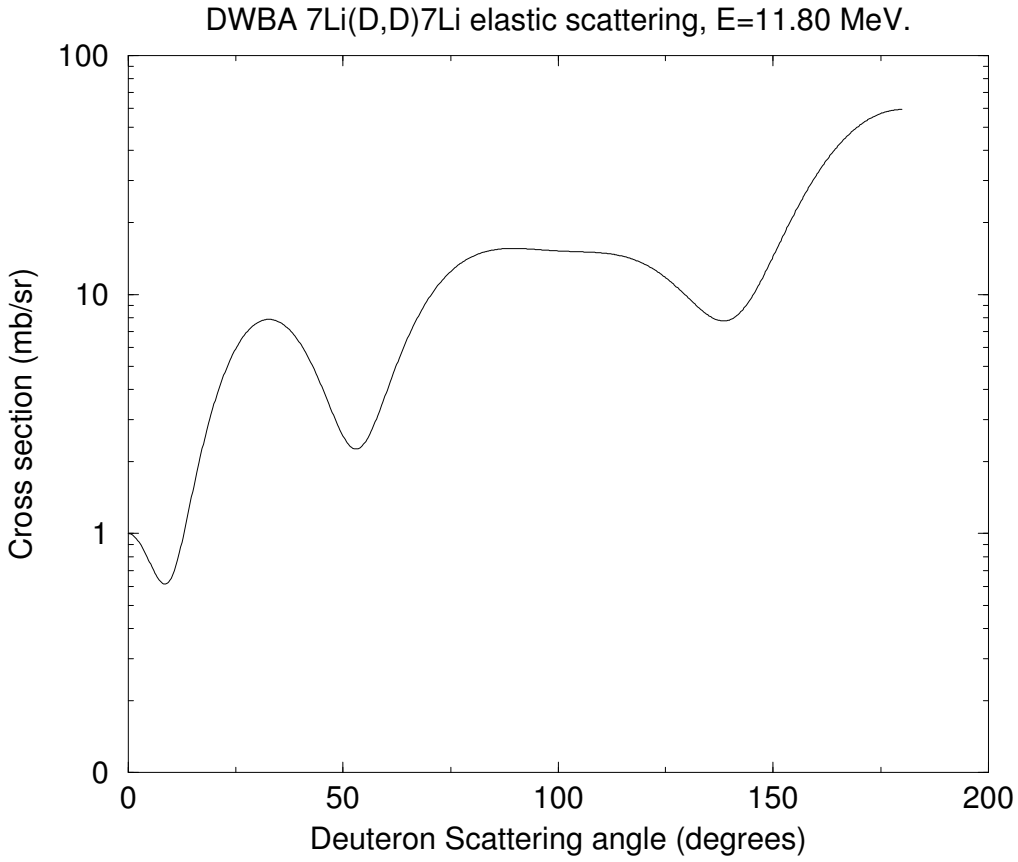

Figure A.1: The FRESCO DWBA calculation of elastic scattering of a deuteron off a ^{7}Li nucleus at a laboratory energy of 11.8 MeV using the input script of Figure B.1.

A.1.2 Transfer Reaction

To create a FRESCO input file for a transfer reaction only a small number of additions need to be added to an elastic scattering input file. Among those additions are new potentials describing the two-body interactions between the core nuclei and the transferred nucleon or cluster; this is known as the binding potential. Two binding potentials are in general required, one for the entrance channel and one for the exit channel. An extra core-core

potential is also required which describes the interaction of the two core nuclei in the absence of the transferred nucleon or cluster. On top of the additional potentials required, the headers "&OVERLAP" and "&COUPLING" are also used for transfer reactions.

The input file for the reaction ^{14}N(^{7}Be,^{8}B)^{13}C is given as an example of a transfer reaction calculation in FRESCO. Partition headers are required for both the entrance and exit channels as they are no longer identical as they were for the case of elastic scattering. The collection of potentials used is summarized in Table A.1. Notice the inclusion of the entrance and exit channel optical potentials, as well as binding potentials for each. The core-core binding potentials and interactions are often indexed as "10" for simple identification.

kp	Interaction	V	V_{SO}	r_V	a_V	W_V	r_W	a_W	r_C
1	$^{7}Be + ^{14}N$	79.1		0.763	0.88	36.0	0.837	0.98	0.697
2	$^{8}B + ^{13}C$	85.2		3.3	0.91	39.3	3.76	1.02	2.939
3	$p + ^{13}C$	54.0		1.3	0.65				1.3
4	$p + ^{7}Be$	44.675	4.898	2.391	0.520				2.391
10	$^{7}Be + ^{13}C$	54.3		0.92	0.79	29.9	1.03	0.69	1.0

Table A.1: Interaction potentials used for FRESCO calculation of ^{14}N(^{7}Be,^{8}B)^{13}C reaction at 84 MeV. The "kp" value corresponds to the index of the potential as it appears in the input file of Figure B.2. Potential depths are in MeV while radii and diffusenesses are in fm.

Overlap functions are needed in calculations of transfer reactions. Similar to the potentials, each overlap is indexed by an index labeled "kn1". For a nuclear state ϕ_i that is transformed into the state ϕ_f by the removal of some nucleons, then the overlap wave function can be expressed as

$$\chi_{f:i}(\mathbf{r}) = \langle \phi_{\mathbf{f}}(\xi_{\mathbf{f}}) | \phi_{\mathbf{i}}(\xi_{\mathbf{f}}, \mathbf{r}) \rangle \tag{A.1}$$

The partial wave components of each overlap function can be written as the sum of an amplitude times the normalized wave functions ϕ, see Equations 2.84, 2.85 and 2.86. These amplitudes are referred to as the spectroscopic amplitudes or coefficients of fractional parentage. The square moduli of the spectroscopic amplitudes are the spectroscopic factors which are related to the ANCs through Equation 2.90.

In the overlap input the composite nucleus is given by the partition "ic1" while the core is given by the partition "ic2", and the overlap refers to either the projectile for "in=1"

or the target for "in=2". The overlap has "nn" number of nodes, "ℓ" relative angular momentum, "sn" for the spin of the transferred particle, and total angular momentum "j" in the composite state. The potential used in the calculation of the state is indexed by the parameter "kbpot". The binding energy "be" of the transferred particle may also be introduced under this heading.

kind	**Type of Coupling**
1	Spin Transfer
2	Electromagnetic Coupling
3	Single particle excitation for projectile
4	Single particle excitation for target
5	Transfer coupling for zero-range corrections
6	Transfer coupling for local energy approximation corrections
7	Transfer coupling for finite-range corrections
8	Transfer coupling for non-orthogonality corrections

Table A.2: Different types of coupling given by the parameter "kind" in the "&COUPLING" heading.

The "&COUPLING" header gives the required information to calculate the couplings of states. The type of transfer is given by the parameter "kind" and is described in Table A.2. The coupling is from all states in partition "icfrom" to all states in partition "icto" and is included in the reverse direction unless "icto < 0". Following the "&COUPLING" header the amplitudes of all the overlaps to be included in the calculation need to be defined. This is done in the "&CFP" (coefficients of fractional parentage) header where "in=1" for the projectile or "in=2" for the target, "ib" and "ia" corresponds to the state index of the composite and core states respectively, and "kn" is the index of the corresponding overlap function. The spectroscopic amplitude is given by the final parameter "a".

The spectroscopic amplitude "a" is a signed value, and is not the spectroscopic factor from Equation 2.85. Typically the spectroscopic amplitudes will be the square roots of the spectroscopic factors [37]. For transfers out of or into closed shells of N antisymmetrised nucleons, the spectroscopic factors will contain factors of N, so the spectroscopic amplitudes needed by FRESCO will typically need to already contain factors of $\sqrt{N}$. In this example, the spectroscopic amplitude for the $p_{1/2}$ component of the valence proton in ^{8}B is set to zero, so only the remaining $p_{3/2}$ component is considered.

A.2 Variable Descriptions

&FRESCO namelist variables

Variable	Meaning
hcm	Step length for integration of the radial part of the Schrödinger equation.
rmatch	Maximum radius to integrate the Schrödinger equation.
rintp	Step length for calculation of the local coupling kernels.
rnl	Range for non-locality.
hnl	Step length of non-local variable $R_{\kappa'}$ in $V_{\alpha:\alpha'}(R_\kappa, R_{\kappa'})$ of equation 2.69
centre	Central point of kernel calculation.
jtmin	Initial value for total angular momentum.
jtmax	Final value for total angular momentum.
absend	If in the interval max(0,jtmin) < J < jtmax the absorption in the elastic channel is smaller than absend millibarns for three consecutive sets, the calculation stops. When absend<0, it takes the full J-interval.
thmin	Starting angle for output cross sections.
thmax	Final angle for output cross section.
thinc	Step size for output angle in degrees in the center of mass frame.
it0	Solve coupled channels by at least this number of iterations.
iter	Solve coupled channels by a maximum of iter iterations.
iblock	The number of pairs of excitation levels that are coupled exactly by blocking together. For DWBA, it0=iter=0 and iblock=1.
nnu	Number of Gaussian integration point used in non-local transfer kernels (multiples of 6).
elab	Laboratory energy of projectile.
	Trace variables to control the output.
chans ≥1	Print decremented list of coupled partial waves for each J/π set.
smats ≥1	Print absorption and reaction cross section.
xstable=1	Save table of calculated cross sections to file fort.16.

Table A.3: Integration and trace variables for the &FRESCO entry

&PARTITIONS and &STATES

Variable	Meaning
namep/namet	name to identify the projectile/traget.
massp/masst	mass number of the projectile/target.
zp/zt	Z of the projectile/target.
nex	number of pairs of excitation of projectile and/or target.
	If < 0 then cross section for this partition are not printed.
pwf	if T, use coupled Coulomb wavefunction necessary for
	long ranged Coulomb multipoles.
qval	Q value of this partition, relative to the Q-value of the
	other partitions, for $E_p = E_t = 0$.
Jp/Jt	spin state of the projectile/target.
bandp/bandt	> 0 for positive parity state, and < 0 for negative parity.
	The value of band defines the rotational band : all states of
	the same band may be coupled by rotational mechanisms.
copyp/copyt	if positive, then this level is a copy of a previous
	level number (COPY $<$ IA) in the same partition.
	if copyp < 0, then this level is an exchange copy of
	the same IA numbered level in the previous partition
	abs(COPY). A copy with projectile and target nuclei exchanged
	copyt = -IC, then the target state is an exchanged projectile.
	If that state has spin zero, then only even partial waves are allowed.
	COPYs are needed to define identical states of one nucleus in
	different pairings IA. Spectroscopic amplitudes should be defined
	for only the original 'copied' level.
eq/et	excitation energy of state relative to ground state for projectile/target.
KP	index of optical potential for this pair of excited states.
cpot	index of potential for interaction of nuclei in the described state.

Table A.4: Variables for the &PARTITIONS and &STATES entry

&POTENTIAL	
Variable	Meaning
kp	Index of potential.
ap/at	atomic mass of projectile/target.
rc	Coulomb radius.
V, rv, av	real volume Woods-Saxon potential parameters.
W, rw, aw	imaginary volume Woods-Saxon potential parameters.
vso, rso, aso	spin-orbit interaction parameters.
All radii follow the convention $R_i = r_i(A_t^{1/3} + A_p^{1/3})$.	

Table A.5: Variables for the &POTENTIAL entry

&OVERLAP	
Variable	Meaning
kn1	Index of overlap.
ic1/ic2	Partition numbers of core and composite nuclei.
in	1 for projectile single particle state, 2 for target.
nn, l, sn	Principal, orbital angular momentum and spin quantum numbers of valence nucleon.
j	Total angular momentum of valence nucleon.
kbpot	Index of binding potential.
be	Binding energy of valence nucleon.
isc	=1 to vary depth of binding potential in order to reproduce be. =0 to vary energy but keep potential fixed.

Table A.6: Variables for the &OVERLAP entry

&COUPLING	
Variable	Meaning
icto / icfrom	Coupling states from partition icfrom to partition icto.
kind	Specify the type of coupling.
ip1, ip2, ip3	kind specific variables.
&CFP	
Variable	Meaning
in	1 for projectile overlap, 2 for targer.
ib	Excitation state of composite nucleus.
ia	Excitation state of the core nucleus.
kn	Bound state form factor. kn1 from the &OVERLAP entry.
a	Spectroscopic amplitude.

Table A.7: Variables for the &COUPLING and &CFP entry

SFRESCO Input commands

Command	Operation
Q	Query status of search variables.
SET var val	Set variable number var to val.
FIX var	Fix variable number var (set step=0).
STEP var step	Unfix variable var with step step.
SCAN var val1 val2 step	Scan raviable var from val1 to val2 in steps of step.
SHOW	List all datasets with current predictions and χ values.
LINE plotfile	Write file (default: search.plot) with theoretical curves only.
READ file	Read plot output file for further searches.
READ snapfile	If the name of snapfile contains the string 'snap', read last set of snap output snapfile from a previous fort.105. file.
ESCAN emin emax estep	Scan lab. energy in incident channel.
MIN	Call MINUIT interactively.
MIGRAD	In MINUIT, perform MIGRAD search.
END	Return to SFRESCO from MINUIT.
PLOT plotfile	Write file (default: search.plot) with data and theory curve.
EX	Exit (also at end of input file).

Table A.8: SFRESCO input commands

Appendix B

FRESCO Input Code

All the code for FRESCO and SFRESCO input files for the examples presented in this thesis are located in this appendix. The input files for the analysis of the data are also located in this appendix.

B.1 Elastic Scattering

```
DWBA 7Li(D,D)7Li elastic scattering, E=11.80 MeV.
NAMELIST
 &FRESCO
 hcm=0.10 rmatch=25 rintp=0.5 hnl=0.100 rnl=5
 jtmin=0.0 jtmax=50.0 absend=.00010
 thmin=0.00 thmax=180.0 thinc=0.25
 chans=1 smats=1 xstabl=1 elab=11.8 /

 &PARTITION namep='deuteron' massp=2.0 zp=1
            namet='Li7' masst=7.0 zt=3
            qval=0.0 pwf=F nex=1 /
 &STATES jp=0.0 bandp=1 ep=0.0 cpot=1
         jt=1.5 bandt=-1 et=0.0 /
 &partition /

 &POT kp=1    at=7.0 at=2.0 rc=1.30
              V=78.0 rv=1.05 av=0.95
              w=30.0  rw=1.04 aw=0.95
              vso=6.4 rso=1.04 aso=0.95 /
 &pot /
 &overlap /
 &coupling /
```

Figure B.1: Elastic scattering FRESCO input file

B.2 Transfer Reaction

```
DWBA 14N(7Be,8B)13C single proton transfer, E=84.0, MeV
NAMELIST
&FRESCO
  hcm=0.100 rmatch=40.00 rintp=0.20 hnl=0.100 rnl=3. centre=0.00
  jtmin=0.0 jtmax=70.0 absend=-0.0010 thmin=0.0 thmax=90.00
  thinc=0.50 it0=1 iter=1 iblock=0 nnu=24 chans=1 smats=2
  xstabl=1 elab=84.0 unitmass=1.000 finec=137.03599d0 /

&PARTITION namep='Be7' massp=7.0169 zp=4 namet='14N'
           masst=14.0033 zt=7 qval=0.0000 pwf=T nex=1 /

&STATES jp=1.5 bandp=-1 ep=0.0000 cpot=1 jt=1.0
        bandt=1 et=0.0000 /

&PARTITION namep='B8' massp=8.0246 zp=5 namet='C13'
           masst=13.0033 zt=6 qval=-7.414 pwf=T nex=1 /

&STATES jp=2 bandp=1 ep=0.0000 cpot=2 jt=0.5
        bandt=-1 et=0.0000 /

&partition /

&POT kp=1 ap=7.0 at=14.0 rc=0.697
     v=79.1000 rv=0.7630 av=0.8800
     w=36.0000 rw=0.8370 aw=0.9800 /

&POT kp=2 ap=1.0000 at=0.0000 rc= 2.9390
     v=85.2000 rv=3.3000 av=0.9100
     w=39.3000 rw=3.7600 aw=1.0200 /
```

```
&POT kp=3 ap=0.0 at=13. rc=1.3
     v=54. rv=1.3 av=0.650 /

&POT kp=4 ap=1.000 at=0.000 rc=2.391
     v=44.675 rv=2.391 av=0.520
     vso=4.898 rso=2.391 aso=0.520 /

&POT kp=10 ap=7.0 at=13. rc=1.
     v=54.3 rv=0.92 av=0.79
     w=29.9 rw=1.03 aw=0.69 /

&pot /

&OVERLAP kn1=10 ic1=2 ic2=1 in=2 nn=1 l=1 sn=0.5
         j=0.5 kbpot=8 be=7.5506 isc=1 /
&OVERLAP kn1=1 ic1=1 ic2=2 in=1 nn=1 l=1 sn=0.5
         j=1.5 kbpot=4 be=0.1370 isc=1 /
&OVERLAP kn1=2 ic1=1 ic2=2 in=1 nn=1 l=1 sn=0.5
         j=0.5 kbpot=4 be=0.1370 isc=1 /
&OVERLAP kn1=3 ic1=1 ic2=2 in=1 nn=1 l=1 sn=0.5
         j=1.5 kbpot=4 be=0.05 isc=1 /
&overlap /

&COUPLING icto=-2 icfrom=1 kind=7 ip1=1 ip2=-1 ip3=10 /
&CFP in=2 ib=1 ia=1 kn=10 a=0.777 /
&CFP in=1 ib=1 ia=1 kn=1 a=1.0 /
&CFP in=1 ib=1 ia=1 kn=2 a=0.0 /
&cfp /
&coupling /
```

Figure B.2: Transfer reaction FRESCO input file.

B.3 ^{7}Li(^{8}Li,^{7}Li)^{8}Li Transfer Reaction

```
DWBA calculation of Exchange transfer 7Li(8Li,7Li)8Li, 11MeV
NAMELIST
 &FRESCO hcm=0.10 rmatch=20 rintp=0.2 hnl=0.100
         rnl=5 centre=0.0 jtmin=0.0 jtmax=10.0
         absend=.001 thmin=1.00 thmax=180.00
         thinc=1.0 ips=0.05 it0=1 iter=1 nnu=24
         chans=1 smats=1  xstabl=1 elab=11.0 /

 &PARTITION namep='8-Li' massp=8. zp=3
            namet='7-Li' masst=7 zt=3 qval=0.0 nex=1  /
 &STATES jp=2.0 bandp=+1 ep=0.0 cpot=1
         jt=1.5 bandt=-1 et=0.0  /

 &PARTITION namep='7-Li' massp=7. zp=3
            namet='8-Li' masst=8 zt=3 qval=0.0 nex=1  /
 &STATES cpot=1 copyp=-1 /

 &partition /

# Entrance and Exit Channel
 &POT kp=1 ap=7.0 at=8.0 rc=1.3
      V=175 rv=0.64 av=0.8
      W=16.9 rw=1.09 aw=0.8  /
# Davids-Typel binding potential p3/2
 &POT kp=2 ap=1.0 at=0.0 rc=2.5
      V=43.19 Vso=0.0 rv=2.5
      av=0.65 /
```

```
# Esbensen-Bertsch binding potential p1/2
 &POT kp=4 ap=1.0 at=0.0 rc=2.391
      V=42.14 vso=4.9 rv=2.391
      av=0.52 /
# Potthast volume-dominated 7Li-7Li potential at 11 MeV
# Core-Core potential
 &POT kp=10 ap=7.0 at=7.0 rc=1.3
      V=4.66 rv=0.173 av=1.617
      W=5.60 rw=1.589 aw=0.397  /
 &pot /
# p3/2 overlap
 &OVERLAP kn1=1 ic1=1 ic2=2 in=1 kind=0 nn=1
          l=1 sn=0.5 j=1.5 kbpot=2 be=2.03229 isc=1  /
 &OVERLAP kn1=2 ic1=2 ic2=1 in=2 kind=0 nn=1
          l=1 sn=0.5 j=1.5 kbpot=2 be=2.03229 isc=1 /
# p1/2 overlap
 &OVERLAP kn1=3 ic1=1 ic2=2 in=1 kind=0 nn=1
          l=1 sn=0.5 j=0.5 kbpot=4 be=2.03229 isc=1  /
 &OVERLAP kn1=4 ic1=2 ic2=1 in=2 kind=0 nn=1
          l=1 sn=0.5 j=0.5 kbpot=4 be=2.03229 isc=1 /
 &overlap /

 &COUPLING icto=2 icfrom=1 kind=7 ip1=0 ip2=-1 ip3=10  /
# 3/2 COUPLING
 &CFP in=1 ib=1 ia=1 kn=1 a=0.868  /
 &CFP in=2 ib=1 ia=1 kn=2 a=0.868  /
# 1/2 COUPLING
 &CFP in=1 ib=1 ia=1 kn=3 a=0.0737  /
 &CFP in=2 ib=1 ia=1 kn=4 a=0.0737  /
 &cfp /
 &coupling /
```

Figure B.3: FRESCO input for the ^{7}Li(^{8}Li,^{7}Li)^{8}Li transfer reaction.

B.4 p + ^{112}Cd elastic scattering

```
p + 112Cd elastic scattering, E=27.90 MeV
NAMELIST
 &FRESCO
  hcm=0.100 rmatch=20.000 rintp=1.00 hnl=0.100 rnl=10.00
  centre=0.00 jtmin=0.0 jtmax=20.0 absend=0.0100
  thmin=0.00 thmax=180.00 thinc=2.00
  ips=0.0000  it0=0 iter=1 iblock=0 chans=1 smats=2 xstabl=1
  elab(1)=27.9000 /

 &PARTITION namep='Proton' massp=1.0000 zp=1 nex=1
            namet='112Cd' masst=112.0000 zt=48
            qval=0.0000/

 &STATES jp=0.5 ptyp=1 ep=0.0000
         cpot=1 jt=0.0 ptyt=1 et=0.0000/

 &partition /    ! END OF DEFINING PARTITIONS

 &pot kp= 1 type= 0 p(1:3)=112.000 0.0000 1.2000/
 &pot kp= 1 type= 1 p(1:6)= 45.500 1.1700 0.7500 1.5000 1.3200 0.6100/
 &pot kp= 1 type= 2 p(1:6)=  0.000 0.0000 0.0000 3.5000 1.3200 0.6100/
 &pot kp= 1 type= 3 p(1:3)=  6.200 1.0100 0.7500/
 &pot /    ! END OF DEFINING POTENTIALS

 &overlap /    ! END OF DEFINING OVERLAPS

 &COUPLING /
```

Figure B.4: FRESCO input file for p + ^{112}Cd elastic scattering.

```
112Cd.search
plot ss-init.plot
q
min
scan
migrad
end
plot ss-fit.plot
```

Figure B.5: SFRESCO script file for the SFRESCO input file found in Figure B.6.

```
 '112Cd.frin' '112Cd.frout'
 4 1
  &variable kind=1 name='r0' kp=1 pline=2 col=2 potential=1.171 step=0.01/
  &variable kind=1 name='V' kp=1 pline=2 col=1 potential=45.50 step=0.1/
  &variable kind=1 name='W' kp=1 pline=2 col=4 potential=1.5 step=0.1/
  &variable kind=1 name='WD' kp=1 pline=3 col=4 potential=4.5 step=0.1/
  &data iscale=0  idir=1 lab=F  points=28 abserr=T/
   22.       0.548      0.044
   26.       0.475      0.024
   30.       0.481      0.014
   34.       0.502      0.010
   38.       0.447      0.009
   42.       0.256      0.005
   46.       0.115      0.003
   50.       0.144      0.004
   54.       0.371      0.011
   58.       0.612      0.012
   62.       0.678      0.014
   66.       0.499      0.010
   70.       0.248      0.005
   74.       0.086      0.003
   78.       0.119      0.004
   82.       0.289      0.009
   86.       0.463      0.014
   90.       0.485      0.015
   94.       0.398      0.012
   98.       0.235      0.007
   102.      0.123      0.004
   106.      0.087      0.003
   110.      0.135      0.004
   114.      0.198      0.006
   118.      0.225      0.009
   122.      0.223      0.009
   126.      0.189      0.006
   130.      0.161      0.005
 &
```

Figure B.6: SFRESCO input file for the FRESCO input file found in Figure B.4.

B.5 SFRESCO

```
'Li2_Exchange11.frin' 'Li2_Exchange11.frout'
6 1
 &variable kind=1 name='V' kp=1 pline=2 col=1 step=0.1/
 &variable kind=1 name='rv' kp=1 pline=2 col=2 step=0.1/
 &variable kind=1 name='av' kp=1 pline=2 col=3 step=0.1/
 &variable kind=1 name='W' kp=1 pline=2 col=4 step=0.1/
 &variable kind=1 name='rw' kp=1 pline=2 col=5 step=0.1/
 &variable kind=1 name='aw' kp=1 pline=2 col=6 step=0.1/
 &variable kind=5 name='norm1' dataset=1 datanorm=0.0094 /
 &variable kind=2 name='a3/2' nafrac=1 afrac=0.868 step=0.01/
 &data type=0 points=13 energy=11.0 idir=0 iscale=2 lab=F abserr=T/
 21.44663        266365.1        18975.76
 23.59555        165623.7        11884.37
 25.74572        116030.2        8379.325
 27.89728        75926.23        5532.77
 30.05036        44744.02        3336.144
 32.20510        27413.07        2292.66
 78.42747        421.9482        20.90864
 84.07995        461.7515        22.56461
 89.34119        438.7153        21.34884
 94.44160        349.5466        18.19396
 99.38766        302.1436        16.84404
 103.9448        285.5333        16.96672
 108.3533        281.2268        16.96982
 &
```

Figure B.7: SFRESCO input file for the ^{8}Li + ^{7}Li elastic scattering fit

Appendix C

MINUIT

Minuit was probably the first minimization program to offer full user choice from a selection of several minimization algorithms. When Minuit was first introduced none of the algorithms known at the time was good enough to be universal. When fitting a function users were encouraged to find an algorithm that worked best for them. In the years since Minuit was first introduced algorithms have improved considerable to the point where user selection is all but unnecessary. There are still the occasional users who require alternative minimizers and thus the option for user choice is still present in Minuit.

Minuit currently offers five commands which can be used to find a smaller function value as well as a few other commands to help with minimization. This appendix will describe the two commands that were used in this study, MIGRAD and SCAN. For a full description of all the commands please see reference [49].

C.1 MIGRAD

As a variable-metric method with inexact line search, a stable metric updating scheme, and checks for positive definiteness this is the best minimizer for nearly all functions. The SET STRATEGY command may be used to adjust the run time at the cost of reliability. A value of 0 for the SET STRATEGY command will run much faster than a value of 2 but will not be as reliable.

The main weakness of MIGRAD is its heavy dependence on the first derivatives. If the first derivatives of the fitting parameters are very inaccurate MIGRAD will fail miserably.

If the first derivatives are a problem, they can be calculated analytically inside a multiparameter Fortran function. If this is not possible the user can try other methods to improve the accuracy of Minuit's numerical approximation by adjusting various other values.

C.2 SCAN

The SCAN command is not intended to be a minimizer. Its purpose is to scan the function, one parameter at a time by adjusting the parameter by a set step size to cover the entire range of values set by the limits on the parameter. The number of points to be scanned is 40 by default but can range up to 100. This is a useful command to debug a user function or to find a reasonable starting point for minimization. The command also presents the curve resulting from each parameter scan in order to show the approximate behaviour of the function over the scanned values.

Bibliography

[1] E. G. Adelberger *et al.*, "Solar fusion cross sections. II. The pp chain and CNO cycles," *Rev. Mod. Phys.*, vol. 83, pp. 195–245, Apr 2011.

[2] R. H. Cyburt, B. Davids, and B. K. Jennings, "Determination of $S_{17}(0)$ from published data," *Phys. Rev. C*, vol. 70, p. 045801, Oct 2004.

[3] B. Mattson, "Imagine the universe." `http://imagine.gsfc.nasa.gov/docs/teachers/elements/imagine/05.html`, Accessed in 2012.

[4] W. S. Rolfs, C. E. & Rodney, *Cauldrons in the Cosmos.* The University of Chicago Press, 1988.

[5] F. Reines and C. L. Cowan, "Detection of the free neutrino," *Phys. Rev.*, vol. 92, pp. 830–831, Nov 1953.

[6] G. Danby, J.-M. Gaillard, K. Goulianos, L. M. Lederman, N. Mistry, M. Schwartz, and J. Steinberger, "Observation of high-energy neutrino reactions and the existence of two kinds of neutrinos," *Phys. Rev. Lett.*, vol. 9, pp. 36–44, Jul 1962.

[7] M. L. Perl *et al.*, "Evidence for anomalous lepton production in $e^+ - e^-$ annihilation," *Phys. Rev. Lett.*, vol. 35, pp. 1489–1492, Dec 1975.

[8] J. N. Bahcall, *Unsolved Problems in Astrophysics.* Princeton University Press, 1997.

[9] J. N. Bahcall, "Solar neutrinos. I. Theoretical," *Phys. Rev. Lett.*, vol. 12, pp. 300–302, Mar 1964.

[10] G. Feinberg, "The neutrino in astrophysics," *Proceedings of the Royal Society of London. Series A. Mathematical and Physical Sciences*, vol. 285, no. 1401, pp. 257–262, 1965.

[11] K. S. Hirata *et al.*, "Search for correlation of neutrino events with solar flares in Kamiokande," *Phys. Rev. Lett.*, vol. 61, pp. 2653–2656, Dec 1988.

[12] J. N. Bahcall, A. M. Serenelli, and S. Basu, "New solar opacities, abundances, helioseismology, and neutrino fluxes," *The Astrophysical Journal Letters*, vol. 621, no. 1, p. L85, 2005.

[13] A. I. Abazov *et al.*, "Search for neutrinos from the Sun using the reaction ^{71}Ga(ν_e,e^-)^{71}Ge," *Phys. Rev. Lett.*, vol. 67, pp. 3332–3335, Dec 1991.

[14] P. Anselmann *et al.*, "Solar neutrinos observed by GALLEX at Gran Sasso," *Physics Letters B*, vol. 285, no. 4, pp. 376 – 389, 1992.

[15] Y. Fukuda *et al.*, "Constraints on neutrino oscillation parameters from the measurement of day-night solar neutrino fluxes at super-Kamiokande," *Phys. Rev. Lett.*, vol. 82, pp. 1810–1814, Mar 1999.

[16] S. M. Bilenky and B. Pontecorvo, "Lepton mixing and neutrino oscillations," *Physics Reports*, vol. 41, no. 4, pp. 225 – 261, 1978.

[17] Q. R. Ahmad *et al.*, "Direct evidence for neutrino flavor transformation from neutral-current interactions in the Sudbury neutrino observatory," *Phys. Rev. Lett.*, vol. 89, p. 011301, Jun 2002.

[18] Q. R. Ahmad *et al.*, "Measurement of the rate of $\nu_e + d \rightarrow p + p + e^-$ interactions produced by ^{8}B solar neutrinos at the sudbury neutrino observatory," *Phys. Rev. Lett.*, vol. 87, p. 071301, Jul 2001.

[19] G. Bellini *et al.*, "Precision measurement of the ^{7}Be solar neutrino interaction rate in borexino," *Phys. Rev. Lett.*, vol. 107, p. 141302, Sep 2011.

[20] B. W. Filippone, A. J. Elwyn, C. N. Davids, and D. D. Koetke, "Proton capture cross section of ^{7}Be and the flux of high energy solar neutrinos," *Phys. Rev. C*, vol. 28, pp. 2222–2229, Dec 1983.

[21] T. Teichmann and E. P. Wigner, "Sum rules in the dispersion theory of nuclear reactions," *Phys. Rev.*, vol. 87, pp. 123–135, Jul 1952.

[22] P. A. Tipler and R. A. Llewellyn, *Modern Physics*. W. H. Freeman and Company, 2000.

[23] A. R. Junghans, E. C. Mohrmann, K. A. Snover, T. D. Steiger, E. G. Adelberger, J. M. Casandjian, H. E. Swanson, L. Buchmann, S. H. Park, A. Zyuzin, and A. M. Laird, "Precise measurement of the ^{7}Be(p,γ)^{8}B S factor," *Phys. Rev. C*, vol. 68, p. 065803, Dec 2003.

[24] Ian J. Thompson and Filomena M. Nunes, *Nuclear Reactions for Astrophysics*. Cambridge University Press, 2009.

[25] L. E. Ballentine, *Quantum Mechanics: A Modern Development*. World Scientific, 2003.

[26] R. Pike and P. Sabatier, *Scattering*. Academic Press, 2002.

[27] A. M. Mukhamedzhanov, H. L. Clark, C. A. Gagliardi, Y.-W. Lui, L. Trache, R. E. Tribble, H. M. Xu, X. G. Zhou, V. Burjan, J. Cejpek, V. Kroha, and F. Carstoiu, "Asymptotic normalization coefficients for ^{10}B $\rightarrow^{9}$ Be + p," *Phys. Rev. C*, vol. 56, pp. 1302–1312, Sep 1997.

[28] A. Azhari, V. Burjan, F. Carstoiu, C. A. Gagliardi, V. Kroha, A. M. Mukhamedzhanov, F. M. Nunes, X. Tang, L. Trache, and R. E. Tribble, "Asymptotic normalization coefficients and the ^{7}Be(p,γ)^{8}B astrophysical S factor," *Phys. Rev. C*, vol. 63, p. 055803, Apr 2001.

[29] G. Tabacaru, A. Azhari, J. Brinkley, V. Burjan, F. Carstoiu, C. Fu, C. A. Gagliardi, V. Kroha, A. M. Mukhamedzhanov, X. Tang, L. Trache, R. E. Tribble, and S. Zhou, "Scattering of ^{7}Be and ^{8}B and the astrophysical S_{17} factor," *Phys. Rev. C*, vol. 73, p. 025808, Feb 2006.

[30] H. M. Xu, C. A. Gagliardi, R. E. Tribble, A. M. Mukhamedzhanov, and N. K. Timofeyuk, "Overall normalization of the astrophysical S factor and the nuclear vertex constant for ^{7}Be(p,γ)^{8}B reactions," *Phys. Rev. Lett.*, vol. 73, pp. 2027–2030, Oct 1994.

[31] T. Davinson, W. Bradfield-Smith, S. Cherubini, A. DiPietro, W. Galster, A. Laird, P. Leleux, A. Ninane, A. Ostrowski, A. Shotter, J. Vervier, and P. Woods, "Louvain-Edinburgh detector array (LEDA): A silicon detector array for use with radioactive nuclear beams," *Nuclear Instruments and Methods in Physics Research Section A: Accelerators, Spectrometers, Detectors and Associated Equipment*, vol. 454, no. 2 - 3, pp. 350 – 358, 2000.

[32] L. Trache, A. Azhari, F. Carstoiu, H. L. Clark, C. A. Gagliardi, Y.-W. Lui, A. M. Mukhamedzhanov, X. Tang, N. Timofeyuk, and R. E. Tribble, "Asymptotic normalization coefficients for ^{8}B $\rightarrow^7$ Be + p from a study of ^{8}Li $\rightarrow^7$ Li + n," *Phys. Rev. C*, vol. 67, p. 062801, Jun 2003.

[33] R. B. Wiringa, "Two-cluster distribution functions." `http://www.phy.anl.gov/theory/research/overlap/`, 2011.

[34] S. Wright, "ANC for the valence neutron in ^{8}Li from a study of ^{8}Li(^{7}Li,^{8}Li)^{7}Li a mirrored approach to $S_{17}(0)$," Master's thesis, University of Surrey, UK, 2006.

[35] R. B. . F. Rademakers, "ROOT User's Guide v5.26." `http://root.cern.ch/drupal/content/users-guide`.

[36] I. J. Thompson, "Coupled reaction channels calculations in nuclear physics," *Computer Physics Reports*, vol. 7, no. 4, pp. 167 – 212, 1988.

[37] I. J. Thompson, "Fresco user's guide." `http://www.fresco.org.uk/`, 2010.

[38] B. Davids and S. Typel, "Electromagnetic dissociation of ^{8}B and the astrophysical S factor for ^{7}Be(p,γ)^{8}B," *Phys. Rev. C*, vol. 68, p. 045802, Oct 2003.

[39] H. Esbensen and G. Bertsch, "Effects of E2 transitions in the coulomb dissociation of ^{8}B," *Nuclear Physics A*, vol. 600, no. 1, pp. 37 – 62, 1996.

[40] K. Potthast, H. Brand, H. Freiesleben, P. Rosenthal, B. Kamys, H. gen. Schieck, and L. Sydow, "Global optical model potentials for symmetrical lithium systems: ^{6}Li +^{6} Li, ^{7}Li +^{7} Li at Elab = 5 $\rightarrow$ 40 MeV," *Nuclear Physics A*, vol. 614, no. 1, pp. 95 – 111, 1997.

[41] F. D. Becchetti, W. Z. Liu, K. Ashktorab, J. F. Bajema, J. A. Brown, J. W. Jänecke, D. A. Roberts, J. J. Kolata, K. L. Lamkin, A. Morsad, R. J. Smith, X. J. Kong, and R. E. Warner, "Systematics of ^{8}Li induced radioactive beam reactions: E=13˘20 MeV," *Phys. Rev. C*, vol. 48, pp. 308–318, Jul 1993.

[42] I. J. Thompson. Private Communication, 2009.

[43] W. T. Eadie, D. Drijard, F. James, M. Roos, and B. Sadoulet, *Statistical Methods in Experimental Physics*. Elsevier Science Ltd, 1971.

[44] J. F. Ziegler, M. Ziegler, and J. Biersack, "SRIM - The stopping and range of ions in matter," *Nuclear Instruments and Methods in Physics Research Section B: Beam Interactions with Materials and Atoms*, vol. 268, no. 11-12, pp. 1818 – 1823, 2010. 19th International Conference on Ion Beam Analysis.

[45] T. Davinson. Private Communication, 2006.

[46] N. K. Timofeyuk and P. Descouvemont, "Asymptotic normalization coefficients for mirror virtual nucleon decays in a microscopic cluster model," *Phys. Rev. C*, vol. 71, p. 064305, Jun 2005.

[47] A. Volkov, "Equilibrium deformation calculations of the ground state energies of 1p shell nuclei," *Nuclear Physics*, vol. 74, no. 1, pp. 33 – 58, 1965.

[48] D. Thompson, M. Lemere, and Y. Tang, "Systematic investigation of scattering problems with the resonating-group method," *Nuclear Physics A*, vol. 286, no. 1, pp. 53 – 66, 1977.

[49] F. James, "Minuit reference manual." `http://wwwasdoc.web.cern.ch/wwwasdoc/minuit/minmain.html`, Accessed in 2012.